DISSERTATION

Theoretical Investigations of Magneto-Optical Properties of Multi-Layer Systems

ausgeführt zum Zwecke der Erlangung des akademischen Grades eines Doktors der technischen Wissenschaften

unter der Leitung von

Prof. Dr. phil. Peter Weinberger

E 134
Institut für Allgemeine Physik

eingereicht an der Technischen Universität Wien
Fakultät für Physik

von

Dipl.-Ing. Irene Reichl
97 25 549

23. Mai 2005

THESIS

Theoretical Investigations of Magneto-Optical Properties of Multi-Layer Systems

performed in application for the degree of a
Doctor of Technical Sciences

under the guidance of

Prof. Dr. phil. Peter Weinberger

E 134
Institut für Allgemeine Physik

submitted to the
Vienna University of Technology
Faculty for Physics

by

Dipl.-Ing. Irene Reichl
97 25 549

23^{rd} May 2005

Kurzfassung

Die Gründe, magneto-optische Materialeigenschaften zu studieren reichen von Fragestellungen der Grundlagenforschung bis hin zu technologischen Anwendungen. Der magneto-optische Kerr Effekt (MOKE) spiegelt sehr empfindlich die magnetischen Aspekte der elektronischen Struktur wider. Im Rahmen dieser Dissertation werden die magneto-optischen Eigenschaften mit Hilfe der Spin-polarisierten relativistischen abgeschirmten Korringa-Kohn-Rostoker Methode, der Luttinger Formel für finite Photonenenergien und einem klassischen optischen Zugang, der alle Reflexionen und Interferenzen in Betracht zieht, berechnet.

Als erstes wird ein magnetischer Reorientierungsübergang anhand von $\mathrm{Fe}_n/\mathrm{Au}$ studiert. Sowohl der experimentelle Befund als auch theoretische Anisotropieberechnungen zeigten die Reorientierung der Grundzustandsmagnetisierung von einer senkrechten zu einer parallelen Oberflächenmagnetisierung, wenn die Eisendicke 3 Monolagen überschreitet. Es stellte sich heraus, dass die Analyse mit Hilfe des ab-initio berechneten MOKE bestens dafür geeignet ist, das Verständnis über dieses physikalische System zu vergrößern. Aber nicht nur der Reorientierungsübergang wurde untersucht, darüber hinaus wurde auch die Geometrieabhängigkeit des MOKE dokumentiert.

Die Kopplung zweier magnetischer Schichten wurde in Abhängigkeit von der Dicke der paramagnetischen Spacer-Schicht als zweites Beispiel anhand von $\mathrm{Cu}_4\mathrm{Ni}_8\mathrm{Cu}_n\mathrm{Ni}_9/\mathrm{Cu}(100)$, $n = 2, \ldots, 10$ untersucht. Die Oszillationen des MOKE stimmen sehr gut mit dem Verhalten der berechneten Interlagenkopplungsenergien (inter-layer exchange coupling (IEC) energies) überein. Ein interessantes Ergebnis dieser Untersuchung ist, dass der MOKE nicht einfach nur mit dem magnetischen Gesamtmoment linear verknüpft ist. Aufgrund endlicher Eindringtiefe sieht das Licht nicht mehr jede Lage gleich stark, sondern die inneren Lagen viel schwächer.

Abschließend wurden CoPt Superstrukturen behandelt, die Zuktunftskandidaten für senkrecht magnetisierte magneto-optische Medien sind.

Abstract

There exist many reasons for studying magneto-optical material properties of solids and surfaces, from a fundamental as well as from a technological point of view because the magneto-optical Kerr effect (MOKE) is extremely sensitive to the magnetic aspects of the electronic structure. In this thesis the magneto-optical properties are investigated theoretically by using the spin-polarized relativistic screened Korringa-Kohn-Rostoker method, the Luttinger formula for finite photon frequencies and a classical optical approach that takes into account multiple reflections and interferences.

First, the studies were devoted to a magnetic reorientation transition in $\mathrm{Fe}_n/\mathrm{Au}(100)$. Experimental investigations and theoretical magnetic anisotropy energy calculations show that the equilibrium magnetization turns from out-of-plane to in-plane as the iron thickness exceeds three mono-layers. The results showed that the analysis of the reorientation transition by means of the ab-initio magneto-optical Kerr effect is very well suited to augment our understanding of physical properties in this system. Not only the description of this transition was the topic there, but also the dependence of the MOKE on the geometry was analyzed in some detail. The relations between the photon propagation direction of the beam, the magnetization and the surface normal were varied. For each configuration the Kerr rotation and ellipticity angles were determined.

Second, the magnetic inter-layer exchange coupling in $\mathrm{Cu}_4\mathrm{Ni}_8\mathrm{Cu}_n\mathrm{Ni}_9/\mathrm{Cu}(100)$, $n = 2, \ldots, 10$ was discussed in terms of the ab-initio calculated MOKE. The occurring oscillations in the Kerr angles with respect to the spacer thickness resemble closely those for the inter-layer exchange coupling energy. As an interesting result it was observed that the Kerr signals are found to be not direct proportional to the total magnetic moment. Due to the finite penetration depth of the light, weighted layer-resolved magnetic moments have to be considered, in order to assign at least indirectly the size of the Kerr angles.

Finally an example from technology, a CoPt superstructure being a candidate to become a future material for perpendicular magneto-optical recording, was discussed.

Contents

1 Introduction

1.1 Developments in magneto-optics

1845 was the birth of magneto-optics as Michael Faraday discovered the *magneto-optical (MO) Faraday effect*. It was observed that light transmitted through a magnetic sample suffered from a change of the polarization. [1] Faraday's discovery drew immediately wide attention as this was the first observation of interaction between magnetism and light. In 1876, John Kerr discovered the corresponding effect in reflection, the *magneto-optical Kerr effect* (MOKE). [2] In 1897 Zeeman observed the Zeeman effect, two years later Voigt reported the occurrence of magnetic double refraction in Na vapor. In 1902 Majorana reported magnetic double refraction in a colloidal suspension of metal particles and in 1907 Cotton and Mouton saw the same in paramagnetic liquids.

One of the primary consequences of these discoveries was to conceive light as an electromagnetic entity. Magneto-optics played a key role in the development of Maxwell's theory on electromagnetism. Maxwell theory provides a macroscopic description of the MOKE involving the energy and material dependent dielectric tensor, $\boldsymbol{\varepsilon}(\omega)$, and the conductivity tensor, $\boldsymbol{\sigma}(\omega)$. At that time quantum mechanics has not been considered yet, thus the theoretical understanding of MO effects was completely lacking.

Considerable effort to investigate the MOKE has been done since, on one hand, interest in modern data storage technology was present and since, on the other hand, MOKE was regarded a powerful spectroscopic tool in materials research. In 1957, Williams et al. [3] and later Conger and Tomlinson [4] and Supernowicz [5] gave evidence that suitably stored magnetic information could be read-out by means of MOKE. Technological research was directed in order to find better materials for MO recording, i.e. higher MO response at smaller wavelengths in combination with chemical and physical stability of the material. In the beginnings particularly ferromagnetic materials were investigated. [6, 7].

The theoretical understanding did not develop as fast as applied research; in 1884, Lorentz [8] proposed that left- and right circularly polarized light couple differently to the classical electron oscillators of the solid, theoretical extensions were made by Drude. In 1932, Hulme [9] proposed that MOKE is caused by the symmetry breaking due to spin-orbit coupling (SOC). It was not yet possible to consistently explain the peak structure of the Kerr spectrum. Suggestions for large peaks were free-carrier plasma resonances [10], scalar relativistic effects [11], or half-metallic band-structure properties [12]. In itself they all form contributions to the structure of the Kerr spectra but is was more desirable to have a quantitative first principles theory of the Kerr spectra in order to be able to make predictions in materials research.

A formulation in which both, SOC and spin polarization, were treated was developed by Argyres, [13] but still at that time no direct comparison between theory and experiment possible. Considerable advances were made with the advent of inter-band theories, [14] but also then transition matrix elements were only estimated. Accurate band structure calculations first became possible in the framework of density functional theory and the local spin-density approximation (LSDA). [15, 16]

The quantum-mechanical formulation based on the Kubo formalism [17] was pushed forward by Wang and Callaway in 1974. [18] allowing for taking into account the absorptive parts of the conductivity tensor by means of the linear-response Kubo-theory. [17] They calculated the absorptive part of $\sigma_{xx}(\omega)$ and $\sigma_{xy}(\omega)$ but the spectra did not compare well to experiment.

In its initial state the first principles calculations were hardly even compared to experiment, satisfactory agreement between experiment and theory was given then only within modern ab-initio relativistic band theory where the first MOKE spectra were calculated by Oppeneer et al. [19, 20, 21] Subsequently, other relativistic band-structure calculations were performed. [22, 23] Since then it is possible to make predictions of MOKE-spectra from first-principles energy-band calculations.

The problems of this theory can be summarized as follows; the Kohn-Sham [15] energy bands are used to evaluate the optical spectra in a linear response formalism, although formally the Kohn-Sham energy bands are not the same as the electron band energies. But it is quite common to assume that they are the same. More seriously is the fact that explicit many body effects, such as electron-hole and final state-effects, are neglected.

Also the magneto-crystalline anisotropy is initiated by SOC, therefore a relationship between magneto-crystalline anisotropy and MOKE is expected which was analyzed by Weller. [24] The MOKE thus offers an insight into the spin-polarized electronic structure of a magnetic material because it is extremely sensitive to those parts of the band structure which initially give rise to magnetism. Therefore the magneto-optical Kerr effect is widely used as a spectroscopic tool to probe magnetic aspects of electronic structure, e.g. the exchange splitting.

MOKE is relatively insensitive to surface effects and is regarded as a bulk sensitive electronic structure method. Typically the valence band region of a metal with an information depth of several ten nm is probed. But studies of Liu and Bader [25] showed that MOKE can also be used for probing surface magnetism.

(A detailed description is found in Ebert. [26])

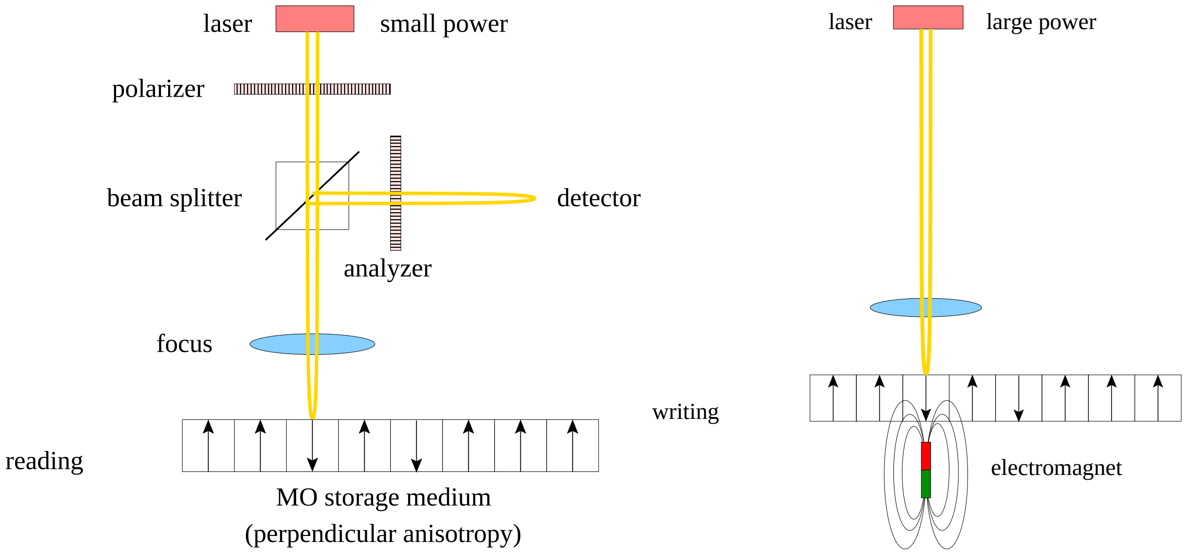

Figure 1.1: Magneto-optical reading and writing devices.

Nonlinear inelastic and linear elastic magneto-optic effects can be distinguished, the latter being the topic of this thesis.

1.2 Magneto-optical recording

1.2.1 The mechanism of magneto-optical recording

Fig. 1.1 schematically describes the mechanism of magneto-optical reading and writing devices. The two states of a bit, 0 and 1, are represented by two opposite magnetization states, left and right in the case of longitudinal MO recording and up and down in the case of perpendicular MO recording. In the writing process locally one bit is heated up to the Curie temperature and the magnetization is aligned in the direction of the applied external field. In writing, the laser power is approximately times larger than in the reading process. Too high temperatures in reading must be avoided because those might lead to information loss (erasure). The polarization change of the initially linear polarized beam can be detected and evaluated as described in appendix A. [27, 28]

Reading and writing is as fast as the laser can be modulated and the disc rotates; the overwriting speed strongly depends on the technique used. In the first approaches in MO recording the disc rotated twice, the first turn for erasing, the second for writing; in order to save time, techniques for direct overwriting (DOW) have been developed, including the *laser intensity modulation* and the *magnetic field modulation* technique.

1.2.2 Magneto-optical devices

After the first realization of magneto-optical devices by Sony in 1991 [29, 30] quite a large number of companies focussed on MO recording.

Although MO storage media may not be the fastest (concerning data access time and transfer rate) and cheapest rewritable medium, it has a number of favorable opportunities, e.g., the highest possible storage density, better reliability and robustness against external influences. [31] A comparison between magnetic and MO recording media shows that the risk of head crashes in hard discs is more likely due to the close correlation between the head-disk distance and the storage density. Contrary to that, in MO devices the resolution is primarily determined by the wave-length of the laser light and the distance between head and disc can be by a factor of 10 larger. Also purely optical devices such as compact discs are more vulnerable than MO-discs. Depending on the technique used for the compact discs (bubble forming, pit forming, dye ablative, or phase changing) different weak points may be expected. MO media can also be compared to the phase-change (PC) media where the two different states, amorphous and crystalline, are distinguished by measuring the intensity of the reflected light. Although PC media may have a strong read signal, a high signal to noise ratio (SNR), and are cheap, the important drawbacks of this method are that writing and erasure do not range in the same time-scale and that repeated melting ($T \approx 600^0$C) leads to segregation and other unpleasant modifications of the surface. The number of read/write/erase cycles in MO media (≈ 100 cycles) is about ten times larger than that for PC. Since only the *Curie temperature* of the medium has to be reached, the temperature is by far smaller than for PC media, for MO discs employing the *magnetic field modulation* (MFM) technique the temperature is only 180^0C.

1.3 Organization of the present thesis

As was done also historically, we start our description with the phenomenological part. The macroscopic Maxwell equations alone are used to describe the wave propagation through the material and the boundary conditions determine the reflection and refraction of the wave. This part is partly well documented in the literature. However, we will describe this classical optical part in quite some detail; first because an important part of the work was devoted to extend the existing code and theory to calculate the MOKE accounting multiple reflections and interferences; and second because the ab-initio calculated results were compared to a simple 2-media approach formula widely discussed in literature. [32, 33, 34, 35] The two-media approach formula was confirmed by You and Shin [36, 37, 38] by comparison to the experimental investigations documenting the dependence on the angle of incidence of Deeter and Sarid. [39] Up to here the optical constants were taken from experiment and could not be determined from first principles theory.

The two-media formula becomes also important if the size and the orientation of the magnetic moments should be deduced from the measured Kerr data. [40]

In the second part the basic ideas about multiple scattering theory and the quantum-mechanical conductivity given in the Kubo-formalism will be explained. It was the intention to keep this introduction rather straight in order to avoid to veil the physical meaning. A perfect description of all theoretical and computational details about multiple scattering theory is found in Zabloudil et al [41], a review on electric transport in Palotás et al [42].

The third part of this thesis summarizes the physical problems that were studied in the frame-work of first principle calculations of MOKE. The systems were carefully selected covering some of the most interesting subjects in surface physics. In Chapter 10 we present a magnetic reorientation transition in Fe/Au(100). Not only the description of this transition was the topic there, but also the dependence of the MOKE on the geometry (i.e. the relations between the photon propagation direction of the beam, the magnetization and the surface normal) was analyzed in some detail. In Chapter 11 we discuss the magnetic coupling in Cu/Ni tri-layer systems. The interesting point here was that our ab-initio calculations showed that there is no direct relationship of the total magnetic moment to the Kerr rotation angles, but that the light, due to the finite penetration depth, does not see the magnetic moments deep inside the material. In Chapter 12 we discuss an example from technology, a CoPt superstructure being a candidate to become a future material for perpendicular recording.

Part I

Macroscopic treatment: Classical optics

2 Polarization

Commonly, the polarization of a wave is represented in either of two different complete ortho-normal basis sets. The first possibility is the decomposition in linearly polarized waves,

$$\begin{pmatrix} 1 \\ 0 \end{pmatrix} \cos(\mathbf{kr} - \omega t) \quad \text{and} \quad \begin{pmatrix} 0 \\ 1 \end{pmatrix} \cos(\mathbf{kr} - \omega t) \quad , \tag{2.1}$$

the second the decomposition in circularly polarized waves,

$$\mathrm{Re}\left[\begin{pmatrix} 1 \\ \pm i \end{pmatrix} e^{i\mathbf{kr} - i\omega t} \right] = \begin{pmatrix} \cos(\mathbf{kr} - \omega t) \\ \mp \sin(\mathbf{kr} - \omega t) \end{pmatrix} \quad . \tag{2.2}$$

If we are dealing with monochromatic waves, only one frequency is needed. The time evolution of the electric field vector describes a line, an ellipsis or a circle in the polarization plane. For two frequencies present the famous Lissajous-figures are obtained, see Fig. 2,

$$A_1 \begin{pmatrix} \cos(\omega_1 t) \\ \sin(\omega_1 t) \end{pmatrix} + A_2 \begin{pmatrix} \cos(\omega_2 t) \\ -\sin(\omega_2 t) \end{pmatrix} \quad \text{for} \quad \mathbf{r} = 0 \quad . \tag{2.3}$$

In Fig. 2 the sense of rotation handedness of the two circularly polarized waves is depicted (solid lines). A left circularly polarized (LCP) wave has positive helicity, ie. $\mathbf{E}$ turns counter-clock-wise when the observer is facing in the on-coming wave. This concept is opposite to that of the handedness. Under time inversion the LCP wave becomes right circularly polarized and vice versa.

An arbitrary polarized wave can be seen as a linear combination of the two circularly polarized basis waves where complex coefficients are possible. The phase of the complex coefficients shifts the phase factor of the circular polarized waves. In Fig. 2 (dash-dotted line) this is visualized for a phase-shift of $e^{i\pi/2}$,

$$\begin{pmatrix} 1 \\ \pm i \end{pmatrix} e^{-i\omega t + i\frac{\pi}{2}} = \begin{pmatrix} \sin(\omega t) \\ \mp \cos(\omega t) \end{pmatrix} \quad .$$

2.1 Magneto-optical Kerr effect and the surface reflectivity matrix

If an incident linearly polarized beam is elliptically polarized upon reflection from a magnetic sample, then this effect is called the magneto-optical Kerr effect (MOKE). Commonly, two quantities, the Kerr rotation angle θ_K and Kerr ellipticity angle ε_K, see Fig. 2.3,

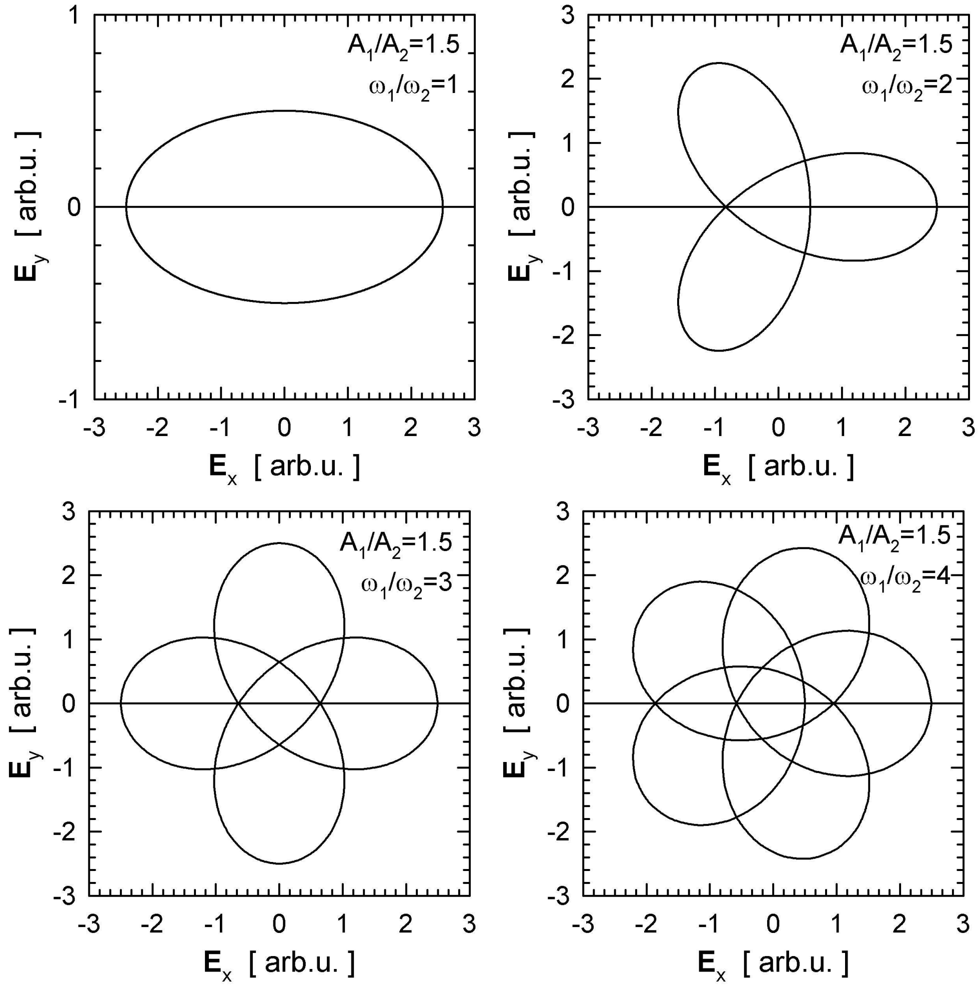

Figure 2.1: Lissajous-figures. For a rational fraction ω_1/ω_2 a closed trajectory is obtained, for an irrational fraction ω_1/ω_2 the trajectory will never visit the same point in the polarization plane twice.

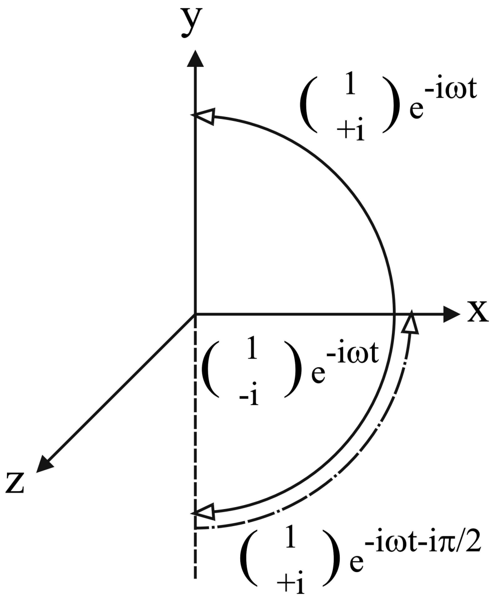

Figure 2.2: Handedness of circularly polarized waves.

are used to describe this kind of polarization change. At first the MOKE is discussed for normal incidence, then formulas for oblique incidence are derived .

2.1.1 Normal incidence

Before analyzing the oblique incidence the surface is assumed to lie in the $(xy)-$plane and the incident beam parallel to the $z-$axis. In vacuum, $E_z = 0$, thus, only a relation for the x- and the y- component of incident and reflected light is necessary. For an arbitrary direction of the magnetization ($\tilde{r}_{xx} \neq \tilde{r}_{yy}$ and $\tilde{r}_{xy} \neq -\tilde{r}_{yx}$), the surface reflectivity matrix $\mathbf{R}_{surf}$ is given by[a.]

$$\mathbf{R}^{(xy)}_{surf} = \begin{pmatrix} \tilde{r}_{xx} & \tilde{r}_{xy} \\ \tilde{r}_{yx} & \tilde{r}_{yy} \end{pmatrix} \quad . \tag{2.4}$$

2.1.1.1 Incident wave with E oscillating in x-direction

For an incident electric field oscillating in the x-direction, $\mathbf{E} = (E_x, 0)$, the amplitude of the reflected wave $\mathbf{E}''$ is given by $(\tilde{r}_{xx}, \tilde{r}_{yx})E_x$. As the elements of $\mathbf{R}_{surf}$ are complex, i.e., $\mathbf{R}_{surf} \in \mathbb{C}^2 \times \mathbb{C}^2$, the reflected wave is elliptically polarized. For a further analysis it is convenient to represent $\mathbf{E}''$ in the basis set of the circular polarized waves,

$$\mathbf{E}'' = \frac{\tilde{a}_+}{2} \begin{pmatrix} 1 \\ +i \end{pmatrix} E_x + \frac{\tilde{a}_-}{2} \begin{pmatrix} 1 \\ -i \end{pmatrix} E_x \equiv \begin{pmatrix} \tilde{r}_{xx} \\ \tilde{r}_{yx} \end{pmatrix} E_x \quad , \tag{2.5}$$

[a.] In this chapter, tilde is used for complex quantities.

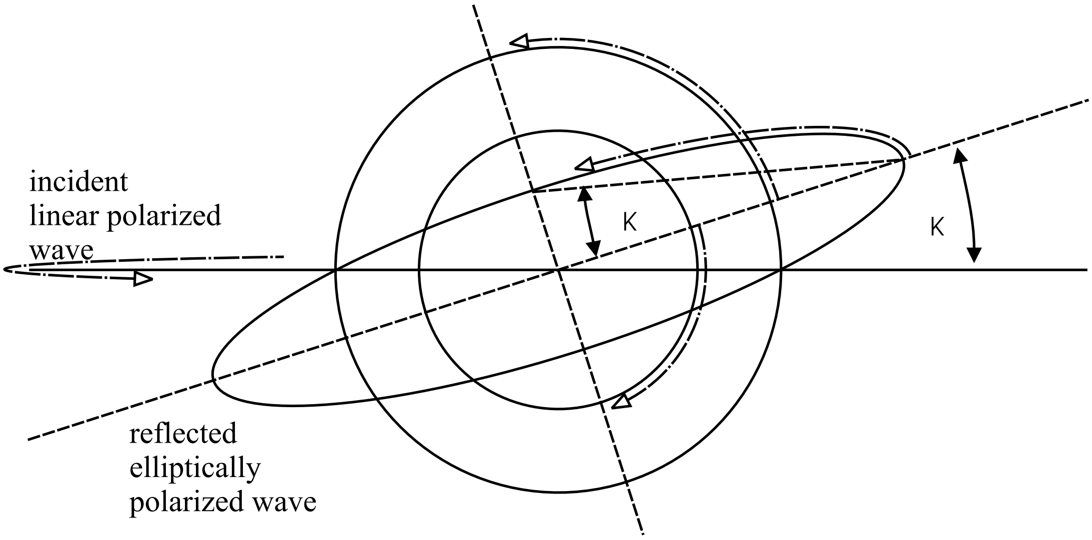

Figure 2.3: The incident linearly polarized beam is elliptically polarized upon reflection from a magnetic sample. The elliptically polarized light is decomposed into two circular polarized waves, drawn in the figure. The ellipsis is characterized by the Kerr rotation angle θ_K and the Kerr ellipticity angle ε_K. The polarization state of the incident light serves as the reference.

where the coefficients $\tilde{a}_\pm$ are given by

$$\tilde{a}_\pm = \tilde{r}_{xx} \mp i\tilde{r}_{yx} \equiv a_\pm e^{i\Delta_\pm} \quad , \quad \tilde{a}_\pm \in \mathbb{C} \quad , \quad a_\pm \in \mathbb{R} \quad , \quad \Delta_\pm \in \mathbb{R} \quad . \tag{2.6}$$

The radii of the circular polarized waves are the absolute values of $\tilde{a}_\pm$, the long and short axis of the ellipsis are given by $(a_+ + a_-)$ and $|a_+ - a_-|$, respectively. The phase factor $\Delta_\pm$ is the angle of the electric field with the x-axis at $t = 0$. The time evolution of the electric field vector $\mathbf{E}''$ describes the ellipsis, which, at $t = 0$ exhibits a phase shift of $\frac{1}{2}(\Delta_- - \Delta_+)$.

Thus, the Kerr rotation angle θ_K and Kerr ellipticity angle ε_K are given by

$$\theta_K = -\frac{1}{2}(\Delta_+ - \Delta_-) \quad , \quad \tan\Delta_\pm = \mathrm{Im}(\tilde{a}_\pm)/\mathrm{Re}(\tilde{a}_\pm) \quad , \tag{2.7}$$

$$\tan\varepsilon_K = \frac{|\tilde{a}_+| - |\tilde{a}_-|}{|\tilde{a}_+| + |\tilde{a}_-|} \quad . \tag{2.8}$$

2.1.1.2 Incident wave with $\mathbf{E}$ oscillating in y-direction

The reflected electric field vector $\mathbf{E}''$ for an incident wave with $\mathbf{E}$ oscillating in y-direction, $\mathbf{E} = (0, E_y)$, is decomposed in terms of circular waves as follows

$$\mathbf{E}'' = \frac{\tilde{b}_+}{2}\begin{pmatrix} 1 \\ +i \end{pmatrix} E_y + \frac{\tilde{b}_-}{2}\begin{pmatrix} 1 \\ -i \end{pmatrix} E_y \equiv \begin{pmatrix} r_{xy} \\ r_{yy} \end{pmatrix} E_y \quad , \tag{2.9}$$

where

$$\tilde{b}_{\pm} = \tilde{r}_{xy} \mp i\tilde{r}_{yy} \quad , \tag{2.10}$$

thus the MOKE is given by the equations (2.7) and (2.8) with $\tilde{a}_+$ and $\tilde{a}_-$ replaced by $\tilde{b}_+$ and $\tilde{b}_-$, respectively.

2.1.1.3 The polar magneto-optic Kerr effect

The obtained formulas should be compared to the literature for the case of a polar magnetization, ie., the magnetic moment $\mathbf{m}$ points along the surface normal, $\mathbf{m} = m_z \mathbf{e}_z$. Consequently, the elements of the reflectivity matrix become $\tilde{r}_{xx} = \tilde{r}_{yy}$ and $\tilde{r}_{xy} = -\tilde{r}_{yx}$ and the equations (2.6) and (2.10) reduce to

$$\tilde{a}_{\pm} = \tilde{r}_{xx} \pm i\tilde{r}_{xy} \tag{2.11}$$

with $\tilde{b}_{\pm} = \mp \tilde{a}_{\pm}$. Commonly, the expressions $\tilde{a}_{\pm}$ are then called $\tilde{r}_{\pm}$ [43].

2.2 Oblique incidence

If the incident light is not normal to the surface, the description of the beam's polarization in x- and y-coordinates is not recommended. Thus, polarization axes related to the direction of the beam, s and p, are introduced.

2.2.1 s- and p-waves

In the case of oblique incident light, $\mathbf{E}$ is no longer restricted to the xy-plane, it is strongly recommended to chose a different coordinate system. p lies in the plane of incidence and s is orthogonal to the latter. A third orthogonal direction d is introduced lying in the plane of incidence orthogonal to p. It is not evident that d coincides with the wave vector as in a magnetic medium $\mathbf{E}$ and $\mathbf{k}$ are not necessarily orthogonal. Only in vacuum (or a paramagnetic medium) is the polarization plane orthogonal to $\mathbf{k}$, thus p, s and $\mathbf{k}$ (coincident with d then) form a pairwise orthogonal system.

With the following form of the surface reflectivity matrix $\mathbf{R}^{(sp)}_{surf}$,

$$\mathbf{R}^{(sp)}_{surf} = \begin{pmatrix} \tilde{r}_{pp} & \tilde{r}_{ps} \\ \tilde{r}_{sp} & \tilde{r}_{ss} \end{pmatrix} \quad , \tag{2.12}$$

for an incident p-wave the coefficients $\tilde{a}_{\pm}$ are given by

$$\tilde{a}_{\pm} = \tilde{r}_{pp} \mp i\tilde{r}_{sp} \quad , \tag{2.13}$$

and for an incident s-wave the coefficients $\tilde{b}_{\pm}$ are given by

$$\tilde{b}_{\pm} = \tilde{r}_{ps} \mp i\tilde{r}_{ss} \quad , \tag{2.14}$$

such that for the MOKE equations (2.7) and (2.8) apply.

In the exact a-initio calculations the MOKE was computed according to equations (2.7) and (2.8). For reasons of comparability with the literature, the approximative two-media formulas are derived for the Kerr rotation and ellipticity angles. These are presented and compared to the formulas derived in the present chapter in appendix B.

3 Reflection: The two-media approach

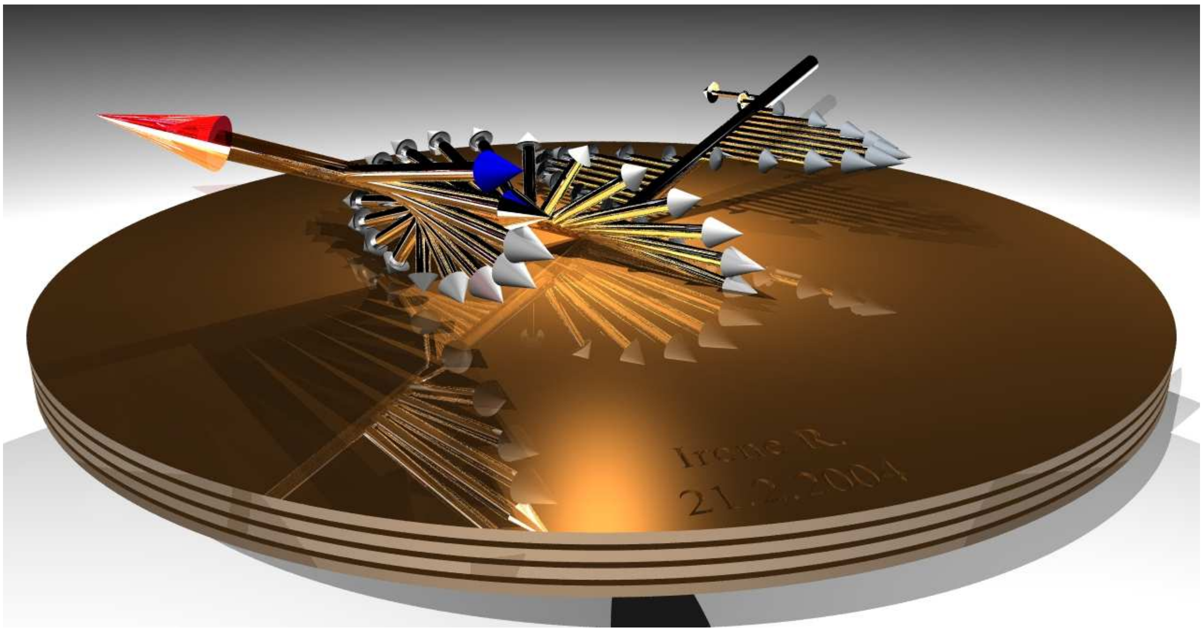

At the interface between two media, for an electromagnetic wave the boundary conditions for the electric field **E**, the magnetic field **H**, the electric induction **D** and the magnetic induction **B** have to be satisfied. The permeability μ in the regime of visible light is approximately 1, thus $\mathbf{B} \approx \mathbf{H}$ (Landau hypothesis).

In the following the global coordinate system is chosen such that the surface normal is parallel to the unitary vector $\mathbf{e}_z$ of the z-axis. Incident components will be denoted as bare quantities, refracted components with prime and reflected components with double prime. The electromagnetic wave obeying the Maxwell equations has to be determined so that the boundary conditions,

$$\varepsilon(\mathbf{E}+\mathbf{E}^{''})\cdot\mathbf{e}_z = \varepsilon^{'}\mathbf{E}^{'}\cdot\mathbf{e}_z \quad , \tag{3.1}$$

$$\mu(\mathbf{H}+\mathbf{H}^{''})\cdot\mathbf{e}_z = \mu^{'}\mathbf{H}^{'}\cdot\mathbf{e}_z \quad , \tag{3.2}$$

$$(\mathbf{E}+\mathbf{E}^{''})\times\mathbf{e}_z = \mathbf{E}^{'}\times\mathbf{e}_z \quad , \tag{3.3}$$

$$(\mathbf{H}+\mathbf{H}^{''})\times\mathbf{e}_z = \mathbf{H}^{'}\times\mathbf{e}_z \quad , \tag{3.4}$$

hold for all times t and all for all points $\mathbf{r}$. The conditions are examined for plane waves,

$$\mathbf{E} = \mathbf{E}_0 e^{i(\mathbf{qr}-\omega t)} \quad , \quad \mathbf{q} = \frac{\omega}{c} n \boldsymbol{\kappa} \quad , \quad \mathbf{q}^{''} = \frac{\omega^{''}}{c} n \boldsymbol{\kappa}^{''} \quad , \quad \mathbf{q}^{'}_{\pm} = \frac{\omega^{'}_{\pm}}{c} n^{'}_{\pm} \boldsymbol{\kappa}^{'}_{\pm} \quad , \tag{3.5}$$

where $\mathbf{q}$ is the wave vector, $\boldsymbol{\kappa}$ a unitary vector parallel to $\mathbf{q}$, n the (complex) refractive index of the medium, c the speed of light in vacuum and ω the frequency. The Maxwell equations yield conditions for the phase shifts and for the amplitudes of the waves, the former leading to the kinematic properties of reflection which are called the Snell's law, the latter to the dynamic properties called the Fresnel equations.

3.1 Kinematic properties: Snell's law

For all points in the plane $z = 0$ the boundary conditions are time independent. This applies to the frequencies,

$$\omega = \omega^{''} = \omega^{'}_{\pm} \quad , \tag{3.6}$$

and for the wave vectors $\mathbf{k}$,

$$(\boldsymbol{\kappa} \cdot \mathbf{r})_{z=0} = -(\boldsymbol{\kappa}^{''} \cdot \mathbf{r})_{z=0} \quad , \quad (n\boldsymbol{\kappa} \cdot \mathbf{r})_{z=0} = (n^{'}_{\pm} \boldsymbol{\kappa}^{'}_{\pm} \cdot \mathbf{r})_{z=0} \quad . \tag{3.7}$$

Provided that the refractive indices are real numbers, a geometric interpretation is possible. Assuming the xz-plane as the plane of incidence, the directions of the incident, reflected and refracted beams are given by

$$\boldsymbol{\kappa} = (\sin\alpha, 0, \cos\alpha) \quad , \quad \boldsymbol{\kappa}^{''} = (\sin\alpha^{''}, 0, -\cos\alpha^{''}) \quad , \quad \boldsymbol{\kappa}^{'}_{\pm} = (\sin\alpha^{'}_{\pm}, 0, \cos\alpha^{'}_{\pm}) \quad . \tag{3.8}$$

Then equations (3.7) yield the well-known form of Snell's law,

$$\alpha = \alpha^{''} \quad \text{and} \quad n \sin\alpha = n^{\prime}_{\pm} \sin\alpha^{\prime}_{\pm} \quad , \tag{3.9}$$

where α is the angle between the incident beam, $\alpha^{''}$ the angle between the reflected beam, and $\alpha^{'}_{\pm}$ the angles between the refracted beams and the surface normal. In case of damped waves, the complex refractive index $n^{\prime}_{\pm}$ in equations (3.9) will lead to complex angles $\alpha^{\prime}_{\pm}$. Even though a geometric interpretation is not obvious, the description is correct mathematically. The trigonometric functions were introduced for convenience and the interpretation as angles is not necessary.

3.2 Dynamic properties: Fresnel equations

3.2.1 The Fresnel equation for a magnetic medium

In Section 3.2.1 of this chapter normal modes of a wave propagating in a magnetic medium are calculated, in Section 3.3 boundary conditions for the polar (P-MOKE) and in Section 3.4 those for the longitudinal (L-MOKE) configuration are considered. In Section 3.5 the properties of the obtained formulas will be discussed.

Finally, in Section 10.5.1.1 a comparison between the angle-of-incidence-dependent ab-initio results including multiple reflections and interferences with the results based on the 2-media approach are carried out.

We start with the Maxwell equations and the linear material equations[a.]

$$\epsilon_{ijk}\partial_j E_k = -\frac{1}{c}\partial_0 H_i \quad , \tag{3.10}$$

$$\epsilon_{ijk}\partial_j H_k = \frac{4\pi}{c} j_i + \frac{e}{c}\partial_0 D_i \quad , \tag{3.11}$$

$$\mathbf{D} = \boldsymbol{\varepsilon}\mathbf{E} \quad . \tag{3.12}$$

For vanishing external charges and currents these two Maxwell equations become

$$\epsilon_{lmi}\partial_m \epsilon_{ijk}\partial_j E_k = -\frac{1}{c}\partial_0 \epsilon_{lmi}\partial_m H_i \quad , \tag{3.13}$$

$$\epsilon_{lmi}\partial_m H_i = \frac{e}{c}\partial_0 D_l \quad . \tag{3.14}$$

Inserting equation (3.14) into equation (3.13) and using the multiplication law of the totally antisymmetric Levi Civita tensor gives

$$(\delta_{lj}\delta_{mk} - \delta_{lk}\delta_{mj})\partial_m\partial_j E_k = -\frac{e}{c^2}\partial_0\partial_0 D_l \quad . \tag{3.15}$$

For plane waves,

$$E_k = E_{k0}e^{i(q_n r_n - \omega t)} \quad , \quad D_k = \varepsilon_{kj}E_j \quad , \quad q_n = \frac{\omega}{c} n \kappa_n \quad , \tag{3.16}$$

the Fresnel equation is given by,

$$n^2(\kappa_l\kappa_k - \delta_{lk})E_k + \varepsilon_{lk}E_k = 0 \quad . \tag{3.17}$$

As a consequence of the Maxwell equations[b.] the vectors **D**, **H**, and $\boldsymbol{\kappa}$ are pairwise orthogonal. If the dielectric tensor $\boldsymbol{\varepsilon}$ is non-scalar, **E** and $\boldsymbol{\kappa}$ are not necessarily orthogonal. Thus, provided that the inverse of the dielectric matrix ($\boldsymbol{\varepsilon}^{-1}$) exists (none of the eigenvalues of $\boldsymbol{\varepsilon}$ must be 0), it is convenient to solve the Fresnel equation in terms of **D**,

$$\mathbf{D} = n^2(\mathbf{E} - \boldsymbol{\kappa}(\boldsymbol{\kappa}\cdot\mathbf{E})) = n^2(\boldsymbol{\varepsilon}^{-1}\mathbf{D} - \boldsymbol{\kappa}(\boldsymbol{\kappa}\cdot\boldsymbol{\varepsilon}^{-1}\mathbf{D})) \quad . \tag{3.18}$$

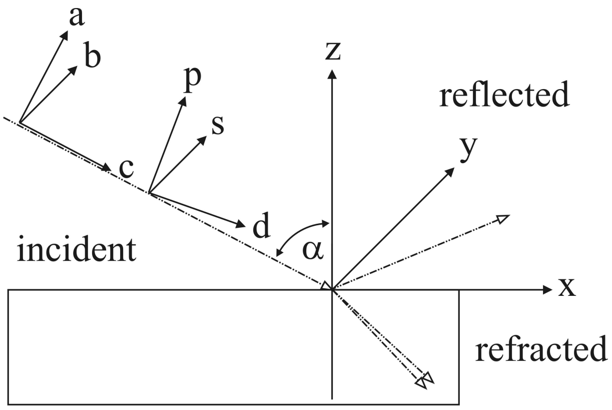

Figure 3.1: The orthonormal coordinate systems *(xyz)*, *(abc)*, and *(spd)*. s is orthogonal to the plane of incidence which is spanned by the axis p and d. p is not necessarily transversal to the propagation direction of the beam, implying that d does not coincide with the propagation direction.

3.2.2 Arbitrary angle between the magnetic field and the photon beam

3.2.2.1 Choice of the Cartesian coordinate system

As a uniform magnetization in z-direction is assumed, the dielectric tensor is given by

$$\boldsymbol{\varepsilon} = \begin{pmatrix} \varepsilon_{xx} & \varepsilon_{xy} & 0 \\ -\varepsilon_{xy} & \varepsilon_{yy} & 0 \\ 0 & 0 & \varepsilon_{zz} \end{pmatrix} \quad . \tag{3.19}$$

The beam and the magnetization form an angle α, see Fig. 3.1. Here, the coordinates (a, b, c) of the beam should be introduced, where c is the direction of the wave vector, $\boldsymbol{\kappa}$, and a and b are orthogonal directions. a lies in the plane of incidence, b is orthogonal to the latter and is parallel to the y-axis and the later to be explained s-axis.

In the Fresnel equation for $\mathbf{D}$ the inverted dielectric tensor, $\boldsymbol{\varepsilon}^{-1}$, appears. The transformation into the new coordinates (a, b, c) is performed by $(\boldsymbol{\varepsilon}^{-1})_{abc} = \mathbf{S}^{-1}\boldsymbol{\varepsilon}^{-1}\mathbf{S}$ where

$$\mathbf{S} = \begin{pmatrix} \cos\alpha & 0 & \sin\alpha \\ 0 & 1 & 0 \\ -\sin\alpha & 0 & \cos\alpha \end{pmatrix} \tag{3.20}$$

is a $3D$ rotation matrix.

---

[a] For better readability in the derivation of the Fresnel equations the Einstein conventions are in use, where the arabic indices denote the space-like coordinates and ∂_0 the time derivative.

[b] If there are no free charges ρ or free currents $\mathbf{j}$ present, the following relations apply: $\rightarrow 0 = \boldsymbol{\kappa}\mathbf{B} \approx \boldsymbol{\kappa}\mathbf{H}$, $\boldsymbol{\kappa}.\mathbf{D} = 0$, $\boldsymbol{\kappa} \times \mathbf{H} = \omega\mathbf{D}/c$, $\boldsymbol{\kappa} \times \mathbf{E} = -\omega\mathbf{B}/c \approx -\omega\mathbf{H}/c$, $\mathbf{D} = \boldsymbol{\varepsilon}\mathbf{E}$.

In the coordinate system (a, b, c) the Fresnel equation simplifies since $\mathbf{D} \perp \boldsymbol{\kappa}$ and $c \parallel \boldsymbol{\kappa}$ and the third component of $\mathbf{D}$, D_c, vanishes,

$$\mathbf{D} = n^2(\boldsymbol{\varepsilon}^{-1}\mathbf{D} - \mathbf{e}_c(\mathbf{e}_c \cdot \boldsymbol{\varepsilon}^{-1}\mathbf{D})) \quad , \tag{3.21}$$

$$D_a = n^2((\boldsymbol{\varepsilon}^{-1})_{aa}D_a + (\boldsymbol{\varepsilon}^{-1})_{ab}D_b) \quad , \tag{3.22}$$

$$D_b = n^2((\boldsymbol{\varepsilon}^{-1})_{ba}D_a + (\boldsymbol{\varepsilon}^{-1})_{bb}D_b) \quad , \tag{3.23}$$

$$D_c = n^2((\boldsymbol{\varepsilon}^{-1})_{ca}D_a + (\boldsymbol{\varepsilon}^{-1})_{cb}D_b - (\boldsymbol{\varepsilon}^{-1})_{ca}D_a - (\boldsymbol{\varepsilon}^{-1})_{cb}D_b) = 0 \quad . \tag{3.24}$$

Here, $\mathbf{e}_c$ is the unit vector in the direction of the c-axis. The elements of the reduced 2×2 matrix $\boldsymbol{\varepsilon}$,

$$\begin{pmatrix} (\boldsymbol{\varepsilon}^{-1})_{aa} & (\boldsymbol{\varepsilon}^{-1})_{ab} \\ (\boldsymbol{\varepsilon}^{-1})_{ba} & (\boldsymbol{\varepsilon}^{-1})_{bb} \end{pmatrix} \quad , \tag{3.25}$$

are given by

$$(\boldsymbol{\varepsilon}^{-1})_{aa} = (\boldsymbol{\varepsilon}^{-1})_{xx}\cos^2\alpha + (\boldsymbol{\varepsilon}^{-1})_{zz}\sin^2\alpha = \frac{\varepsilon_{xx}}{\varepsilon_{xx}^2 + \varepsilon_{xy}^2}\cos^2\alpha + \frac{\sin^2\alpha}{\varepsilon_{zz}} \quad , \tag{3.26}$$

$$(\boldsymbol{\varepsilon}^{-1})_{ab} = (\boldsymbol{\varepsilon}^{-1})_{xy}\cos\alpha = -\frac{\varepsilon_{xy}}{\varepsilon_{xx}^2 + \varepsilon_{xy}^2}\cos\alpha \quad , \tag{3.27}$$

$$(\boldsymbol{\varepsilon}^{-1})_{ba} = (\boldsymbol{\varepsilon}^{-1})_{yx}\cos\alpha = \frac{\varepsilon_{xy}}{\varepsilon_{xx}^2 + \varepsilon_{xy}^2}\cos\alpha \quad , \tag{3.28}$$

$$(\boldsymbol{\varepsilon}^{-1})_{bb} = (\boldsymbol{\varepsilon}^{-1})_{yy} = \frac{\varepsilon_{xx}}{\varepsilon_{xx}^2 + \varepsilon_{xy}^2} \quad . \tag{3.29}$$

The system of equations for $\mathbf{D}$,

$$0 = (n^2(\boldsymbol{\varepsilon}^{-1})_{aa} - 1)D_a + n^2(\boldsymbol{\varepsilon}^{-1})_{ab}D_b \quad , \tag{3.30}$$

$$0 = n^2(\boldsymbol{\varepsilon}^{-1})_{ba}D_a + (n^2(\boldsymbol{\varepsilon}^{-1})_{bb} - 1)D_b \quad , \tag{3.31}$$

has a solution if the determinant of the coefficients vanishes. This condition yields a biquadratic equation in the refractive index n,

$$n^4\left(\frac{\varepsilon_{xx}\varepsilon_{zz}\cos^2\alpha + (\varepsilon_{xx}^2 + \varepsilon_{xy}^2)\sin^2\alpha + \varepsilon_{zz}\varepsilon_{xy}^2\cos^2\alpha}{\varepsilon_{zz}(\varepsilon_{xx}^2 + \varepsilon_{xy}^2)^2}\right) \\ - n^2\left(\frac{\varepsilon_{xx}\varepsilon_{zz}\cos^2\alpha + (\varepsilon_{xx}^2 + \varepsilon_{xy}^2)\sin^2\alpha + \varepsilon_{zz}\varepsilon_{xx}}{\varepsilon_{zz}(\varepsilon_{xx}^2 + \varepsilon_{xy}^2)}\right) + 1 = 0 \quad .$$

With identical diagonal elements, ε_{xx} and ε_{zz}, and anti-symmetric off-diagonal elements $\varepsilon_{xy} = -\varepsilon_{yx}$ assumed, this implies

$$n^4 - n^2\frac{2\varepsilon_{xx}^2 + \varepsilon_{xy}^2\sin^2\alpha}{\varepsilon_{xx}} + (\varepsilon_{xx}^2 + \varepsilon_{xy}^2) = 0 \quad . \tag{3.32}$$

In the linear approximation in ε_{xy}, the two solutions for n^2 are given by[c.],

$$n_\pm^2 \approx \varepsilon_{xx} \pm i\varepsilon_{xy}\cos\alpha + \frac{\varepsilon_{xy}^2}{2\varepsilon_{xx}}\sin^2\alpha \quad . \tag{3.36}$$

As the two equations (3.30) and (3.31) are linearly dependent, either one suffices in calculating the corresponding electric induction $\mathbf{D}_\pm$. Again in the linear approximation in ε_{xy}, equation (3.31) yields,

$$\begin{aligned} D_{a\pm} &= \frac{\varepsilon_{xx}^2+\varepsilon_{xy}^2}{n^2\varepsilon_{xy}\cos\alpha}\left(1-\frac{n^2\varepsilon_{xx}}{\varepsilon_{xx}^2+\varepsilon_{xy}^2}\right)D_{b\pm} && (3.37)\\ &= \frac{1}{n^2\varepsilon_{xy}\cos\alpha}\left(\varepsilon_{xx}^2+\varepsilon_{xy}^2-n^2\varepsilon_{xx}\right)D_{b\pm} \quad , && (3.38)\\ D_{a\pm} &= \frac{1}{n^2\cos\alpha}\left(\varepsilon_{xy}(1-\frac{1}{2}\sin^2\alpha)\mp i\varepsilon_{xx}\cos\alpha\right)D_{b\pm} \quad . && (3.39)\end{aligned}$$

In a first order approximation, the expression in the brackets is at least linear in ε_{xy}, the numerator has to be approximated in zeroth order in ε_{xy}, giving

$$\begin{aligned} (n^2\cos\alpha)^{-1} &= \left(\varepsilon_{xx}\cos\alpha(1\pm i\frac{\varepsilon_{xy}\cos\alpha}{\varepsilon_{xx}}+\frac{\varepsilon_{xy}^2}{2\varepsilon_{xx}^2}\sin^2\alpha)\right)^{-1} && (3.40)\\ &\approx \frac{1}{\varepsilon_{xx}\cos\alpha}(1\mp i\frac{\varepsilon_{xy}}{\varepsilon_{xx}}\cos\alpha) \quad , && (3.41)\end{aligned}$$

which implies for the components of $\mathbf{D}$,

$$\begin{aligned} D_{a\pm} &\approx \frac{1}{\varepsilon_{xx}\cos\alpha}\left(\frac{\varepsilon_{xy}}{2}(1-\cos^2\alpha)\mp i\varepsilon_{xx}\cos\alpha\right)D_{b\pm} \quad , \\ &= \left(\frac{\varepsilon_{xy}\sin^2\alpha}{2\varepsilon_{xx}\cos\alpha}\mp i\right)D_{b\pm} \quad , && (3.42)\\ D_{c\pm} &= 0 \quad . && (3.43)\end{aligned}$$

In order to obtain $E_{a\pm}(E_{b\pm})$ and $E_{c\pm}(E_{b\pm})$ the relation $\mathbf{E} = \varepsilon^{-1}\mathbf{D}$ is exploited. With

---

[c.]

$$\begin{aligned} n_\pm^2 &= \frac{2\varepsilon_{xx}^2+\varepsilon_{xy}^2\sin^2\alpha \pm \sqrt{\varepsilon_{xy}^4\sin^4\alpha - 4\varepsilon_{xx}^2\varepsilon_{xy}^2\cos^2\alpha}}{2\varepsilon_{xx}} && (3.33)\\ &= \varepsilon_{xx}+\frac{\varepsilon_{xy}^2}{2\varepsilon_{xx}}\sin^2\alpha \pm \frac{\sqrt{-4\varepsilon_{xx}^2\varepsilon_{xy}^2\cos^2\alpha}}{2\varepsilon_{xx}}\sqrt{1-\frac{\varepsilon_{xy}^4\sin^4\alpha}{4\varepsilon_{xx}^2\varepsilon_{xy}^2\cos^2\alpha}} && (3.34)\\ &\approx \varepsilon_{xx}+\frac{\varepsilon_{xy}^2}{2\varepsilon_{xx}}\sin^2\alpha \pm i\varepsilon_{xy}\cos\alpha\left(1-\frac{\varepsilon_{xy}^4\sin^4\alpha}{8\varepsilon_{xx}^2\varepsilon_{xy}^2\cos^2\alpha}\right) && (3.35)\end{aligned}$$

$\varepsilon_{xx} = \varepsilon_{zz}$ and a linear approximation in ε_{xy} and $(\varepsilon^{-1})_{ca}$ and $(\varepsilon^{-1})_{cb}$,

$$(\boldsymbol{\varepsilon}^{-1})_{ca} = \left(\frac{\varepsilon_{xx}}{\varepsilon_{xx}^2 + \varepsilon_{xy}^2} - \frac{1}{\varepsilon_{zz}}\right)\sin\alpha\cos\alpha \quad , \tag{3.44}$$

$$(\boldsymbol{\varepsilon}^{-1})_{cb} = -\frac{\varepsilon_{xy}}{\varepsilon_{xx}^2 + \varepsilon_{xy}^2}\sin\alpha \quad . \tag{3.45}$$

the following relations for the components of the electric field amplitude are obtained

$$E_{a\pm} = \frac{\varepsilon_{xx}^2 + \varepsilon_{xy}^2\sin^2\alpha}{\varepsilon_{xx}(\varepsilon_{xx}^2 + \varepsilon_{xy}^2)} D_{a\pm} - \frac{\varepsilon_{xy}}{\varepsilon_{xx}^2 + \varepsilon_{xy}^2}\cos\alpha D_{b\pm} \quad , \tag{3.46}$$

$$E_{b\pm} = \frac{\varepsilon_{xy}}{\varepsilon_{xx}^2 + \varepsilon_{xy}^2}\cos\alpha D_{a\pm} + \frac{\varepsilon_{xx}}{\varepsilon_{xx}^2 + \varepsilon_{xy}^2} D_{b\pm} \quad , \tag{3.47}$$

$$E_{c\pm} = \left(\frac{\varepsilon_{xx}}{\varepsilon_{xx}^2 + \varepsilon_{xy}^2} - \frac{1}{\varepsilon_{xx}}\right)\sin\alpha\cos\alpha D_{a\pm} - \frac{\varepsilon_{xy}}{\varepsilon_{xx}^2 + \varepsilon_{xy}^2}\sin\alpha D_{b\pm} \quad . \tag{3.48}$$

$D_{a\pm}$ is eliminated by inserting equation (3.42) which gives $D_{a\pm}$ as a function of $D_{b\pm}$ into equations (3.46) - (3.48),

$$E_{a\pm} = \left(\frac{\varepsilon_{xx}^2 + \varepsilon_{xy}^2\sin^2\alpha}{\varepsilon_{xx}(\varepsilon_{xx}^2 + \varepsilon_{xy}^2)}\left(\frac{\varepsilon_{xy}\sin^2\alpha}{2\varepsilon_{xx}\cos\alpha} \mp i\right) - \frac{\varepsilon_{xy}}{\varepsilon_{xx}^2 + \varepsilon_{xy}^2}\cos\alpha\right) D_{b\pm} \quad , \tag{3.49}$$

$$D_{b\pm} = \left(\frac{\varepsilon_{xy}}{\varepsilon_{xx}^2 + \varepsilon_{xy}^2}\cos\alpha\left(\frac{\varepsilon_{xy}\sin^2\alpha}{2\varepsilon_{xx}\cos\alpha} \mp i\right) + \frac{\varepsilon_{xx}}{\varepsilon_{xx}^2 + \varepsilon_{xy}^2}\right)^{-1} E_{b\pm} \quad , \tag{3.50}$$

$$E_{c\pm} = \left(\left(\frac{\varepsilon_{xx}}{\varepsilon_{xx}^2 + \varepsilon_{xy}^2} - \frac{1}{\varepsilon_{xx}}\right)\left(\frac{\varepsilon_{xy}\sin^2\alpha}{2\varepsilon_{xx}\cos\alpha} \mp i\right)\cos\alpha - \frac{\varepsilon_{xy}}{\varepsilon_{xx}^2 + \varepsilon_{xy}^2}\right)\sin\alpha D_{b\pm} \quad . \tag{3.51}$$

Equation (3.50) to first order in ε_{xy} yields $D_{b\pm}$,

$$D_{b\pm} \approx \frac{\varepsilon_{xx}^2 + \varepsilon_{xy}^2}{\varepsilon_{xx}}\left(1 \pm i\frac{\varepsilon_{xy}}{\varepsilon_{xx}}\cos\alpha\right) E_{b\pm} \quad . \tag{3.52}$$

which is inserted into $E_{a\pm}(D_{b\pm})$ and $E_{c\pm}(D_{b\pm})$.

In the consecutive chapters, reflection in a system with two homogeneous media will be discussed. The two normal modes of the refracted wave will be indicated as $\mathbf{E}'_+$ and $\mathbf{E}'_-$. Corresponding to the refractive indices $n_\pm$, the refractive angles $\alpha'_\pm$ are given by Snell's law. Thus, $E'_{a\pm}$ and $E'_{c\pm}$ are are given by,

$$E'_{a\pm} \approx \left(\frac{\varepsilon_{xy}\sin^2\alpha'_\pm}{2\varepsilon_{xx}\cos\alpha'_\pm} \mp i\right) E'_{b\pm} \quad , \tag{3.53}$$

$$E'_{c\pm} \approx -\frac{\varepsilon_{xy}\sin\alpha'_\pm}{\varepsilon_{xx}} E'_{b\pm} \quad . \tag{3.54}$$

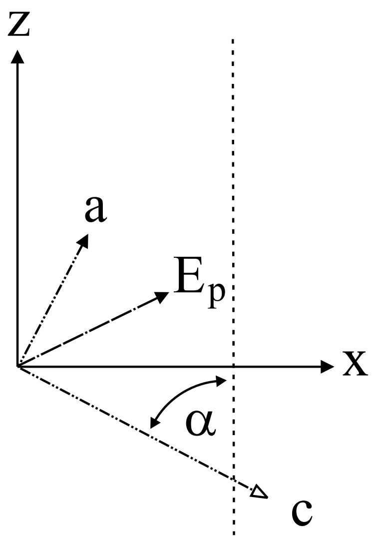

Figure 3.2: The incoming beam is described by the coordinates (a, b, c), where c is the propagation direction of light. The global coordinate system is (x, y, z) and the surface is terminated by a plane at $z = 0$.

3.3 Boundary conditions for the polar magneto-optic Kerr effect (P-MOKE)

In polar geometry the magnetization axis is parallel to the surface normal and therefore the angle $\alpha'_{\pm}$ in the equations (3.53) and (3.54) between the propagation direction of the beam and the magnetization is the same as the angle of incidence.

At the boundary between the two media the normal-to-plane components $D_{\perp}$ and $B_{\perp}$ and the in-plane components $\mathbf{E}_{||}$ and $\mathbf{H}_{||}$ have to be continuous.[d.] $\mathbf{E}$ is best described in the coordinates (abc), see Fig. 3.1. s is orthogonal to the plane of incidence and thus parallel to the surface, the p-wave is in the plane of incidence and at an oblique angle to the surface, i.e., $\mathbf{E}_p = E_a\mathbf{e}_a + E_c\mathbf{e}_c$. If the plane of incidence is the xz-plane, the correspondence between the different basis sets is given by

$$E_x = \mathbf{E}_p \cdot \mathbf{e}_x = E_a \cos\alpha + E_c \sin\alpha \qquad \rightarrow \quad \in \mathbf{E}_{||} \quad , \tag{3.55}$$

$$E_y = \mathbf{E}_s \cdot \mathbf{e}_y = E_b \qquad \rightarrow \quad \in \mathbf{E}_{||} \quad , \tag{3.56}$$

$$E_z = \mathbf{E}_p \cdot \mathbf{e}_z = E_a \sin\alpha - E_c \cos\alpha \qquad \rightarrow \quad \in E_{\perp} \quad , \tag{3.57}$$

see Fig. 3.2. In vacuum, the component E_c vanishes and therefore $\mathbf{E}_p$ encloses an angle $(90^0 - \alpha)$ with the surface normal, thus $E_x = E_p \cos\alpha$. At the boundary between a para(non)-magnetic medium and a magnetic medium we consider an incident and a reflected wave in the para-magnetic (vacuum) and left- and right-polarized refracted waves

---

[d.] The Maxwell equations imply the continuity of the following components at the boundary between two media, Div$\mathbf{D} = 0 \rightarrow D_{\perp}$, Div$\mathbf{B} = 0 \rightarrow B_{\perp}$, Rot$\mathbf{E} = 0 \rightarrow \mathbf{E}_{||}$, and Rot$\mathbf{H} = 0 \rightarrow \mathbf{H}_{||}$.

in the magnetic medium. The incident wave is denoted as E_p and E_s, the refracted as $E'_{p\pm}$ and $E'_{s\pm}$, and the reflected as $E^{''}_p$ and $E^{''}_s$,

$$\mathbf{E} = \begin{pmatrix} E_x \\ E_y \\ E_z \end{pmatrix} \quad , \quad \mathbf{E}'_\pm = \begin{pmatrix} E'_{x\pm} \\ E'_{y\pm} \\ E'_{z\pm} \end{pmatrix} \quad , \quad \text{and} \quad \mathbf{E}^{''} = \begin{pmatrix} -E^{''}_x \\ E^{''}_y \\ E^{''}_z \end{pmatrix} \quad . \tag{3.58}$$

In a magnetic medium the absolute value of the p-component of the refracted wave is given by

$$|\mathbf{E}_{p\pm}| = \pm\sqrt{E^2_{a\pm} + E^2_{c\pm}} = \pm E_{s\pm}\sqrt{\left(\frac{\varepsilon_{xy}\sin^2\alpha_\pm}{2\varepsilon_{xx}\cos\alpha_\pm} \mp i\right)^2 + \left(\frac{\varepsilon_{xy}\sin\alpha_\pm}{\varepsilon_{xx}}\right)^2} \quad , \tag{3.59}$$

the two refracted circular components are therefore given by

$$E'_{p\pm} \approx \left(\pm i - \frac{\varepsilon_{xy}\sin^2\alpha'_\pm}{2\varepsilon_{xx}\cos\alpha'_\pm}\right) E'_{s\pm} \quad . \tag{3.60}$$

In the same manner $E_{x\pm}$ and $E_{z\pm}$ are derived

$$E_{x\pm} = \left(-\frac{\varepsilon_{xy}\sin^2\alpha_\pm}{2\varepsilon_{xx}\cos\alpha_\pm} \mp i\right)\cos\alpha_\pm E_{s\pm} \quad , \tag{3.61}$$

$$E_{z\pm} = \left(\frac{\varepsilon_{xy}(1+\cos^2\alpha_\pm)}{2\varepsilon_{xx}\cos\alpha_\pm} \mp i\right)\sin\alpha_\pm E_{s\pm} \quad . \tag{3.62}$$

The condition for the tangential components $E_{\|}$ gives the following expressions

$$\cos\alpha(E_p - E^{''}_p) = \sum_\pm \left(-\frac{\varepsilon_{xy}\sin^2\alpha'_\pm}{2\varepsilon_{xx}\cos\alpha'_\pm} \mp i\right)\cos\alpha'_\pm E'_{s\pm} \quad , \tag{3.63}$$

$$E_s + E^{''}_s = \sum_\pm E'_{s\pm} \quad . \tag{3.64}$$

The magnetic field $\mathbf{H}$ is given by $\mathbf{H} = n\boldsymbol{\kappa} \times \mathbf{E}$, the wave vectors by

$$n\boldsymbol{\kappa} = n\begin{pmatrix} \sin\alpha \\ 0 \\ -\cos\alpha \end{pmatrix} \quad , \quad n'_\pm\boldsymbol{\kappa}' = n'_\pm\begin{pmatrix} \sin\alpha'_\pm \\ 0 \\ -\cos\alpha'_\pm \end{pmatrix} \quad , \quad n\boldsymbol{\kappa}^{''} = n\begin{pmatrix} \sin\alpha \\ 0 \\ \cos\alpha \end{pmatrix} \quad .$$

Note that there exist 4 solutions for n' in the medium, two travelling downwards and two upwards. Here $n'_\pm$ denote only the two downwards travelling waves. Therefore the magnetic field $\mathbf{H}$ becomes

$$\mathbf{H} = n\begin{pmatrix} \cos\alpha E_y \\ -\cos\alpha E_x - \sin\alpha E_z \\ \sin\alpha E_y \end{pmatrix} \quad , \quad \mathbf{H}' = n'_\pm\begin{pmatrix} \cos\alpha'_\pm E'_{y\pm} \\ -\cos\alpha'_\pm E'_{x\pm} - \sin\alpha'_\pm E'_{z\pm} \\ \sin\alpha'_\pm E'_{y\pm} \end{pmatrix} \quad ,$$

$$\mathbf{H}^{''} = n\begin{pmatrix} -\cos\alpha E^{''}_y \\ -\cos\alpha E^{''}_x - \sin\alpha E^{''}_z \\ \sin\alpha E^{''}_y \end{pmatrix} \quad .$$

The y-component can be simplified and becomes in vacuum

$$\begin{aligned} n(-\cos\alpha E_x - \sin\alpha E_z - \cos\alpha E_x'' - \sin\alpha E_z'') = \\ &= n(-E_p\cos^2\alpha - E_p\sin^2\alpha - \cos^2\alpha E_x'' - \sin^2\alpha E_z'') \\ &= -n(E_p + E_p'') \end{aligned}$$

and the assumed homogeneous medium

$$\sum_\pm n_\pm'(-\cos\alpha_\pm' E_{x\pm}' - \sin\alpha_\pm' E_{z\pm}') = -\sum_\pm n_\pm' E_{a\pm}' \approx \sum_\pm n_\pm' E_{p\pm}' \quad .$$

The continuity of the tangential components of $\mathbf{H}$ yields for H_x (with $E_y = E_s$) and H_y

$$n\cos\alpha(E_s - E_s'') = \sum_\pm n_\pm' \cos\alpha_\pm' E_{s\pm}' \quad , \tag{3.65}$$

$$n(E_p + E_p'') = \sum_\pm n_\pm' \left(\frac{\varepsilon_{xy}\sin^2\alpha_\pm'}{2\varepsilon_{xx}\cos\alpha_\pm'} \mp i\right) E_{s\pm}' \quad . \tag{3.66}$$

The equations ((3.63)-(3.66)) summarize the relations between incident, refracted and reflected waves which are valid at the boundary between a magnetic and a non-magnetic medium. Assuming an incident s-wave (p-wave) $\tilde{r}_{ps}$ and $\tilde{r}_{ss}$ ($\tilde{r}_{sp}$ and $\tilde{r}_{pp}$) can be calculated.

3.3.1 Incident s-wave: $E_p = 0$

$$E_s + E_s'' = \sum_\pm E_{s\pm}' \quad , \tag{3.67}$$

$$-\cos\alpha E_p'' = \sum_\pm \left(-\frac{\varepsilon_{xy}\sin^2\alpha_\pm'}{2\varepsilon_{xx}\cos\alpha_\pm'} \mp i\right)\cos\alpha_\pm' E_{s\pm}' \quad , \tag{3.68}$$

$$n\cos\alpha(E_s - E_s'') = \sum_\pm n_\pm' \cos\alpha_\pm' E_{s\pm}' \quad , \tag{3.69}$$

$$nE_p'' = \sum_\pm n_\pm' \left(\frac{\varepsilon_{xy}\sin^2\alpha_\pm'}{2\varepsilon_{xx}\cos\alpha_\pm'} \mp i\right) E_{s\pm}' \quad . \tag{3.70}$$

This system of equations is solved, first by calculating $E_{s+}'(E_p'')$ and $E_{s-}'(E_p'')$ using (3.68) and (3.70). Inserting into (3.67) and (3.69) gives $E_s''(E_s)$ and $E_p''(E_s)$, i.e., $\tilde{r}_{ps}$ and $\tilde{r}_{ss}$, respectively, see also appendix (D). Assuming equivalent values for n_+' and n_-' the reflection coefficients are given by

$$\tilde{r}_{ps} = \frac{\tilde{\varepsilon}_{xy}\tilde{n}\cos\alpha}{\tilde{n}'(\tilde{n}\cos\tilde{\alpha}' + \tilde{n}'\cos\alpha)(\tilde{n}\cos\alpha + \tilde{n}'\cos\tilde{\alpha}')} \quad , \tag{3.71}$$

$$\tilde{r}_{ss} = \frac{\tilde{n}\cos\alpha - \tilde{n}'\cos\tilde{\alpha}'}{\tilde{n}\cos\alpha + \tilde{n}'\cos\tilde{\alpha}'} \quad . \tag{3.72}$$

3.3.2 Incident p-wave: $E_s = 0$

$$E_s'' = \sum_{\pm} E'_{s\pm} \quad , \tag{3.73}$$

$$\cos\alpha(E_p - E_p'') = \sum_{\pm} \left(-\frac{\varepsilon_{xy}\sin^2\alpha'_{\pm}}{2\varepsilon_{xx}\cos\alpha'_{\pm}} \mp i \right) \cos\alpha'_{\pm} E'_{s\pm} \quad , \tag{3.74}$$

$$-n\cos\alpha E_s'' = \sum_{\pm} n'_{\pm}\cos\alpha'_{\pm} E'_{s\pm} \quad , \tag{3.75}$$

$$n(E_p + E_p'') = \sum_{\pm} n'_{\pm} \left(\frac{\varepsilon_{xy}\sin^2\alpha'_{\pm}}{2\varepsilon_{xx}\cos\alpha'_{\pm}} \mp i \right) E'_{s\pm} \quad . \tag{3.76}$$

In analogy to an incident s-wave, $E'_{s+}(E_s'')$ and $E'_{s-}(E_s'')$ are calculated from (3.73) and (3.75), then by inserting $E'_{s\pm}(E_s'')$ into (3.74) and (3.76) $E_p''(E_p)$ and $E_s''(E_p)$, i.e., $\tilde{r}_{pp}$ and $\tilde{r}_{sp}$, respectively, are obtained. Assuming $n'_+ \approx n'_- \approx n'$ and $\alpha'_+ \approx \alpha'_- \approx \alpha'$ for the nominator of E'_{s+} and E'_{s-}, the refracted components yield[e.]

$$\tilde{r}_{pp} = \frac{E_p''}{E_p} = \frac{n'\cos\alpha - n\cos\alpha'}{n'\cos\alpha + n\cos\alpha'} \quad , \tag{3.78}$$

$$\tilde{r}_{sp} = \frac{E_s''}{E_p} = \frac{n\varepsilon_{xy}\cos\alpha}{n'(n\cos\alpha' + n'\cos\alpha)(n\cos\alpha + n'\cos\alpha')} \quad . \tag{3.79}$$

3.3.3 Polar magneto-optical Kerr effect (P-MOKE) in the Two-Media Approach

Two-media approach means that the Kerr angles are calculated for the boundary between two homogeneous media. The complex Kerr angle $\Theta_K = \theta_K + i\varepsilon_K$ of an incident s-wave is given by $\tan\Theta_K^s = \frac{\tilde{r}_{ps}}{\tilde{r}_{ss}}$ and that of an incident p-wave by $\tan\Theta_K^p = \frac{\tilde{r}_{sp}}{\tilde{r}_{pp}}$ if the approximations of You and Shin [36, 37, 38] apply (see also the appendix B). The compact form of the Kerr angles in the two-media approach (for details see the appendix C), assuming identical diagonal matrix elements and for the off-diagonal matrix elements $\varepsilon_{xy} = -\varepsilon_{yx}$ is then

$$\tan\Theta_K^p = \frac{\tilde{r}_{sp}}{\tilde{r}_{pp}} = \frac{\cos\alpha}{\cos(\alpha+\alpha')}\frac{n\varepsilon_{xy}}{n'(n'^2 - n^2)} \quad , \tag{3.80}$$

$$\tan\Theta_K^s = \frac{\tilde{r}_{ps}}{\tilde{r}_{ss}} = \frac{\cos\alpha}{\cos(\alpha-\alpha')}\frac{n\varepsilon_{xy}}{n'(n^2 - n'^2)} \quad . \tag{3.81}$$

[e.]

$$E'_{s+} \approx -E'_{s-} \approx i\frac{n'}{\varepsilon_{xy}}(n'\cos\alpha' + n\cos\alpha)E_s'' \tag{3.77}$$

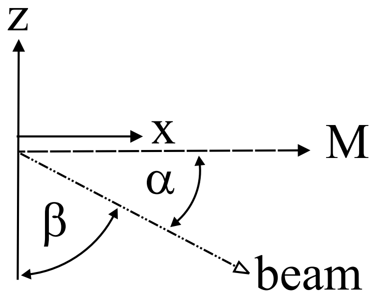

Figure 3.3: Geometry. The angle occurring in the electric field is the angle α between the magnetic field and the propagation direction of the beam. In the case of L-MOKE this angle is complementary to the angle between the surface normal and the propagation direction of the beam β, thus $\alpha + \beta = \pi/2$.

3.4 Longitudinal magneto-optical Kerr effect (L-MOKE) in the Two-Media Approach

In longitudinal geometry the magnetization is in the surface plane and in the plane of incidence. The angle $\alpha'_\pm$ (equations (3.53) and (3.53)) between the propagation direction of the beam and the magnetization is complementary to the angle between surface normal and the propagation direction of the beam $\beta'_\pm$, however, $\alpha'_\pm + \beta'_\pm = \pi/2$, see Fig. 3.3. Therefore the relations (3.53) and (3.54) read

$$E'_{a\pm} \approx \left(\frac{\varepsilon_{xy}\sin^2(\pi/2-\beta'_\pm)}{2\varepsilon_{xx}\cos(\pi/2-\beta'_\pm)} \mp i\right) E'_{b\pm} = \left(\frac{\varepsilon_{xy}\cos^2\beta'_\pm}{2\varepsilon_{xx}\sin\beta'_\pm} \mp i\right) E'_{b\pm} \quad , \tag{3.82}$$

$$E'_{c\pm} \approx -\frac{\varepsilon_{xy}\sin(\pi/2-\beta'_\pm)}{\varepsilon_{xx}} E'_{b\pm} = -\frac{\varepsilon_{xy}\cos\beta'_\pm}{\varepsilon_{xx}} E'_{b\pm} \quad . \tag{3.83}$$

The boundary conditions corresponding to the equations (3.63) and (3.66) yield,

$$\cos\beta(E_p - E''_p) = \sum_\pm \left(\frac{\varepsilon_{xy}(1+\sin^2\beta'_\pm)}{2\varepsilon_{xx}\sin\beta'_\pm} \mp i\right) E'_{s\pm}\cos\beta'_\pm \quad , \tag{3.84}$$

$$n(E_p + E''_p) = \sum_\pm \left(\frac{\varepsilon_{xy}\cos^2\beta'_\pm}{2\varepsilon_{xx}\sin\beta'_\pm} \mp i\right) n'_\pm E'_{s\pm} \quad . \tag{3.85}$$

The boundary conditions (3.64) and (3.65) for P-MOKE are identical for L-MOKE. Applying the same approximations as for P-MOKE the Fresnel-coefficients for L-MOKE are given by,

$$\tilde{r}_{ss} = \frac{n\cos\beta - n'\cos\beta'}{n\cos\beta + n'\cos\beta'} \quad , \tag{3.86}$$

$$\tilde{r}_{pp} = \frac{n'\cos\beta - n\cos\beta'}{n'\cos\beta + n\cos\beta'} \quad , \tag{3.87}$$

$$-\tilde{r}_{sp} = \tilde{r}_{ps} = \frac{n\varepsilon_{xy}\cos\beta}{n'(n\cos\beta' + n'\cos\beta)(n\cos\beta + n'\cos\beta')}\tan\beta' \quad . \tag{3.88}$$

Thus for an incident p-wave the Kerr rotation angle is,

$$\tan\Theta_K^p = \frac{\tilde{r}_{sp}}{\tilde{r}_{pp}} = \frac{n\varepsilon_{xy}\cos\beta\tan\beta'}{n'(n\cos\beta + n'\cos\beta')(n'\cos\beta - n\cos\beta')} \quad , \tag{3.89}$$

$$= \frac{\cos\beta\tan\beta'}{\cos(\beta+\beta')}\frac{n\varepsilon_{xy}}{n'(n'^2-n^2)} \quad , \tag{3.90}$$

and for an incident s-wave,

$$\tan\Theta_K^s = \frac{\tilde{r}_{ps}}{\tilde{r}_{ss}} = -\frac{n\varepsilon_{xy}\cos\beta\tan\beta'}{n'(n\cos\beta' + n'\cos\beta)(n\cos\beta - n'\cos\beta')} \quad , \tag{3.91}$$

$$= -\frac{\cos\beta\tan\beta'}{\cos(\beta-\beta')}\frac{n\varepsilon_{xy}}{n'(n^2-n'^2)} \quad . \tag{3.92}$$

3.5 Properties of two-media formulas

The system we discuss is the interface between the vacuum ($n = 1$) and a uniform magnetic medium (n'). In the Figs. 3.4 and 3.5 it is shown how the two-media formula depends on the refractive index n' and on the off-diagonal part of the dielectric tensor ε_{xy}. The real part of the complex refractive Kerr angle is the Kerr rotation angle θ_K and the imaginary part is the Kerr ellipticity angle ε_K.

For an incident p-wave and a real refractive index the complex refractive Kerr angle Θ_K would have a pole if $\cos(\beta+\beta') = 0$, i.e., $\beta+\beta' = \pi/2$. If the refractive index n' of the medium is close to 1, then this pole occurs near $\pi/2$, as the β and β' are approximately the same.

But for a complex refractive index the nominator becomes complex and the pole transforms to a local maximum of finite height. This peak is shifted in β by varying the constants n and $Q = i\varepsilon_{xy}/\varepsilon_{xx}$. As it can be seen in the plots for the polar Kerr effect, the variation of n changes the height of the maximum whereas the variation of Q dramatically influences the angle β where the peak occurs.

There exist measurements documenting the dependence on the angle of incidence [39] later used to confirm the applicability of the two-media formula. [36] The agreement between the experiment and the phenomenological theory following from the Maxwell equations, only, was almost perfect.

In Chapter 4 the 2×2-matrix technique will be developed which is an algorithm allowing one to take into account multiple reflections and interferences. The up to now calculated approximate formulas serve as a first estimation to the exactly calculated *ab-initio* results.

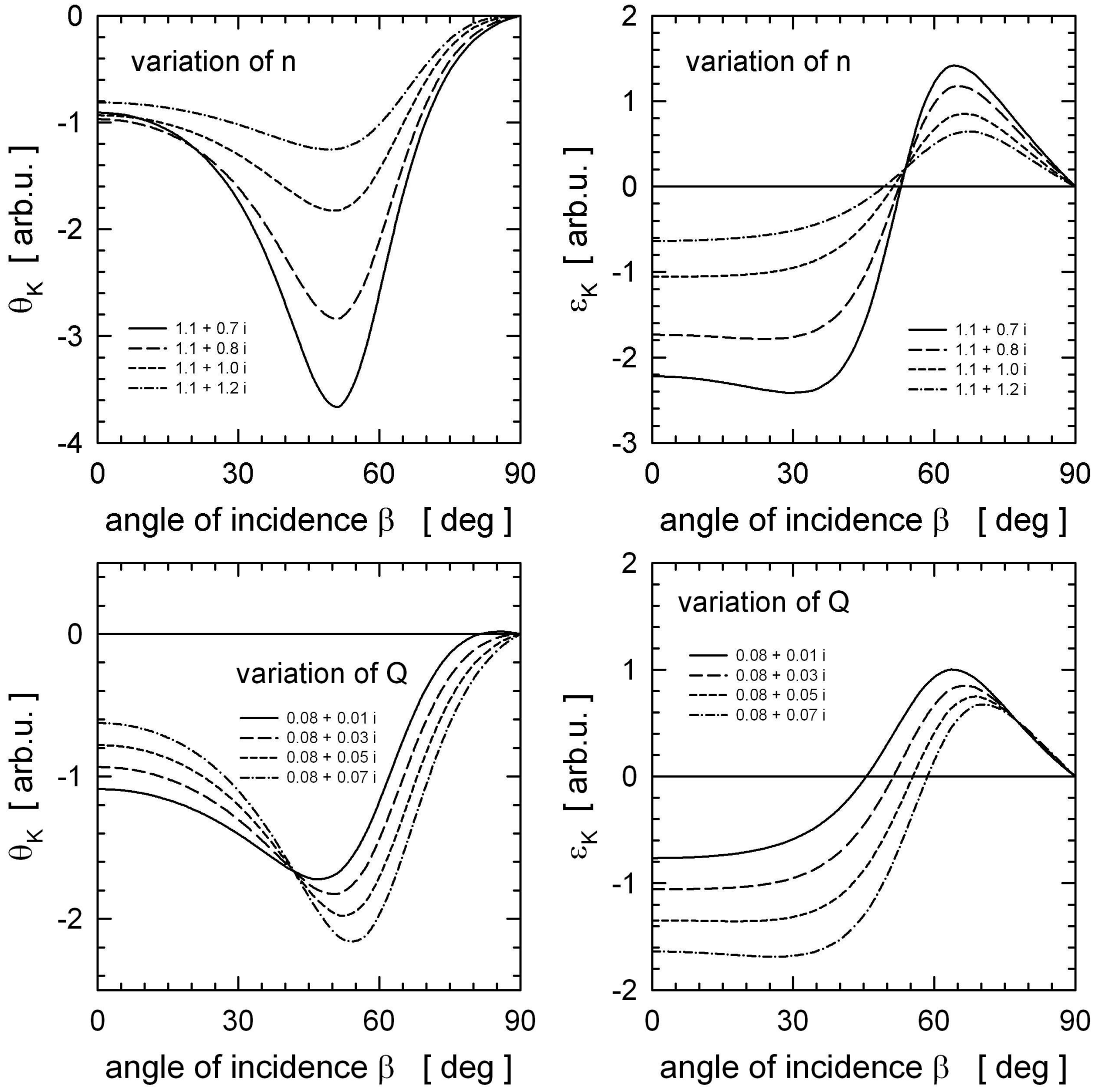

Figure 3.4: Polar MOKE using the two-media approach. In the upper row the magneto-optical Voigt parameter Q, defined by $\mathrm{i}\frac{\varepsilon_{xy}}{\varepsilon_{xx}}$, is fixed at $0.08 + 0.03\mathrm{i}$ while the refractive index n is varying according to the values given in the respective plots. In the lower row the refractive index n is set to 1.1+i while the Voigt parameter Q is varying.

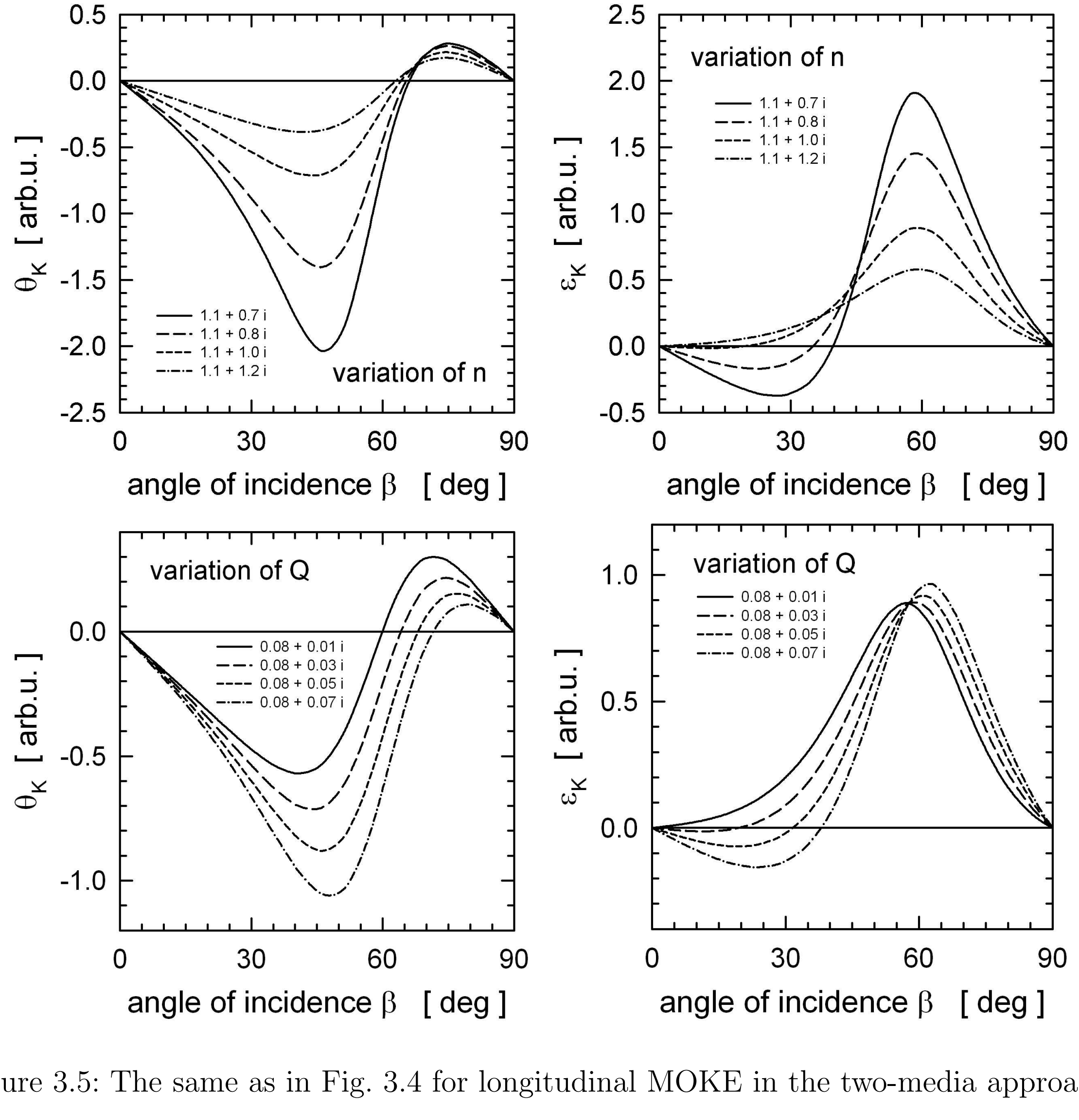

Figure 3.5: The same as in Fig. 3.4 for longitudinal MOKE in the two-media approach.

4 Multiple reflections and interferences: The 2×2 matrix technique for arbitrary magnetization

4.1 Optical properties of a layered system

The optical properties of a material can be described by the Helmholtz-Fresnel equation (3.18). This approach does include the option of choosing an arbitrary direction of an eventual magnetization and deals with all reflections and interferences of a system caused by incident light. In thin film systems the dielectric tensor depends on the photon frequency ω and varies with the distance from the surface. Since we are interested in interactions of visible and ultra-violet light with the surface, the atomic variations of the dielectric tensor cannot be resolved. Therefore it is assumed that the spatial variation of the dielectric tensor is negligible in one layer. Then the Helmholtz-Fresnel equation can be reformulated in layer-resolved quantities.

In the following first the solutions (Section 4.1.1) of the Helmholtz-Fresnel equation are discussed in a single layer and then boundary conditions (Section 4.1.2) are introduced in order to join up the layer-resolved quantities.

4.1.1 Solution in one layer

Consider a solid medium magnetized homogeneously in an arbitrary direction. The surface normal is parallel to the xy-plane, then the layer-resolved permittivity tensor ε^p is of the form,

$$\varepsilon^p = \begin{pmatrix} \varepsilon^p_{xx} & \varepsilon^p_{xy} & \varepsilon^p_{xz} \\ \varepsilon^p_{yx} & \varepsilon^p_{yy} & \varepsilon^p_{yz} \\ \varepsilon^p_{zx} & \varepsilon^p_{zy} & \varepsilon^p_{zz} \end{pmatrix} \quad .$$

The Fresnel equation should be solved for a coordinate system where the arbitrary assumed (not parallel to the surface normal) wave vector, $\mathbf{k}_p$, takes on the form

$$\mathbf{k}_p = n_p \boldsymbol{\kappa}_p \quad ,$$

where n_p is the complex refractive index and $\boldsymbol{\kappa}_p$ the unit vector in the propagation direction of the beam. n_p follows from the below Fresnel equation,

$$\det\left[n_p^2 \delta_{\mu\nu} - \varepsilon^p_{\mu\nu} - n_p^2 \kappa_{p,\mu} \kappa_{p,\nu}\right] = 0 \quad , \quad \mu, \nu \in \{x, y, z\} \quad ,$$

where $\varepsilon^p_{\mu\nu}$ is given in the rotated coordinate system. The notation of the previous chapter has to be generalized when dealing with multi-layer systems. To distinguish into incident, reflected and reflected waves is not appropriate any more because at an interface waves impinge from both sides and get reflected and refracted in either side again. Therefore we will only give numbers to the four solutions. Since in this equation only even powers of n_p occur the corresponding solutions $\left\{ n_p^{(k)} \right\}, k = 1, \ldots, 4$, have the property that

$$n_p^{(1)} = -n_p^{(3)} \quad , \quad n_p^{(2)} = -n_p^{(4)} \quad ,$$

which in turn implies that these four solutions yield only two different systems of equations and therefore only two linear independent solutions can be obtained for the time independent part of the electric field vector $\mathbf{E}_p^{(k)}$.

The components of each wave can be expressed in terms of one component, for example,

$$\mathbf{E}_p^{(k)} = \begin{pmatrix} E_{p,x}^{(k)} \\ E_{p,y}^{(k)}(E_{p,x}^{(k)}) \\ E_{p,z}^{(k)}(E_{p,x}^{(k)}) \end{pmatrix} \quad , \quad k = 1 - 4 \quad ,$$

where $\mathbf{E}_p^{(k)}$ is given in coordinates where the surface normal coincides with the z-axis.

For a description of multiple reflections of light it is sufficient to take only the x- and the y-components into account because the three components of $\mathbf{E}_p$ are not independent. The monochromatic, homogeneous and harmonic plane waves are then given by

$$\mathbf{E}_p^{(k)}(z,t) = \mathbf{E}_p^{(k)} \exp\left[i(\tilde{q}z - \tilde{\omega}t)\right] \quad , \quad \tilde{q}_p = q_0 n_p^{(k)} \quad , \quad \tilde{\omega} = \omega - i\delta \quad , \tag{4.1}$$

where q_0,

$$q_0 = \frac{\omega}{c} \quad ,$$

is the propagation constant in vacuum, ω the photon frequency and δ the life-time broadening parameter [44, 45]. For later purposes it is necessary to identify the incident and the reflected waves at each interface. It is convenient to define waves with $n_p^{(1)}$ and $n_p^{(2)}$ ($\mathrm{Im}(n_p^{(k)}) < 0$, $k = 1, 2$) as incident waves and waves with $n_p^{(3)}$ and $n_p^{(4)}$ ($\mathrm{Im}(n_p^{(k)}) > 0$, $k = 3, 4$) as reflected waves.

The total incident wave (indicated by the superscript inc) is a linear combination of $\mathbf{E}_p^{(1)}$ and $\mathbf{E}_p^{(2)}$, which by introducing a 2×2 matrix can be written as a function of the x-component of $\mathbf{E}_p^{(1)}$ and the y-component of $\mathbf{E}_p^{(2)}$:

$$\begin{pmatrix} E_{p,x}^{\mathrm{inc}} \\ E_{p,y}^{\mathrm{inc}} \end{pmatrix} = \mathbf{A}_p \begin{pmatrix} E_{p,x}^{(1)} \\ E_{p,y}^{(2)} \end{pmatrix} \quad , \tag{4.2}$$

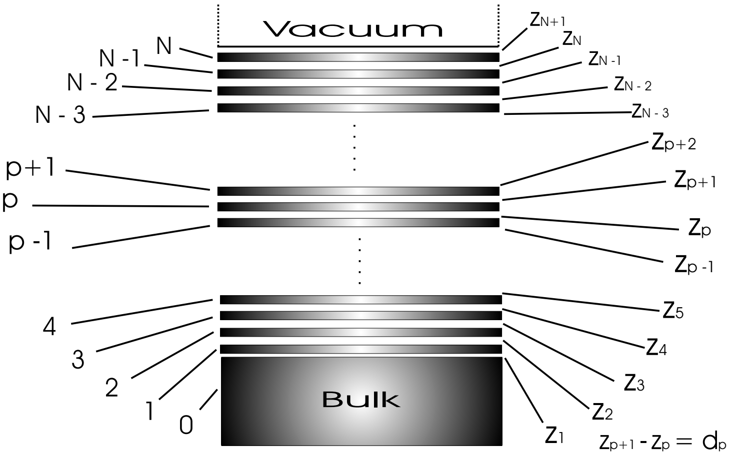

Figure 4.1: Layers are numbered from 1 to N, for the bulk regime the index 0 applies. Each layer p has a lower boundary z_p and an upper boundary z_{p+1}.

where

$$\mathbf{A}_p = \begin{pmatrix} 1 & \frac{E^{(2)}_{p,x}(E^{(2)}_{p,y})}{E^{(2)}_{p,y}} \\ \frac{E^{(1)}_{p,y}(E^{(1)}_{p,x})}{E^{(1)}_{p,x}} & 1 \end{pmatrix} \quad .$$

It is easy to find the matrix $\mathbf{A}'_p$ which connects the reflected wave to $\mathbf{E}^{(3)}_p$ and $\mathbf{E}^{(4)}_p$. The waves $\mathbf{E}^{(1)}_p$ and $\mathbf{E}^{(3)}_p$ differ only by a phase factor such that

$$\frac{E^{(3)}_{p,x}}{E^{(3)}_{p,y}} = \frac{E^{(1)}_{p,x}}{E^{(1)}_{p,y}} \quad , \quad \frac{E^{(4)}_{p,x}}{E^{(4)}_{p,y}} = \frac{E^{(2)}_{p,x}}{E^{(2)}_{p,y}} \quad ,$$

which in turn implies that $\mathbf{A}'_p \equiv \mathbf{A}_p$.

Defining now a general 2×2 reflection matrix $\mathbf{R}_p$ which transforms the x- and the y-components of the incident waves, $\mathbf{E}^{(1)}$ and $\mathbf{E}^{(2)}$, into their reflected counterparts (indicated by the superscript ref), $\mathbf{E}^{(3)}$ and $\mathbf{E}^{(4)}$, the total reflected wave is given by

$$\begin{pmatrix} E^{\text{ref}}_{p,x} \\ E^{\text{ref}}_{p,y} \end{pmatrix} = \mathbf{A}_p \mathbf{R}_p \begin{pmatrix} E^{(1)}_{p,x} \\ E^{(2)}_{p,y} \end{pmatrix} \quad . \tag{4.3}$$

For each solution $\mathbf{n}^{(k)}_p$ (the superscript (k) numbers the solutions) the magnetic field vectors $\mathbf{H}^{(k)}_p$ are given by

$$\mathbf{H}^{(k)}_p = \mathbf{n}^{(k)}_p \times \mathbf{E}^{(k)}_p \quad , \quad k = 1, \ldots 4 \quad .$$

In the above developed 2×2 matrix formalism the magnetic field vectors become

$$\begin{pmatrix} H^{\text{inc}}_{p,x} \\ H^{\text{inc}}_{p,y} \end{pmatrix} = \mathbf{N}_p \begin{pmatrix} E^{(1)}_{p,x} \\ E^{(2)}_{p,y} \end{pmatrix} \quad \text{and} \quad \begin{pmatrix} H^{\text{ref}}_{p,x} \\ H^{\text{ref}}_{p,y} \end{pmatrix} = -\mathbf{N}_p \mathbf{R}_p \begin{pmatrix} E^{(1)}_{p,x} \\ E^{(2)}_{p,y} \end{pmatrix} , \tag{4.4}$$

with the matrix $\mathbf{N}_p$,

$$\mathbf{N}_p = \begin{pmatrix} -n_p^{(1)} \frac{E_{p,y}^{(1)}(E_{p,x}^{(1)})}{E_{p,x}^{(1)}} & -n_p^{(2)} \\ n_p^{(1)} & n_p^{(2)} \frac{E_{p,x}^{(2)}(E_{p,y}^{(2)})}{E_{p,y}^{(2)}} \end{pmatrix} . \tag{4.5}$$

4.1.2 Boundary conditions

Between different layers the electric and the magnetic field have to be matched at each boundary z_p, see Fig. 4.1. The wave with the subscript z_p^+ is supposed to be the solution in the p-th layer at the lower boundary z_p^+; the wave with the subscript z_p^- is the solution in the $(p-1)$-th layer at the upper boundary z_p^-.

At z_p^+ the sum of the incident and the reflected wave applies, see equations (4.2) - (4.5),

$$(\mathbf{E}_p)_{z_p^+} \equiv \begin{pmatrix} E_{p,x} \\ E_{p,y} \end{pmatrix}_{z_p^+} = \mathbf{A}_p \left[\mathbf{1} + \mathbf{R}_p \right] \begin{pmatrix} E_{p,x}^{(1)} \\ E_{p,y}^{(2)} \end{pmatrix} \quad , \tag{4.6}$$

$$(\mathbf{H}_p)_{z_p^+} \equiv \begin{pmatrix} H_{p,x} \\ H_{p,y} \end{pmatrix}_{z_p^+} = \mathbf{N}_p \left[\mathbf{1} - \mathbf{R}_p \right] \begin{pmatrix} E_{p,x}^{(1)} \\ E_{p,y}^{(2)} \end{pmatrix} \quad , \tag{4.7}$$

where $\mathbf{1}$ is the unit matrix.

Due to the finite thickness d_p of layer $p-1$ the total wave at the lower boundary z_p^- is augmented by a phase shift φ_{p-1}^k with respect to z_{p-1}^+,

$$\varphi_{p-1}^{(k)} = n_p^{(k)} q_0 d_{p-1} \quad .$$

For $k = 1$ or $k = 3$ the matrix $\mathbf{C}_{p-1}^{(k,k+1)}$,

$$\mathbf{C}_{p-1}^{(k,k+1)} = \begin{pmatrix} \exp\left(i\varphi_{p-1}^{(k)}\right) & 0 \\ 0 & \exp\left(i\varphi_{p-1}^{(k+1)}\right) \end{pmatrix} \quad , \tag{4.8}$$

describes wave propagation in layer $(p-1)$ from z_{p-1}^+ to z_p^-:

$$(\mathbf{E}_p)_{z_p^-} \equiv \begin{pmatrix} E_{p,x} \\ E_{p,y} \end{pmatrix}_{z_p^-} = \mathbf{A}_{p-1} \left[\mathbf{C}_{p-1}^{(1,2)} + \mathbf{C}_{p-1}^{(3,4)} \mathbf{R}_{p-1} \right] \begin{pmatrix} E_{p-1,x}^{(1)} \\ E_{p-1,y}^{(2)} \end{pmatrix} \quad , \tag{4.9}$$

$$(\mathbf{H}_p)_{z_p^-} \equiv \begin{pmatrix} H_{p,x} \\ H_{p,y} \end{pmatrix}_{z_p^-} = \mathbf{N}_{p-1} \left[\mathbf{C}_{p-1}^{(1,2)} - \mathbf{C}_{p-1}^{(3,4)} \mathbf{R}_{p-1} \right] \begin{pmatrix} E_{p-1,x}^{(1)} \\ E_{p-1,y}^{(2)} \end{pmatrix} \quad . \tag{4.10}$$

The boundary conditions, namely the continuity of the tangential components at z_p.

$$\begin{aligned} (\mathbf{E}_p)_{z_p^+} &= (\mathbf{E}_p)_{z_p^-} \quad , \\ (\mathbf{H}_p)_{z_p^+} &= (\mathbf{H}_p)_{z_p^-} \quad , \end{aligned}$$

lead to a set of equations for $\left(E^{(1)}_{p,x}, E^{(2)}_{p,y}\right)$ and $\left(E^{(1)}_{p-1,x}, E^{(2)}_{p-1,y}\right)$. After elimination of these vectors an explicit expression for $\mathbf{R}_p$ is obtained:

$$\mathbf{R}_p = \left[\mathbf{N}_p + \mathbf{D}_{p-1}\mathbf{A}_p\right]^{-1}\left[\mathbf{N}_p - \mathbf{D}_{p-1}\mathbf{A}_p\right] \quad , \tag{4.11}$$

where $\mathbf{D}_{p-1}$ is defined by

$$\mathbf{D}_{p-1} = \mathbf{N}_{p-1}\left[\mathbf{C}^{(1,2)}_{p-1} - \mathbf{C}^{(3,4)}_{p-1}\mathbf{R}_{p-1}\right]\left[\mathbf{C}^{(1,2)}_{p-1} + \mathbf{C}^{(3,4)}_{p-1}\mathbf{R}_{p-1}\right]^{-1}\mathbf{A}^{-1}_{p-1} \quad . \tag{4.12}$$

Equations (4.11) and (4.12) have to be solved recursively starting with $p = 1$, namely the boundary between the substrate and the first layer. For $p = N + 1$ the corresponding reflectivity matrix $\mathbf{R}_{\text{surf}}$ is the surface reflectivity matrix.

4.1.3 Recursive algorithm

4.1.3.1 Initial step:

The equations (4.11) and (4.12) are applied to the boundary between the substrate and first layer. $\mathbf{A}_0$, $\mathbf{N}_0$, $\mathbf{C}^{(1,2)}_0$, and $\mathbf{C}^{(3,4)}_0$ are determined using the refractive indices of the bulk system and the corresponding reflectivity matrix $\mathbf{R}_0$ can be assumed to be zero since in an ideal bulk system there are no boundaries and therefore no reflections, thus

$$\begin{aligned} \mathbf{D}_0 &= \mathbf{N}_0\mathbf{A}^{-1}_0 \quad , & (4.13)\\ \mathbf{R}_1 &= [\mathbf{N}_0\mathbf{A}^{-1}_0\mathbf{A}_1 + \mathbf{N}_1]^{-1}[\mathbf{N}_1 - \mathbf{N}_0\mathbf{A}^{-1}_0\mathbf{A}_1] \quad . & (4.14)\end{aligned}$$

4.1.3.2 Final step:

Taking into account that there are only two solutions in the vacuum, namely one incident and one reflected wave, the reflectivity matrix at the vacuum interface (usually termed surface reflectivity matrix) is given by

$$\mathbf{R}_{\text{surf}} = \begin{pmatrix} r_{xx} & r_{xy} \\ r_{yx} & r_{yy} \end{pmatrix} \quad .$$

Furthermore, the material properties in vacuum are obtained by setting $n^{(1)}_p$ and $n^{(2)}_p$ to unity, that is,

$$\mathbf{N}_{vac} = \begin{pmatrix} 0 & 1 \\ -1 & 0 \end{pmatrix} \quad .$$

At z^+_{N+1} the total fields are therefore given by

$$\begin{aligned} [\mathbf{E}_{vac}]_{z^+_{N+1}} &= [\mathbf{1} + \mathbf{R}_{\text{surf}}]\mathbf{E}^{(inc)}_{vac} \quad , \\ [\mathbf{H}_{vac}]_{z^+_{N+1}} &= \mathbf{N}_{vac}[\mathbf{1} - \mathbf{R}_{\text{surf}}]\mathbf{H}^{(inc)}_{vac} \quad , \end{aligned}$$

while at z^-_{N+1} they are of the form ($p = N$)

$$\begin{pmatrix} E_{vac,x} \\ E_{vac,y} \end{pmatrix}_{z^-_{N+1}} = \mathbf{A}_N \left[\mathbf{C}^{12}_N + \mathbf{C}^{34}_N R_N\right] \begin{pmatrix} E^{(1)}_{N,x} \\ E^{(2)}_{N,y} \end{pmatrix} \quad ,$$

$$\begin{pmatrix} H_{vac,x} \\ H_{vac,y} \end{pmatrix}_{z^-_{N+1}} = \mathbf{N}_N \left[\mathbf{C}^{12}_N - \mathbf{C}^{34}_N \mathbf{R}_N\right] \begin{pmatrix} E^{(1)}_{N,x} \\ E^{(2)}_{N,y} \end{pmatrix} \quad .$$

Demanding continuity at the surface for both fields leads to

$$\mathbf{R}_{\text{surf}} = \left[\mathbf{N}_{vac} + \mathbf{D}_N\right]^{-1} \left[\mathbf{N}_{vac} - \mathbf{D}_N\right] \quad , \tag{4.15}$$

$$\mathbf{D}_N = \mathbf{N}_N \left[\mathbf{C}^{(1,2)}_N - \mathbf{C}^{(3,4)}_N R_N\right] \left[\mathbf{C}^{(1,2)}_N + \mathbf{C}^{(3,4)}_N \mathbf{R}_N\right]^{-1} \mathbf{A}^{-1}_N \quad , \tag{4.16}$$

Equations (4.15) and (4.16) are the corresponding equations for the vacuum-surface interface which are needed to determine $\mathbf{R}_{\text{surf}}$.

4.2 Determination of the dielectric tensor ε^p

4.2.1 Recursion

It was shown by Vernes et al. [44] that the (macroscopic) permittivity tensor ε^{pq} can be related to the (microscopic) conductivity tensor σ^{pq} in terms of the following mapping,

$$\varepsilon^{pq}_{ij}(\omega) = \delta^{pq}_{ij} + \frac{4\pi i}{\omega} \sigma^{pq}_{ij}(\omega) \quad , \quad p, q = 1, ...N \quad , \quad \delta^{pq}_{ij} = \delta_{ij}\delta^{pq}$$

where N is the total number of (atomic) layers and $i, j \in \{x, y, z\}$. In order to obtain a layer-resolved **reduced** permittivity ε^p, the following implicit equation has to be solved:

$$\varepsilon^p(\omega)\,\mathbf{E}_p = \sum_{q=1}^{N} \varepsilon^{pq}(\omega)\,\mathbf{E}_q \quad , \quad p = 1, ..., N. \tag{4.17}$$

Shifting the index p in Equation (4.9) to $p + 1$,

$$\begin{pmatrix} E_{p+1,x} \\ E_{p+1,y} \end{pmatrix}_{z^-_{p+1}} = \mathbf{A}_p \left[\mathbf{C}^{(1,2)}_p + \mathbf{C}^{(3,4)}_p \mathbf{R}_p\right] \begin{pmatrix} E^{(1)}_{p,x} \\ E^{(2)}_{p,y} \end{pmatrix} \tag{4.18}$$

the pseudo-vector $\left(E^{(1)}_{p,x}, E^{(2)}_{p,y}\right)^T$, where T stands for transposed, can be expressed in terms of equation (4.18) and inserted in equation (4.6) yields

$$\begin{pmatrix} E_{p,x} \\ E_{p,y} \end{pmatrix}_{z^+_p} = \mathbf{A}_p \left[\mathbf{1} + \mathbf{R}_p\right] \left[\mathbf{C}^{(1,2)}_p + \mathbf{C}^{(3,4)}_p \mathbf{R}_p\right]^{-1} \mathbf{A}^{-1}_p \begin{pmatrix} E_{p+1,x} \\ E_{p+1,y} \end{pmatrix}_{z^-_{p+1}} \quad . \tag{4.19}$$

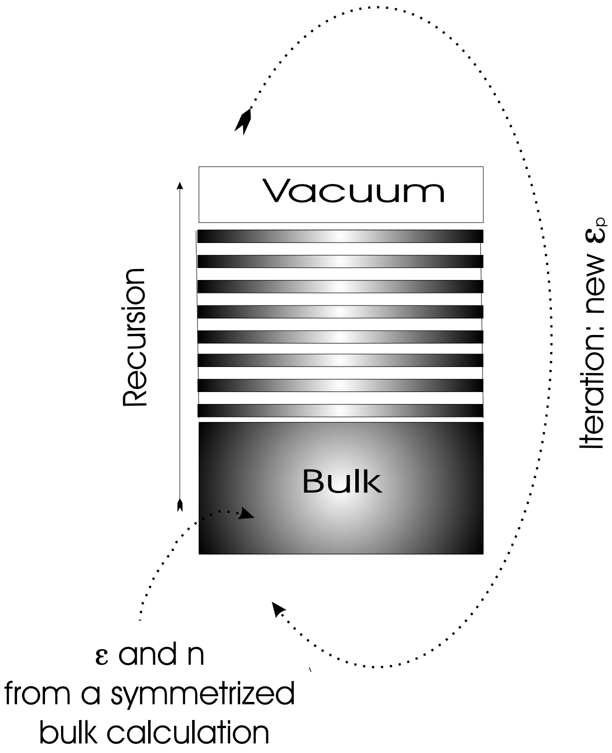

Figure 4.2: Recursive algorithm: (1) The bulk properties $\varepsilon(\omega)$ and $\mathbf{n}(\omega)$ serving as the starting values for a layer recursion have to be known from a separate bulk calculation. (2) The 2×2-matrix technique starts at the boundary between the bulk and the first layer considered. Subsequently all reflections, transmissions and interferences at all boundaries between different layers are taken into account. (3) The obtained layer-resolved permittivities $\varepsilon^p(\omega)$ serve as input for the next iteration: thus the recursion is repeated until the resolved permittivities $\varepsilon^p(\omega)$ no longer change.

$(\mathbf{E}_p)_{z_p^+}$ describes a wave at the boundary between layer $(p-1)$ and layer p. At half distance between z_p and z_{p+1} this wave accumulates a phase shift which can be taken into account using a factor $\sqrt{\mathbf{C}_p^{(k,k+1)}}$, $k = 1, 3$, such that each partial wave is multiplied automatically with the correct phase factor,

$$\left(\begin{array}{c} E_{p,x} \\ E_{p,y} \end{array} \right)_{z_p^+ + \frac{d_p}{2}} = \mathbf{A}_p \left[\sqrt{\mathbf{C}_p^{(1,2)}} + \sqrt{\mathbf{C}_p^{(3,4)}} \mathbf{R}_p \right] \left(\begin{array}{c} E_{p,x}^{(1)} \\ E_{p,y}^{(2)} \end{array} \right) \quad . \tag{4.20}$$

By replacing $\left(E_{p,x}^{(1)}, E_{p,y}^{(2)} \right)^T$ in equation (4.20) with equation (4.18) and recursively inserting equation (4.19) into equation (4.20). $(\mathbf{E}_p)_{z_p^+ + \frac{d_p}{2}}$ can finally be written as a function of $(\mathbf{E}_N)_{z_N^-}$:

$$\left(\begin{array}{c} E_{p,x} \\ E_{p,y} \end{array} \right)_{z_p^+} = \prod_{k=p}^{N} \overline{\mathbf{W}}_k \left(\begin{array}{c} E_{N,x} \\ E_{N,y} \end{array} \right)_{z_N^-} = \prod_{k=0}^{N-p} \overline{\mathbf{W}}_{k+p} \left(\begin{array}{c} E_{N,x} \\ E_{N,y} \end{array} \right)_{z_N^-} \quad , \tag{4.21}$$

where the matrices $\overline{\mathbf{W}}_{k+p}$ are defined in the following way

$$\overline{\mathbf{W}}_{p+k} = \mathbf{A}_p \left[\sqrt{\mathbf{C}_p^{(1,2)}} + \sqrt{\mathbf{C}_p^{(3,4)}} \mathbf{R}_p \right] \left[\mathbf{C}_p^{(1,2)} + \mathbf{C}_p^{(3,4)} \mathbf{R}_p \right]^{-1} \mathbf{A}_p^{-1} \quad , \quad k = 0 \quad ,$$

$$\overline{\mathbf{W}}_{p+k} = \mathbf{A}_{p+k} \left[\mathbf{1} + \mathbf{R}_{p+k} \right] \left[\mathbf{C}_{p+k}^{(1,2)} + \mathbf{C}_{p+k}^{(3,4)} \mathbf{R}_{p+k} \right]^{-1} \mathbf{A}_{p+k}^{-1} \quad , \quad k > 0 \quad .$$

The permittivity ε^p is obtained by inserting the expansion in equation (4.21) into equation (4.17):

$$\begin{aligned} \varepsilon^p(\omega) &= \sum_{q=1}^{N} \varepsilon^{pq}(\omega) \mathbf{W}_{pq} \quad , \\ \mathbf{W}_{pq} &= \left(\prod_{k=0}^{N-q} \overline{\mathbf{W}}_{k+q} \right) \left(\prod_{k=0}^{N-p} \overline{\mathbf{W}}_{k+p} \right)^{-1} \quad . \end{aligned} \tag{4.22}$$

This system of equations for $\varepsilon^p(\omega)$ (see equation (4.17)) has to be solved iteratively (Fig. 4.2), starting with

$$\overline{\mathbf{W}}_k^{(0)} = \mathbf{1} \quad , \tag{4.23}$$

implying that

$$\left[\varepsilon^p(\omega) \right]^0 = \sum_{q=1}^{N} \varepsilon^{pq}(\omega) \quad .$$

As a criterion for the accuracy for this iterative procedure the below inequality can be used

$$\left\| \varepsilon^p(\omega)^{(n)} - \varepsilon^p(\omega)^{(n+1)} \right\| < \varepsilon^p(\omega)^{threshold} . \tag{4.24}$$

An analysis of the matrices $\mathbf{W}_{pq}$ shows that a number of factors $\overline{\mathbf{W}}_{p+k}$ cancel in the product.

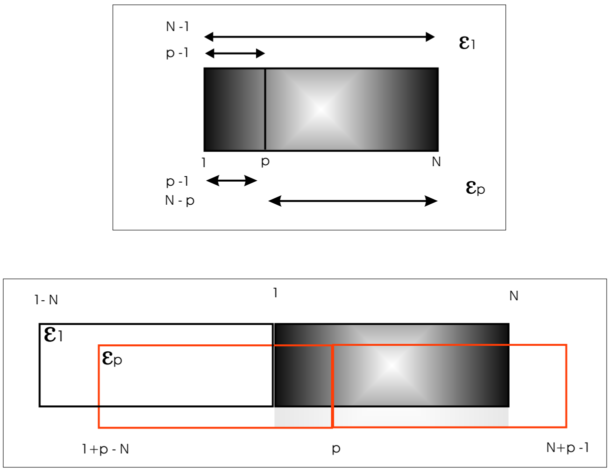

Figure 4.3: *Top:* The picture shows the original layered system: The problem in this setup is that $\varepsilon_p = \sum_{q\in[1,N]} W_{pq}\varepsilon^{pq}$ is asymmetric with respect to a shift in p. ε^{pq} with a smaller difference between p and q give larger contributions. For example in the case of ε_1 the largest $|p-q|$ is $N-1$ whereas in the case of any ε_p with $1 < p < N$ the largest difference is $p-1$ or $N-p$. Therefore, the contributions to the sum over q change depending on the value of p. *Bottom:* The picture shows the extended layered system which is the symmetric extension of the original layered system. The extended sum has the same number of layers on the left and right hand side of p , independent of a change in p.

4.2.2 Bulk systems

As described above the recursive algorithm starts at the interface between the substrate and first layer and ends at the interface between the last layer and the vacuum. In order to obtain the necessary bulk quantities $\mathbf{A}_0$ and $\mathbf{N}_0$ as starting values the bulk properties, ε_{bulk} and $\mathbf{n}_{bulk}$, have to be investigated. Per definition in a bulk system (infinite system, three-dimensional periodicity) all physical properties have to be the same in all unit cells. For a simple lattice (one atom per unit cell) this implies that all physical quantities have to be the same in all (atomic) layers. In the above algorithm the total number N of atomic layers necessarily has to be finite. In the case of a bulk (i.e. an infinite) system this involves problems, see Fig. 4.3, thus, a kind of symmetric extension of the layered system is introduced according to Vernes *et al.* [45].

The ε^p_{ij}, $i, j \in \{x, y, z\}$, calculated in this symmetric way are then given as the original sum plus the extensions to the left and to the right,

$$\varepsilon_{ij}^{p} = \sum_{q=p-N+1}^{0} \mathbf{W}^{N,N-|p-q|}\ \varepsilon_{ij}^{N,N-|p-q|} + \\ + \sum_{q=1}^{N} \mathbf{W}^{p,q}\ \varepsilon_{ij}^{p,q} + \sum_{q=N}^{p+N-1} \mathbf{W}^{1,1+|p-q|}\ \varepsilon_{ij}^{1,1+|p-q|} \quad . \tag{4.25}$$

4.2.3 Final remark

An important part of my work was to program the 2 × 2 matrix technique for arbitrary magnetic field and normal incidence.

Part II

Microscopic treatment: quantum mechanics

5 Korringa-Kohn-Rostoker method

5.1 The band-structure of a solid

A solid consists of neutrons, protons and electrons. In the Born-Oppenheimer approximation the nuclei are treated as frozen because of their huge mass compared to the electron's mass. An approach to treat the residual electron problem is the Hartree-Fock approximation where the many-particle Schrödinger-equation is approximated by an one-particle Schrödinger-equation with an effective potential which is solved self-consistently; the N-electron wave function is given by a Slater determinant. Although the exchange part is given exactly, the correlation part is missing. In order to account for correlation effects, the rather time-consuming configuration interaction (CI) calculations were introduced which involve a variational procedure on the wave function.

In density functional theory (DFT) the variational variable is the electron density $n(r)$. Hohenberg and Kohn [16] showed that the total energy is a unique functional of the density which is minimized in the ground state density. Kohn and Sham [15] showed that by applying the variational procedure the many-body Schrödinger-equation can be formulated for non-interacting particles.

By means of DFT there exist many methods to calculate the band-structure of a solid. We use the screened Korringa-Kohn-Rostoker (SKKR) Greens function method because it is convenient when dealing with surfaces and interfaces. Within the KKR method truly semi-infinite systems and not only slab geometries can be treated. Furthermore, layer-resolved quantities can be determined. In the present chapter we will present a straight description of the basic ideas of the SKKR-method.

5.2 Green's functions and observables

In the wave function formalism, the Kohn-Sham-equation for the generalized (continuous and bound) eigen-solutions, $|\phi_\alpha(\varepsilon)\rangle$, is given by [46]

$$\mathcal{H}|\phi_\alpha(\varepsilon)\rangle = \varepsilon|\phi_\alpha(\varepsilon)\rangle \quad . \tag{5.1}$$

The completeness of the basis set is expressed by the operator,

$$\mathcal{I} = \int d\varepsilon \sum_\alpha |\phi_\alpha(\varepsilon)\rangle\langle\phi_\alpha(\varepsilon)| \quad . \tag{5.2}$$

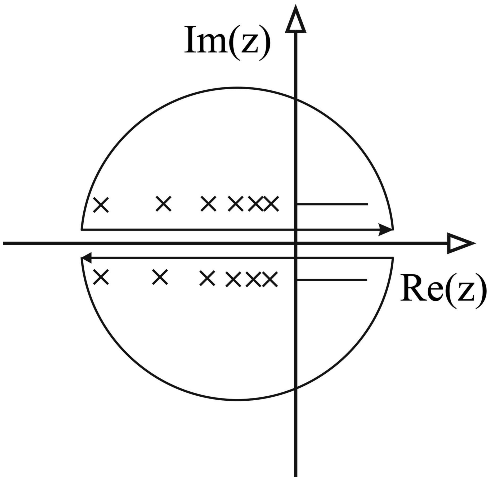

Figure 5.1: The poles and the branchcut are shifted by $\pm i\delta$ in the complex plane.

Equivalently to a wave-function formalism, the Kohn-Sham equation can be solved in the Green's function formalism where $\mathcal{G}(z)$ has to be determined from

$$(\mathcal{H} - \varepsilon)\mathcal{G}(z) = -\delta(z - \varepsilon) \quad . \tag{5.3}$$

Formally the solution for $\mathcal{G}(z)$ is given by

$$\mathcal{G}(z) = (\mathcal{H} - z\mathcal{I})^{-1} \quad , \quad z \in \mathbb{C} \quad , \quad \mathrm{Im}(z) \neq 0 \quad , \tag{5.4}$$

which in the basis of the eigenfunctions of $\mathcal{G}(z)$ yields

$$\mathcal{G}(z) = \int d\varepsilon' \sum_{\alpha} \frac{|\phi_\alpha(\varepsilon')\rangle\langle\phi_\alpha(\varepsilon')|}{z - \varepsilon'} \quad . \tag{5.5}$$

The restriction to $z \in \mathbb{C}$, $\mathrm{Im}(z) \neq 0$ implies that there are no poles (for discrete ε_n) and no branchcut (for continuous ε). The poles are shifted now from the real axis in the complex plane, $\varepsilon \pm i\delta$, see Figure 5.1. Depending on the path of the contour integration up and down side limits of the Greens function $\mathcal{G}(z)$ are defined,

$$\mathcal{G}^{\pm}(z) = \lim_{\delta \to 0+} \mathcal{G}(\varepsilon \pm i\delta) \quad . \tag{5.6}$$

Physics is interested in observables $\mathcal{A}$ the expectation value of which is calculated by the formula (see chapter 18 in Zabloudil et al. [41])

$$A = \mathrm{Tr}\,(f(\mathcal{H})\mathcal{A}) = \sum_{\alpha} f(\mathcal{H})\langle\phi_\alpha(\varepsilon)|\mathcal{A}|\phi_\alpha(\varepsilon)\rangle \quad , \tag{5.7}$$

where $f(\mathcal{H})$ is the Fermi-Dirac distribution function. By exploiting Cauchy's theorem this formula is transferred in the contour integral $\oint dz f(z)\mathrm{Tr}\,(\mathcal{A}\mathcal{G}^{\pm}(z))$ with the complex energy z. By deforming the contour to the real axis the observable becomes

$$A = \mp\frac{1}{\pi}\int\limits_{-\infty}^{\infty} d\varepsilon f(\varepsilon)\mathrm{Tr}\left(\mathcal{A}\mathcal{G}^{\pm}(\varepsilon)\right) \quad . \tag{5.8}$$

Therefore, the knowledge of the the Greens function $\mathcal{G}(\mathbf{r},\mathbf{r},E)$ allows to calculate more or less all quantities of interest. [47]

5.3 Perturbation theory

Perturbation theory can be developed in a wave function formalism or equivalently in a Green function formalism. If the Hamiltonian is given by

$$\mathcal{H} = \mathcal{H}_0 + \mathcal{V} \quad , \tag{5.9}$$

the wave-functions belonging to the unperturbed or the perturbed system, $|\phi_\alpha(\varepsilon)\rangle$ and $|\psi_\alpha(\varepsilon)\rangle$, are introduced in the following way,

$$\begin{aligned} (\varepsilon\mathcal{I} - \mathcal{H}_0)|\phi_\alpha(\varepsilon)\rangle &= 0 \quad , & (5.10)\\ (\varepsilon\mathcal{I} - \mathcal{H}_0 - \mathcal{V})|\psi_\alpha(\varepsilon)\rangle &= 0 \quad . & (5.11) \end{aligned}$$

In the Green function formalism we aim to write the Green's function of the perturbed system $\mathcal{G}$ in terms of the Green's function of the unperturbed system $\mathcal{G}_0$ (*Dyson equation*)

$$\begin{aligned} \mathcal{G}_0(z) &= (\mathcal{H}_0 - z\mathcal{I})^{-1} \quad , & (5.12)\\ \mathcal{G}(z) &= (z - \mathcal{H}_0 - \mathcal{V})^{-1} \\ &= \mathcal{G}_0(z)(1 + \mathcal{V}\mathcal{G}(z)) \\ &= \mathcal{G}_0 + \mathcal{G}_0\mathcal{V}\mathcal{G}_0 + \mathcal{G}_0\mathcal{V}\mathcal{G}_0\mathcal{V}\mathcal{G}_0 + \ldots \\ &= (\mathcal{I} - \mathcal{G}_0(z)\mathcal{V})^{-1}\mathcal{G}_0(z) = \mathcal{G}_0(z)(\mathcal{I} - \mathcal{V}\mathcal{G}_0(z))^{-1} \\ &= \mathcal{G}_0(z) + \mathcal{G}_0(z)\left[\mathcal{V} + \mathcal{V}\mathcal{G}_0(z)\mathcal{V} + \ldots\right]\mathcal{G}_0(z) \quad . & (5.13) \end{aligned}$$

Recursively, the solution $|\psi_\alpha(\varepsilon)\rangle$ of the perturbed Schrödinger equation is represented in terms of the unperturbed stated $|\phi_\alpha(\varepsilon)\rangle$ (*Lippmann-Schwinger equation*),

$$|\psi_\alpha(\varepsilon)\rangle = |\phi_\alpha(\varepsilon)\rangle + \mathcal{G}_0(\varepsilon)\mathcal{V}|\psi_\alpha(\varepsilon)\rangle \quad . \tag{5.14}$$

The transition matrix $\mathcal{T}$ connects the wave function $|\psi_\alpha(\varepsilon)\rangle$ with the unperturbed wave function $|\phi_\alpha(\varepsilon)\rangle$

$$\mathcal{V}|\psi_\alpha(\varepsilon)\rangle = \mathcal{T}|\phi_\alpha(\varepsilon)\rangle \quad . \tag{5.15}$$

The actual form of $\mathcal{T}$ is obtained by a multiplication of equation (5.14) with $\mathcal{V}$ from the left,

$$\begin{aligned}\mathcal{V}|\psi_\alpha(\varepsilon)\rangle &= \mathcal{V}|\phi_\alpha(\varepsilon)\rangle + \mathcal{V}\mathcal{G}_0\mathcal{V}|\psi_\alpha(\varepsilon)\rangle \quad , \\ \mathcal{T}|\phi_\alpha(\varepsilon)\rangle &= \mathcal{V}|\phi_\alpha(\varepsilon)\rangle + \mathcal{V}\mathcal{G}_0\mathcal{T}|\phi_\alpha(\varepsilon)\rangle \quad ,\end{aligned}$$

yielding

$$\begin{aligned}\mathcal{T}(z) &= \mathcal{V} + \mathcal{V}\mathcal{G}_0(z)\mathcal{T}(z) && (5.16)\\ &= \mathcal{V} + \mathcal{V}\mathcal{G}_0(z)\mathcal{V} + \dots \\ &= \mathcal{V}(1 + \mathcal{G}(z)\mathcal{V}) \quad . && (5.17)\end{aligned}$$

A comparison with equation (5.13) gives

$$\mathcal{G}(z) = \mathcal{G}_0(z) + \mathcal{G}_0(z)\mathcal{T}\mathcal{G}_0(z) \quad \Leftrightarrow \quad \mathcal{V}\mathcal{G}(z) = \mathcal{T}(z)\mathcal{G}_0(z) \quad . \tag{5.18}$$

5.4 Multiple Scattering Theory (MST)

5.4.1 Split the potential into individual scatterers

Using the methods of Multiple Scattering Theory (MST) the electronic band-structures of periodic solids are calculated. The scattering system is described as a collection of scattering potentials characterized by non-overlapping, spatially bounded potentials. Introducing the muffin-tin (MT) form of the potential implies that the scattering events at different sites are decoupled from each other. The Lippmann-Schwinger equation involves an incident wave scattered by a (local) potential giving rise to an outgoing solution being the superposition of the incoming and the outgoing scattered wave. Considering the MT-spheres as scattering centers for waves scattered from all other nuclei, a self-consistent problem is obtained. The total scattering matrix of the system will be formulated in terms of the scattering matrices of the individual centers.

5.4.2 Muffin tin potentials

The configurational space, Ω, is divided into disjunct domains, Ω_n, with $\Omega = \bigcup_{\{n\in\mathbb{N}\}}\Omega_n$ and $\Omega_m \cap \Omega_n = \{0\}$. Then the potential $\mathcal{V}$ is decomposed into components of single-domain potentials $\mathcal{V}_n$ localized at the centers of the atoms,

$$\mathcal{V}_n(\mathbf{r}) = \mathcal{V}(\mathbf{r})\ \theta(r^n_{\mathrm{mt}} - |\mathbf{R}_n - \mathbf{r}|) \quad , \tag{5.19}$$

where $\mathbf{R}_n$ points to the origin of the n-th MT-sphere and $r_{\mathrm{m}t}$ is the MT-radius of the n-th MT-sphere yielding the potential $\mathcal{V}$

$$\mathcal{V}(\mathbf{r}) = \sum_n \mathcal{V}_n(\mathbf{r}_n) \quad . \tag{5.20}$$

Instead of the transition matrix $\mathcal{T}$ for one potential $\mathcal{V}$ a single-site T-operator t^n is defined where $\mathcal{T}$ is replaced by t^n and $\mathcal{V}$ by $\mathcal{V}_n$,

$$t^n = \mathcal{V}_n + \mathcal{V}_n \mathcal{G}_0 t^n \quad . \tag{5.21}$$

$\mathcal{T}$ is expressed in terms of $\mathcal{V}_n$,

$$\mathcal{T} = \sum_n \mathcal{V}_n + \sum_{n,m} \mathcal{V}_n \mathcal{G}_0 \mathcal{V}_m + \sum_{n,m,l} \mathcal{V}_n \mathcal{G}_0 \mathcal{V}_m \mathcal{G}_0 \mathcal{V}_l + \ldots \quad , \tag{5.22}$$

or in terms of t^n,

$$\mathcal{T} = \sum_n t^n + \sum_{\{n,m|n\neq m\}} t^n \mathcal{G}_0 t^m + \sum_{\{n,m,l|n\neq m, m\neq l\}} t^n \mathcal{G}_0 t^m \mathcal{G}_0 t^l + \ldots \tag{5.23}$$

$$= \sum_n t^n + \sum_{n,m} t^n \mathcal{G}_0 (1-\delta_{nm}) t^m + \sum_{n,m,l} t^n \mathcal{G}_0 (1-\delta_{nm}) t^m \mathcal{G}_0 (1-\delta_{ml}) t^l + \ldots \quad . \tag{5.24}$$

The equations (5.22, 5.23) suggest that t^n can be regarded as a dressed potential. The definition of a *scattering path operator* (SPO) $\tau_{n,m}$ comprising all scatterings between the sites n and m is as follows

$$\mathcal{T} = \sum_{n,m} \tau_{nm} \quad , \tag{5.25}$$

$$\begin{aligned}\tau_{nm} &= t^n \delta_{nm} + t^n \mathcal{G}_0 (1-\delta_{nm}) t^m + \sum_l t^n \mathcal{G}_0 (1-\delta_{nm}) t^m \mathcal{G}_0 (1-\delta_{ml}) t^l + \ldots \\ &= t^n \delta_{nm} + \sum_l t^n \mathcal{G}_0 (1-\delta_{nl}) \tau_{ml} \quad . \end{aligned} \tag{5.26}$$

Equation 5.26 is the key formula in MST and is called the KKR-equation. By defining the *structural resolvent operator* as

$$\mathcal{G}_0^{nm} = \mathcal{G}_0 (1-\delta_{nm}) + \sum_{k,j} \mathcal{G}_0 (1-\delta_{nk}) \tau_{kj} \mathcal{G}_0 (1-\delta_{jm}) \quad , \tag{5.27}$$

the KKR-equation can be formulated in terms of $\mathcal{G}^{nm}$,

$$\tau_{nm} = t^n \delta_{nm} + t^n \mathcal{G}_0^{nm} t^m \quad . \tag{5.28}$$

In matrix notation the KKR-equation is given by

$$\boldsymbol{\tau}(\varepsilon) = \mathbf{t}(\varepsilon) + \mathbf{t}(\varepsilon)\mathbf{G}_0(\varepsilon)\boldsymbol{\tau}(\varepsilon) \tag{5.29}$$

$$= [1 - \mathbf{t}(\varepsilon)\mathbf{G}_0(\varepsilon)]^{-1}\mathbf{t}(\varepsilon) \tag{5.30}$$

$$= [\mathbf{t}^{-1}(\varepsilon) - \mathbf{G}_0(\varepsilon)]^{-1} \quad , \tag{5.31}$$

where $\mathbf{G}_0 = \{\mathcal{G}_0^{nm}\}$ is the matrix of the free structure constants, $\boldsymbol{\tau} = \{\tau^{nm}\}$ the $\boldsymbol{\tau}$-matrix, and $\mathbf{t} = \{t^n\}$ the single-site t-operator.

5.4.3 Atomic sphere approximation

Instead of using formally correct non-overlapping muffin-tin potentials, in here the atomic sphere approximation (ASA) is applied. The radius of the spheres is chosen such that the volume of the sphere is equivalent to the volume of the respective Wigner-Seitz cell

$$r_{WS} = \left(\frac{3}{4\pi} V_{WS} \right)^{1/3} \quad . \tag{5.32}$$

It turns out that the results of the ASA-potentials are better than those of the MT-potentials.

5.5 Layered system

Layered systems have two-dimensional symmetry, the symmetry in the third direction is lost for surfaces and interfaces. Therefore the position vector $\mathbf{R}_m$ is decomposed in a vector for the third direction $\mathbf{c}_p$ ($\mathbf{c}_p = p\mathbf{c}_0$ if the lattice spacing is always the same $\mathbf{c}_0$) and a translation vector for the 2D-translational invariant planes, $\mathbf{T}_i$,

$$\mathbf{R}_m = \mathbf{R}_{pi} = \mathbf{c}_p + \mathbf{T}_i \quad \text{and} \quad \mathbf{R}_n = \mathbf{R}_{qj} = \mathbf{c}_q + \mathbf{T}_j \quad . \tag{5.33}$$

Then the Green's function $\mathcal{G}_0^{mn}$ of the two muffin tin cells m and n is replaced by $\mathcal{G}_0^{pq}(\mathbf{T}_i - \mathbf{T}_j)$ of the two layers p and q because due to the 2D translation symmetry a Fourier transform can be applied for $\mathbf{k}_\parallel$,

$$\mathcal{G}_0^{mn}(\varepsilon) = \mathcal{G}_0(\varepsilon, \mathbf{R}_{pi} - \mathbf{R}_{qj}) = \mathcal{G}_0(\varepsilon, \mathbf{c}_p + \mathbf{T}_i - \mathbf{c}_q - \mathbf{T}_j) = \mathcal{G}_0^{pq}(\varepsilon, \mathbf{T}_i - \mathbf{T}_j) \quad , \tag{5.34}$$

$$\mathcal{G}_0^{pq}(\varepsilon, \mathbf{T}_i - \mathbf{T}_j) = \frac{1}{\Omega_{BZ}} \int\limits_{BZ} d\mathbf{k}_\parallel e^{-i\mathbf{k}_\parallel(\mathbf{T}_i - \mathbf{T}_j)} \mathcal{G}_0^{pq}(\varepsilon, \mathbf{k}_\parallel) \quad . \tag{5.35}$$

Thus, for layered systems the Green's function depends only on the layer indices and not on each atom in the semi-infinite region.

5.6 Screened KKR method (SKKR)

In the KKR-equation (5.31), $\boldsymbol{\tau}(\varepsilon) = [\mathbf{t}^{-1}(\varepsilon) - \mathbf{G}_0(\varepsilon)]^{-1}$, a matrix of infinite dimension in the layer indices has to be inverted. Due to the asymptotic behavior of the eigenfunctions, at positive energies the free Green function $\mathcal{G}_0$ decays very slowly in real space. Therefore an inversion can hardly be performed directly.

In order to solve this problem, the concept of screening transformations is employed which transform the KKR method in a tight-binding form. In free space and for negative energies the structure constants decay exponentially since in free space there exist no eigen-solutions of the Schrödinger equation. Introducing a positive repulsive potential α which is usually $1-2$Ry above the valence band as a reference system, the reference Green function $\mathcal{G}_r$ becomes exponentially localized in real space. Therefore the matrix elements of the structure constants $\mathcal{G}_r^{pq}(\mathbf{k}_\parallel, \varepsilon)$ can be neglected for too large distances between the layers p and q, $|p-q| > N$. In bcc and fcc systems $N \approx 3$; $\mathcal{G}_r(\mathbf{k}_\parallel, \varepsilon)$ becomes then block tri-diagonal and these blocks are related to the so-called *principal layers* containing N subsequent atomic layers.

After all quantities have been calculated in the reference system, it is necessary to transform them in the real system again,

$$\boldsymbol{\tau}_\Delta(\varepsilon) = (\mathbf{t}_\Delta(\varepsilon)^{-1} - \mathbf{G}_r(\varepsilon))^{-1} \quad , \tag{5.36}$$

$$\mathbf{G}(\varepsilon) = \mathbf{G}_r(\varepsilon)(\mathbf{I} - \mathbf{t}_\Delta(\varepsilon)\mathbf{G}_r(\varepsilon))^{-1} \quad , \tag{5.37}$$

where $\boldsymbol{\tau}_\Delta = \boldsymbol{\tau} - \boldsymbol{\tau}_r$ and $\mathbf{t}_\Delta = \mathbf{t} - \mathbf{t}_r$.

For a detailed description of the screened Korringa-Kohn-Rostoker method see Szunyogh et al. [48] and chapter 17 in Zabloudil et al. [41].

5.7 The Hamiltonian

The in the last sections formally explained MST has to be specified for a certain Hamiltonian. Within the (non-relativistic) Density Functional Theory (DFT) the Kohn-Sham Hamiltonian $\mathcal{H}$ is given by (see Chapter 2 in Zabloudil et al. [41]),

$$\mathcal{H} = \left(\frac{p^2}{2m} + V^{\mathrm{eff}}[n, \mathbf{m}]\right)\mathbf{I}_2 + \boldsymbol{\sigma}_z B_z^{\mathrm{eff}}[n, \mathbf{m}] \quad . \tag{5.38}$$

In this thesis we calculate relativistically and need therefore the Kohn-Sham-Dirac Hamiltonian $\mathcal{H}$ given by

$$\mathcal{H} = c\,\boldsymbol{\alpha} \cdot \mathbf{p} + \beta mc^2 + V^{\mathrm{eff}}[n, \mathbf{m}] + \beta \boldsymbol{\Sigma} \mathbf{B}^{\mathrm{eff}}[n, \mathbf{m}] \quad , \tag{5.39}$$

$$V^{\mathrm{eff}}[n, \mathbf{m}] = V^{\mathrm{ext}} + V^{\mathrm{el}} + \frac{\delta E_{\mathrm{xc}}[n, \mathbf{m}]}{\delta n} \quad , \tag{5.40}$$

$$\mathbf{B}^{\mathrm{eff}}[n, \mathbf{m}] = \mathbf{B}^{\mathrm{eff}} + \frac{e\hbar}{2mc}\frac{\delta E_{\mathrm{xc}}[n, \mathbf{m}]}{\delta \mathbf{m}} \quad , \tag{5.41}$$

where m is the electron mass, n the particle- and $\mathbf{m}$ the magnetization-density and $\boldsymbol{\alpha}$ and $\boldsymbol{\Sigma}$ the Dirac- and Pauli spin matrices. V^{eff} is the effective potential, V^{ext} is an external potential, and $\delta E_{\mathrm{xc}}[n, \mathbf{m}]$ is the functional of the exchange-correlation energy. The electrostatic (Coulomb) potential V^{el} involves a double sum over all interactions between the charge densities of the individual scatterers. V^{el} is separated into two contributions, the inter- and the intra-site potentials, V^{inter} and V^{intra}.

$\mathbf{B}^{\text{eff}}[n,\mathbf{m}]$ is the effective (exchange) magnetic field and $\mathbf{B}^{\text{ext}}$ is an external magnetic field.

$\boldsymbol{\alpha}$ and $\boldsymbol{\beta}$ are the Dirac- and $\boldsymbol{\sigma}_i$, $\boldsymbol{\Sigma}_i$ the Pauli (spin) matrices, given by,

$$\boldsymbol{\beta} = \begin{pmatrix} \mathbf{I}_2 & 0 \\ 0, & -\mathbf{I}_2 \end{pmatrix} \quad , \quad \mathbf{I}_2 = \begin{pmatrix} 1 & 0 \\ 0 & 1 \end{pmatrix} \quad , \tag{5.42}$$

$$\boldsymbol{\alpha}_i = \begin{pmatrix} 0 & \boldsymbol{\sigma}_i \\ \boldsymbol{\sigma}_i & 0 \end{pmatrix} \quad , \quad \boldsymbol{\Sigma}_i = \begin{pmatrix} \boldsymbol{\sigma}_i & 0 \\ 0 & \boldsymbol{\sigma}_i \end{pmatrix} \quad , \quad i = x, y, z \quad , \tag{5.43}$$

and

$$\boldsymbol{\sigma}_x = \begin{pmatrix} 0 & 1 \\ 1 & 0 \end{pmatrix} \quad , \quad \boldsymbol{\sigma}_y = \begin{pmatrix} 0 & -i \\ i & 0 \end{pmatrix} \quad , \quad \boldsymbol{\sigma}_z = \begin{pmatrix} 1 & 0 \\ 0 & -1 \end{pmatrix} \quad . \tag{5.44}$$

The unknown exchange-correlation part, $E_{\text{xc}}[n,\mathbf{m}]$, is assumed to be a local function of the spin density. In the local spin density approximation (LSDA), the exchange-correlation energy is given by

$$E_{XC}^{LSDA} = \int d\, n(r)\epsilon_{XC}[n_\uparrow(r), n_\downarrow(r)] \quad , \tag{5.45}$$

where $\epsilon_{XC}[n_\uparrow(r), n_\downarrow(r)]$ is the exchange-correlation energy per particle. Within LSDA good agreement with the experiment is achieved, although LSDA should be a good approximation in the limit of a slow variation with the charge density.

For $\epsilon_{XC}[n_\uparrow(r), n_\downarrow(r)]$ many different parametrization exist; in here we will use that of Vosko et al. [64]

5.7.1 Observables

The energy and space dependent density of states (DOS) is defined by

$$n(\varepsilon,\mathbf{r}) = \mp\frac{1}{\pi}\mathrm{ImTr}\; \mathcal{G}^{\pm}(\varepsilon,\mathbf{r},\mathbf{r}) \quad , \tag{5.46}$$

the DOS for the energy ε, $n(\varepsilon)$, by

$$n(\varepsilon) = \mp\frac{1}{\pi}\mathrm{ImTr}\; \mathcal{G}^{\pm}(\varepsilon) = \mp\frac{1}{\pi}\mathrm{Im}\int\limits_V d^3r\; \mathrm{Tr}\; \mathcal{G}^{\pm}(\varepsilon,\mathbf{r}+\mathbf{R},\mathbf{r}+\mathbf{R}) \quad , \tag{5.47}$$

and the DOS at a certain space point $\mathbf{r}$, $n(\mathbf{r})$, by

$$n(\mathbf{r}) = -\frac{1}{\pi}\;\mathrm{Im}\; Tr \int\limits_{E_V}^{E_F} dE\mathcal{G}(\mathbf{r},\mathbf{r},E) \quad . \tag{5.48}$$

The charge density, $m(\mathbf{r})$, is obtained via the integral

$$\mathbf{m}(\mathbf{r}) = -\frac{1}{\pi} \operatorname{Im} Tr \int_{E_V}^{E_F} dE \boldsymbol{\beta} \boldsymbol{\sigma}_z \mathcal{G}(\mathbf{r}, \mathbf{r}, E) \quad . \tag{5.49}$$

The number of particles N is given by

$$N = \int_{-\infty}^{\infty} d\varepsilon \; f(\varepsilon) n(\varepsilon) \tag{5.50}$$

and the integrated density of states $N(\varepsilon)$ by

$$N(\varepsilon) = \int_{-\infty}^{\varepsilon} d\varepsilon' \; f(\varepsilon') n(\varepsilon') \quad . \tag{5.51}$$

In the calculation of the magnetic anisotropy energy ΔE_a the difference of the sum of the KS-eigen values for two different magnetic configurations has to be evaluated. Within the magnetic force theorem approximation [41, 49, 50, 51], the potential is treated as frozen, i.e., the potential has to be calculated self-consistently only for one magnetic configuration. ΔE_a is then the sum of the band-energy difference ΔE_b and the dipole-dipole-energy difference ΔE_{dd} between the two magnetic configurations. In the grand canonical ensemble the band-energy is obtained by

$$E_b = \int_{-\infty}^{\varepsilon_F} d\varepsilon \; (\varepsilon - \varepsilon_F) \; n(\varepsilon) \approx \int_{\varepsilon_B}^{\varepsilon_F} d\varepsilon \; (\varepsilon - \varepsilon_F) \; n(\varepsilon) \quad . \tag{5.52}$$

In a simple classical model, the magnetic dipole-dipole-energy is obtained by (see section 26.3.4, equation (26.22) in Zabloudil et al. [41]),

$$E_{dd} = \frac{1}{c^2} \sum_{\{i,j|i \neq j\}} \left(\frac{\mathbf{m}_i \cdot \mathbf{m}_j}{|\mathbf{R}_i - \mathbf{R}_j|^3} - 3 \, \frac{[\mathbf{m}_i \cdot (\mathbf{R}_i - \mathbf{R}_j)][\mathbf{m}_j \cdot (\mathbf{R}_i - \mathbf{R}_j)]}{|\mathbf{R}_i - \mathbf{R}_j|^5} \right) \quad , \tag{5.53}$$

where the $\mathbf{m}_i$ are located at the sites $\mathbf{R}_i$.

6 Electric transport: Linear response theory

6.1 Physical observables and response functions

In this section we calculate the response of a quantum mechanical system to an external potential. The original idea traces back to Kubo in 1957 [17], a detailed description of transport theories is found also in Szunyogh [52] and in Palotás et al. [42]. The thermodynamic average of the time dependent observable $A(t)$, given by

$$A(t) = \mathrm{Tr}\{\rho(t)A\} \quad , \tag{6.1}$$

will be derived in first order perturbation theory (linear response). Here, $\rho(t)$ is the time-dependent density matrix corresponding to the time-dependent Hamiltonian $\mathcal{H}(t)$. The density $\rho(t) = \rho_0 + \Delta\rho(t)$ is reformulated such that it depends only on the known equilibrium density (i.e. for vanishing external fields) ρ_0 and the Hamiltonian,

$$\mathcal{H}(t) = \mathcal{H}_0 + \Delta\mathcal{H}(t) \quad . \tag{6.2}$$

The operator $\mathcal{H}_0$ is supposed to describe the natural motion, whereas the perturbation is described by the Hamiltonian $\Delta\mathcal{H}(t)$. The density is then given by

$$\rho(t) = \rho_0 + \Delta\rho(t),\ \rho_0 = \frac{1}{Z}e^{-\beta\mathcal{H}_0},\ Z = \mathrm{Tr}\left(e^{-\beta\mathcal{H}_0}\right) \quad . \tag{6.3}$$

The equation of motion allows to find an expression for the perturbed density $\rho(t)$ in terms of the Hamiltonian and the density ρ_0,

$$i\hbar\frac{\partial}{\partial t}\rho(t) = [\mathcal{H}, \rho(t)] \tag{6.4}$$

$$i\hbar\frac{\partial}{\partial t}\left(\rho_0 + \Delta\rho(t)\right) = [\mathcal{H}_0 + \Delta\mathcal{H}(t), \rho_0 + \Delta\rho(t)] \quad . \tag{6.5}$$

Quite clearly, the time-independent part $i\hbar\,\partial\rho_0/\partial t = [\mathcal{H}_0, \rho_0]$ vanishes. In linear response theory, also the term $[\Delta\mathcal{H}, \Delta\rho(t)]$ can be neglected because the perturbation is of second order. Therefore equation (6.5) is reduced to

$$i\hbar\frac{\partial}{\partial t}\Delta\rho(t) = [\mathcal{H}_0, \Delta\rho(t)] + [\Delta\mathcal{H}(t), \rho_0] \quad . \tag{6.6}$$

Switching to the Dirac representation,

$$X_D = e^{\frac{i}{\hbar}\mathcal{H}_0 t}Xe^{-\frac{i}{\hbar}\mathcal{H}_0 t} \quad , \tag{6.7}$$

a simple equation for $\Delta\rho_D(t)$ is obtained

$$i\hbar\frac{\partial}{\partial t}\Delta\rho_D(t) = [\Delta\mathcal{H}_D(t), \rho_0] \quad , \tag{6.8}$$

which can be integrated in a straight forward way. Again in the Heisenberg-picture the density $\rho(t)$ becomes

$$\rho(t) = \rho_0 - \frac{i}{\hbar}\int\limits_{-\infty}^{t} dt'\; e^{-i\mathcal{H}_0 t/\hbar}[\Delta\mathcal{H}'_D(t'), \rho_0]e^{i\mathcal{H}_0 t/\hbar} \quad . \tag{6.9}$$

Equation (6.9) is inserted into equation (6.1) and we obtain

$$A(t) = A_0 - \frac{i}{\hbar}\int\limits_{-\infty}^{t} dt'\; \mathrm{Tr}\left\{[\Delta\mathcal{H}'_H(t'), \rho_0]A_H(t)\right\} \tag{6.10}$$

where the observable is analogously to the density and the Hamiltonian split in two parts, $A(t) = A_0 + \Delta A(t)$. In order to evaluate the commutator, the *Kubo identity* [17, 42, 52]

$$\frac{i}{\hbar}[X_H(t), \rho] = \rho\int\limits_{0}^{\beta} d\lambda\; \dot{X}_H(t - i\lambda\hbar) \tag{6.11}$$

is applied, yielding for the quantum mechanical observable

$$A(t) = A_0 - \frac{i}{\hbar}\int\limits_{-\infty}^{t} dt'\int\limits_{0}^{\beta} d\lambda\; \mathrm{Tr}\left\{\Delta\dot{H}_H(t' - i\lambda\hbar)\rho_0 A_H(t)\right\} \quad . \tag{6.12}$$

With the definition of the Heisenberg operator, $X_H = e^{\frac{i}{\hbar}\mathcal{H}t}Xe^{-\frac{i}{\hbar}\mathcal{H}t}$ equation (6.12) becomes

$$A(t) = A_0 - \frac{i}{\hbar}\int\limits_{-\infty}^{t} dt'\int\limits_{0}^{\beta} d\lambda\; \mathrm{Tr}\left\{\Delta\dot{H}(t')\rho_0 A_H(t - t' + i\hbar\lambda)\right\} \quad . \tag{6.13}$$

The equations (6.12) and (6.13) are called the *Kubo formula*.

6.2 Electric transport and the electric conductivity tensor

As an example for a quantum mechanical observable we consider the electric current $\mathbf{J}(\mathbf{r})$ which is induced due to a time dependent electric field E_ν which is applied to the solid. The electric field and the electric current are related by the conductivity (space-time correlation function) $\sigma_{\mu\nu}(\mathbf{r}, \mathbf{r}'; t, t')$ via Ohm's law ($J_\mu \propto \sigma_{\mu\nu}E_\nu$). $\sigma_{\mu\nu}(\mathbf{r}, \mathbf{r}'; t, t')$ is given in equilibrium properties of the system, ie. in the limit of vanishing external field.

$\Delta\mathcal{H}(t)$ is the perturbation Hamiltonian due to an electric field,

$$\Delta\mathcal{H}(t) = \int d^3r\rho(\mathbf{r})\phi(\mathbf{r},t) \quad . \tag{6.14}$$

The time derivative of this Hamiltonian, $\Delta\dot{H}(t)$, appearing in equation (6.13), is obtained by applying the continuity equation, Gauß' theorem, and $\mathbf{E} = -\nabla\phi$,

$$\frac{\partial\Delta\mathcal{H}(t)}{\partial t} = -\int d^3rJ_\nu(\mathbf{r})E_\nu(\mathbf{r},t) \quad . \tag{6.15}$$

According to equation (6.13) the thermodynamic average of the time dependent electric current $\mathbf{J}(\mathbf{r},t)$ is given by

$$\begin{aligned} J_\mu(\mathbf{r},t) &= \frac{i}{\hbar}\int\limits_{-\infty}^{t} dt' \int\limits_{0}^{\beta} d\lambda \mathrm{Tr}\left\{\rho_0 \int d^3r' \left(\mathbf{J}(\mathbf{r}')\cdot\mathbf{E}(\mathbf{r}',t')\right)\mathbf{J}(\mathbf{r},t-t'+i\hbar\lambda)\right\} \\ &= \frac{i}{\hbar}\int\limits_{-\infty}^{+\infty} dt' \int d^3r'\theta(t-t') \int\limits_{0}^{\beta} d\lambda \mathrm{Tr}\left\{\rho_0 J_\nu(\mathbf{r}',0)J_\mu(\mathbf{r},t-t'+i\hbar\lambda)\right\}E_\nu(\mathbf{r}',t') \end{aligned} \tag{6.16}$$

Equation (6.16) is identified as Ohm's law,

$$J_\mu(\mathbf{r},t) = \frac{i}{\hbar}\int\limits_{-\infty}^{+\infty} dt' \int d^3r' \ \sigma_{\mu\nu}(\mathbf{r},\mathbf{r}';t,t')E_\nu(\mathbf{r}',t') \quad , \tag{6.17}$$

where $\sigma_{\mu\nu}$ is the space-time correlation function given by

$$\sigma_{\mu\nu}(\mathbf{r},\mathbf{r}';t,t') = \theta(t-t')\int\limits_{0}^{\beta} d\lambda \ \mathrm{Tr}\left\{\rho_0 J_\nu(\mathbf{r}',0)J_\mu(\mathbf{r},t-t'+i\hbar\lambda)\right\} \quad . \tag{6.18}$$

The non-relativistic current-density operator is given by

$$\mathbf{J}^{nr} = e\hbar\psi(\mathbf{r})^+(\overrightarrow{\nabla} - \overleftarrow{\nabla})\psi(\mathbf{r}) \tag{6.19}$$

and the relativistic current-density operator by

$$\mathbf{J}^{rel} = ec\psi(\mathbf{r})^+\boldsymbol{\alpha}\psi(\mathbf{r}), \tag{6.20}$$

where $\boldsymbol{\alpha}$ denote the Dirac matrices.

By translating $\sigma_{\mu\nu}(\mathbf{r},\mathbf{r}';t,t')$ to Fourier space, the famous Luttinger formula for the *wave vector and frequency dependent conductivity tensor* $\sigma_{\mu\nu}(\mathbf{q},\omega)$ is obtained. [44] $\sigma_{\mu\nu}(\mathbf{q},\omega)$ is then given in terms of the *current-current correlation function* $\Sigma_{\mu\nu}(\mathbf{q},\zeta)$, with the complex frequency argument $\zeta = \omega + i\delta$,

$$\sigma_{\mu\nu}(\mathbf{q},\omega) = \frac{\Sigma_{\mu\nu}(\mathbf{q},\zeta) - \Sigma_{\mu\nu}(\mathbf{q},0)}{\zeta} \quad , \tag{6.21}$$

where $\Sigma_{\mu\nu}(\mathbf{q},\omega)$

$$\Sigma_{\mu\nu}(\mathbf{q},\zeta) = \frac{1}{\hbar V}\int\limits_0^\infty dt\; e^{i\zeta t}\;\mathrm{Tr}\left\{\rho_0[J_\mu(\mathbf{q},t),J_\nu(-\mathbf{q},0)]\right\} \quad . \tag{6.22}$$

6.3 Kubo formula for independent particles

Up to now the formula for the physical response function was evaluated for a special observable $A = \mathbf{J}(\mathbf{r})$ and the Hamiltonian due to an electric field. But the equations were not restricted to a special equilibrium density ρ_0. Assuming Fermi particles the Fermi-Dirac distribution applies for ρ_0,

$$\rho_0 = f(H_0) = \frac{1}{e^{\beta(H_0-\mu)}+1} \quad , \tag{6.23}$$

which is developed in the basis set

$$H_0|n\rangle = \varepsilon_n|n\rangle \quad , \quad \langle m|n\rangle = \delta_{nm} \quad , \quad \sum_n |n\rangle\langle n| = I \quad . \tag{6.24}$$

The thermal average of $\Sigma_{\mu\nu}(\mathbf{q},\zeta)$ is calculated according to equation (6.22). Evaluating only the trace at first, gives

$$\begin{aligned}&\mathrm{Tr}\left\{\rho_0[J_\mu(\mathbf{q},t'),J_\nu(-\mathbf{q},0)]\right\}\\ &\qquad = \sum_{m,n}\left(f(\varepsilon_m)-f(\varepsilon_n)\right)e^{i(\varepsilon_m-\varepsilon_n)t'/\hbar}J_\mu^{mn}(\mathbf{q})J_\nu^{nm}(-\mathbf{q}) \quad ,\end{aligned} \tag{6.25}$$

where $J_\nu^{nm}(\mathbf{q})$ are the matrix elements $\langle m|J_\mu(\mathbf{q},0)|n\rangle$. $\Sigma_{\mu\nu}(\mathbf{q},\omega)$ is then given by

$$\Sigma_{\mu\nu}(\mathbf{q},\zeta) = \frac{1}{\hbar V}\int\limits_0^\infty dt\; e^{i\zeta t}\sum_{m,n}\left(f(\varepsilon_m)-f(\varepsilon_n)\right)e^{i(\varepsilon_m-\varepsilon_n)t'/\hbar}f(\varepsilon_m)J_\mu^{mn}(\mathbf{q})J_\nu^{nm}(-\mathbf{q}) \tag{6.26}$$

and by exchanging sum and integration we obtain

$$\Sigma_{\mu\nu}(\mathbf{q},\omega) = \frac{1}{\hbar V}\sum_{m,n}\left(f(\varepsilon_m)-f(\varepsilon_n)\right)J_\mu^{mn}(\mathbf{q})J_\nu^{nm}(-\mathbf{q})\int\limits_0^\infty dt\; e^{i(\hbar\zeta+\varepsilon_m-\varepsilon_n)t/\hbar} \quad . \tag{6.27}$$

The t-integration is a Laplace transform with a complex integrand, $\zeta = \omega + i\delta$, with $\delta > 0$,

$$\int\limits_0^\infty dt\; e^{(-\delta+i(\hbar\omega+\varepsilon_m-\varepsilon_n)/\hbar)t} = \left.\frac{e^{(-\delta+i(\hbar\omega+\varepsilon_m-\varepsilon_n)/\hbar)t}}{-\delta+i(\hbar\omega+\varepsilon_m-\varepsilon_n)/\hbar}\right|_0^\infty \tag{6.28}$$

and in the limit of $\delta \to 0$ $\Sigma_{\mu\nu}(\mathbf{q},\zeta)$ becomes

$$\Sigma_{\mu\nu}(\mathbf{q},\zeta) = \frac{i}{\hbar V}\sum_{m,n}\left(f(\varepsilon_m)-f(\varepsilon_n)\right)\frac{\hbar J_\mu^{mn}(\mathbf{q})J_\nu^{nm}(-\mathbf{q})}{\hbar\zeta+\varepsilon_m-\varepsilon_n} \tag{6.29}$$

and finally $\sigma_{\mu\nu}(\mathbf{q},\omega)$ is given by

$$\sigma_{\mu\nu}(\mathbf{q},\omega) = \frac{\Sigma_{\mu\nu}(\mathbf{q},\zeta) - \Sigma_{\mu\nu}(\mathbf{q},0)}{\zeta} \tag{6.30}$$

or by

$$\sigma_{\mu\nu}(\mathbf{q},\omega) = \frac{\hbar}{iV}\sum_{m,n} \frac{f(\varepsilon_m) - f(\varepsilon_n)}{\varepsilon_m - \varepsilon_n} \frac{J_\mu^{mn}(\mathbf{q}) J_\nu^{nm}(-\mathbf{q})}{\hbar\zeta + \varepsilon_m - \varepsilon_n} \quad . \tag{6.31}$$

6.4 Contour Integration Technique

It is possible to calculate equation (6.29) or equation (6.31) by evaluating the infinite double summation in m and n. But it is more convenient to use the trick of contour integration. Then the summations in m and n decouple because ε_m and ε_n in the nominators are separated. Formally the two infinite sums are then evaluated by identifying them with the Green's function.

The scope is to write the m and n dependent part of $\sigma_{\mu\nu}(\mathbf{q},\omega)$ as a contour-integral, $(f(\varepsilon_m))/(\hbar\zeta + \varepsilon_m - \varepsilon_n)$ as

$$\oint\limits_{\Gamma_x} dz\, \frac{1}{\varepsilon_m - z}\, f(z)\, \frac{1}{z - \varepsilon_n + \hbar\omega + i\delta} \tag{6.32}$$

and $-(f(\varepsilon_n))/(\hbar\zeta + \varepsilon_m - \varepsilon_n)$ as

$$\oint\limits_{\Gamma_x} dz\, \frac{1}{\varepsilon_n - z}\, f(z)\, \frac{1}{\varepsilon_m - z + \hbar\omega + i\delta} \quad . \tag{6.33}$$

We have to account for all poles in the complex area involved by the contour integrals (6.32) and (6.33), namely

- the ordinary poles $z = \varepsilon_m$ or $z = \varepsilon_n$,
- the ordinary poles $z = \varepsilon_n - \hbar\omega - i\delta$ or $z = \varepsilon_m + \hbar\omega + i\delta$, and
- the fermionic Matsubara poles due to the Fermi-Dirac distribution function, $z_k = \varepsilon_F + i(2k-1)\delta_T$, $\delta_T = \pi kT$.

It is easy to obtain the residua of the ordinary poles, the contour includes the real axis between the bottom energy ε_b and the Fermi energy ε_F.

The number of residua due to the Matsubara poles depends on the extension of the contour in direction of the imaginary axis. The substitution in equations (6.32) and (6.33) is done for both summands in equations (6.31), $f(\varepsilon_m)/(\hbar\zeta + \varepsilon_m - \varepsilon_n)$ with a corresponding contour Γ_1 and $-f(\varepsilon_n)/(\hbar\zeta+\varepsilon_m-\varepsilon_n)$ with a contour Γ_2. The contours Γ_1 and Γ_2 are chosen such that reflection symmetry (with respect to the real axis) applies because then the sum due to the two terms can be simplified best. Γ_1 takes into account N_1 Matsubara poles with positive imaginary part and N_2 Matsubara poles with negative imaginary part while Γ_1 has N_2 in the upper and N_1 in the lower complex plane.

Because of the substitution in equations (6.32) and (6.33) in the contour integral there are two nominators with decoupled ε_m and ε_n. It is possible to identify the double sum in m and n as a product of Green functions,

$$\mathrm{Tr}\{G(z)\ J_\mu\ G(z+\hbar\zeta+i\delta)\ J_\nu\} \quad \text{and} \quad \mathrm{Tr}\{G(z)\ J_\mu\ G(z-\hbar\zeta-i\delta)\ J_\nu\} \quad . \tag{6.34}$$

Exploiting the symmetry therefore the current-current correlation function $\Sigma_{\mu\nu}(\mathbf{q},\zeta)$ becomes

$$\begin{aligned}\Sigma_{\mu\nu}(\mathbf{q},\zeta) = &\oint_{\Gamma_1} dz f(z)\tilde{\Sigma}_{\mu\nu}(\mathbf{q},z+\hbar\zeta+i\delta,z) \\ &-\left(\oint_{\Gamma_1} dz f(z)\tilde{\Sigma}_{\mu\nu}(-\mathbf{q},z-\hbar\zeta+i\delta,z)\right)^* \\ &-2i\delta_T\sum_{k=-N_2+1}^{N_1}\Big(\tilde{\Sigma}_{\mu\nu}(\mathbf{q},z+\hbar\zeta+i\delta,z)+\tilde{\Sigma}_{\mu\nu}(-\mathbf{q},z-\hbar\zeta+i\delta,z)^*\Big)\end{aligned} \tag{6.35}$$

where $\tilde{\Sigma}_{\mu\nu}(\mathbf{q},z_1,z_2)$ is given by

$$\begin{aligned}\tilde{\Sigma}_{\mu\nu}(\mathbf{q},z_1,z_2) &= -\frac{1}{2\pi V}\mathrm{Tr}\left(J_\mu(\mathbf{q})\ G(z_1)\ J_\nu(-\mathbf{q})\ G(z_1)\right) \quad , \\ \tilde{\Sigma}_{\mu\nu}(-\mathbf{q},z_2,z_1) &= \tilde{\Sigma}_{\mu\nu}(\mathbf{q},z_1,z_2) \quad , \\ \tilde{\Sigma}_{\mu\nu}(\mathbf{q},z_1^*,z_2^*) &= \tilde{\Sigma}_{\mu\nu}(\mathbf{q},z_1,z_2)^* = \tilde{\Sigma}_{\mu\nu}(-\mathbf{q},z_2,z_1)^* \quad ,\end{aligned}$$

and the imaginary part $i\delta_i$ of the contour Γ_i is given by

$$(2N_i-1)\delta_T < \delta_i < (2N_i+1)\delta_T \quad , \quad i=1,2 \quad . \tag{6.36}$$

Together with equation (6.29) and (6.30) we have now an expression for the conductivity obtained.

7 Computational procedure

Fig. 7.1 schematically shows the types of calculations that have to be carried out. The arrows mark the sequence of the calculations.

As a first step the effective scattering potentials for bulk and surface multi-layer structures are calculated self-consistently in terms of the spin-polarized relativistic screened Korringa-Kohn-Rostoker (SKKR) method for layered systems [41, 48, 63]. In here, the density functional parametrization of Vosko *et al.* [64] is used. A sufficient number of buffer layers has to be considered to guarantee reliable matching to the semi-infinite substrate and also a sufficient number of vacuum layers to join up to the semi-infinite vacuum.

The corresponding potentials serve then as input for the evaluation of the complex layer-resolved magneto-optical conductivity tensor $\sigma_{\mu\nu}(\omega)$. For a particular photon energy $\sigma_{\mu\nu}(\omega)$ is determined fully relativistically in terms of the Luttinger equation (6.30) for finite frequencies [43, 44, 45, 65, 66, 67, 68, 69].

Only then, as a third step, the in Chapter 4 described calculation of the magneto-optical properties of the system by means of the 2×2 matrix technique can be performed [69, 53]. In using this scheme the permittivity $\varepsilon(\omega)$ for bulk and the surface, are calculated for certain photon energies $\hbar\omega$.

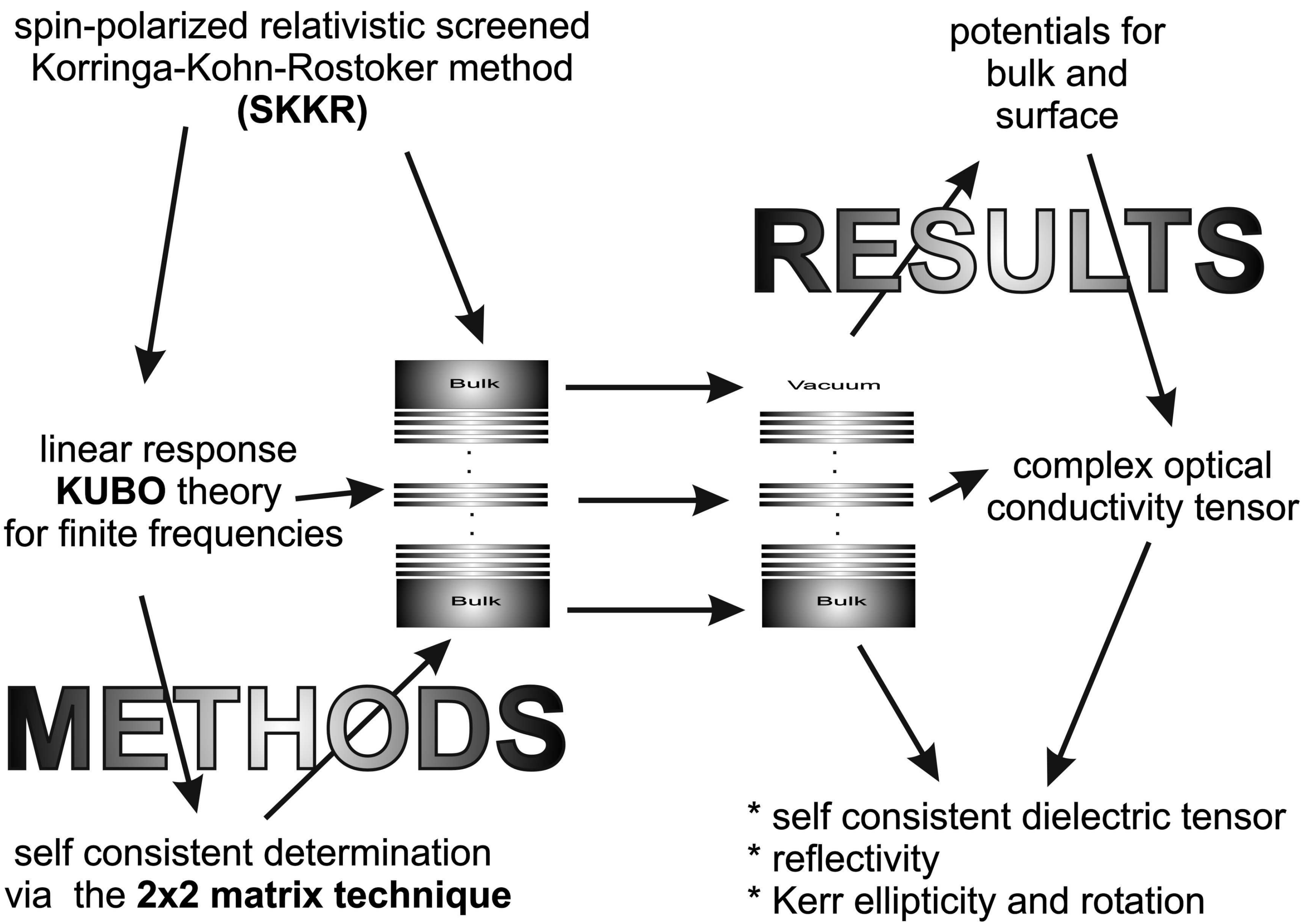

Figure 7.1: Computational scheme for an *ab-initio* calculation of optical properties.

Part III

Results

8 Introduction

The theoretical and computational methods described in the previous chapters should be applied now to some materials of interest. In materials science, the magneto-optical Kerr effect (MOKE) has a long list of applications that are located in fundamental as well as in technological research. The scope of this thesis is to cover some of the most amazing physical phenomena in surface science and describe them by means of the *ab-initio* calculated MOKE. Two examples from fundamental research and one from technological research are analyzed. First, a magnetic reorientation transition is discussed, then, the magnetic inter-layer exchange coupling in a tri-layer system is investigated. Last but not least, one chapter is devoted to a technologically relevant material that is a candidate to become a future material for perpendicular magneto-optic recording.

8.1 Optical properties of para-magnetic substrates

But before investigating these highly interesting phenomena, para-magnetic substrates are selected and their optical properties discussed, see Chapter 9. Gold, copper, and platinum were decided to be worth to be the subject of our investigations. Au is known because of its strong relativistic effects and it seems quite natural to investigate also its magneto-optical properties. Cu is a common substrate for experimental investigations. Pt is interesting because it can be easily magnetically polarized and contributes significantly to magneto-optical effects.

8.1.1 Au(100)

Exploiting Au(100) as a model system, we show that, whenever realistic systems, i.e., systems with a surface, have to be dealt with, a comparison with experimental data has to be carried out with extreme care, since not only the applied preparation technique, but also the thickness of the prepared films enters the experimental observations. It also has to be noted that the term bulk in many cases can be quite misleading, not only because any kind of measurement is carried out from the outside, that is for an at best semi-infinite system, but also because bulk very often only refers to a fictitious quantity, obtained by extrapolating certain thickness parameters to infinity. In the present study the permittivity of bulk Au is needed as starting value for an iterative procedure aiming at an evaluation of the surface reflectivity.

8.1.2 Cu(100)

We will calculate the energy-dependent permittivity and the complex refractive index for Cu(100) bulk in an energy region of 1.5eV$<\hbar\omega<$9eV. Regarding the order of magnitude, the results compare reasonable well to experiment. The structure of the spectrum is not well reflected in the ab-initio calculations. This may be attributed to missing many-body effects in the calculations or to the experimental procedure.

8.1.3 Pt(111)

This substrate has been studied in some detail by Vernes et al. [54]

8.2 Magneto-optics in magnetic multi-layer structures

8.2.1 Reorientation transition

The reorientation transition of the magnetization was studied for Fe_n/Au(100) as there was experimental (Kerr intensity measurements) and theoretical (magnetic anisotropy energy calculations) evidence for it. At an Fe thickness of approximately 3 mono-layers (ML) the transition from a normal-to-plane to an in-plane easy-axis occurred, see Chapter 10.

The purpose of the present calculations is to illustrate in some detail the change of the magneto-optical properties near and at this reorientation transition. In this investigation not only the thickness of the Fe film is varied, but also the geometry including the angle of incidence, β, and the orientation of the magnetization, α. The reorientation of the ground-state magnetization is seen in a spontaneous decrease in the ab-initio calculated Kerr rotation angles θ_K at a Fe thickness between 3 and 4 mono-layers (ML). With the exception of grazing incidence ($\beta = 90^0$), the same behavior is observed for all angles β.

Interesting is the variation of the MOKE with the angle of incidence, where the largest absolute magnitude of θ_K is found for $\beta \approx 70^0$. The angle of incidence dependence of θ_K and ε_K obtained from the first-principles calculations are then compared the the two-media formula, confirming the code for the L-MOKE and the P-MOKE at oblique incidence.

In the case of normal incidence, a direct proportionality of the Kerr rotation angles and the normal component of the magnetization is demonstrated by varying the orientation of the magnetization, α. Experimentally, the latter is changed when an external field is applied normal to the ground-state of the system. In a simple phenomenological picture the equilibrium orientation of the moments is obtained by minimizing the sum of the magneto-static and the magnetic anisotropy energy. This implies a relation between the Kerr angles and the magnetic field strength $\mathbf{H}$.

8.2.2 Inter-layer exchange coupling

It is well known that the type of coupling, anti-ferromagnetic (AFM) or ferromagnetic (FM), in a multi-layer system influences the shape of the hysteresis curve, a feature which is frequently exploited experimentally to record the underlying magnetic configuration. It will be shown that the type of coupling can also be determined from the polar magneto-optic Kerr rotation and ellipticity angles θ_K and ϵ_K at vanishing external magnetic field, provided that for all spacer thicknesses the same (absolute) units apply for θ_K and ϵ_K.

As an example for the inter-layer exchange coupling (IEC) serves the experimentally and theoretically investigated Cu/Ni tri-layer system, $\mathrm{Cu_4Ni_8Cu}_n\mathrm{Ni_9/Cu(100)}$, $n = 2, \ldots, 10$. [55] As to be expected the occurring oscillations in the Kerr angles with respect to the spacer thickness resemble closely those for the inter-layer exchange coupling energy, see Chapter 11.

Contrary to the common belief, in this ab-initio investigation we found out that the Kerr signals are not direct proportional to the *total* magnetic moment. It is shown that in order to assign at least indirectly the size and sign of the Kerr angles and therefore the type of coupling to a kind of total magnetic moment, effective layer-resolved moments have to be to considered. The modification of the magnetic moments is carried out by taking a finite penetration depth into account.

8.2.3 Perpendicular magneto-optic recording

Presently [27, 56] magneto-optical storage media promise the highest storage densities with the constraint of a high data security at respectable data transfer rates. The commercially available RE-TM alloys (e.g. GdTbFe) have several deficiencies, e.g. the easy oxidation of the RE metal component. The needed protective layer complicates the structure and makes the manufacture of the MO discs cumbersome. Furthermore RE-TM alloys are limited to a long-wave length region because the MO Kerr rotation decreases at higher energies. Consequently the resolution and the areal density cannot be further increased by using lasers with shorter wave-lengths.

However, in metal multi-layers highly corrosion and oxidation resistant metal constituents can be chosen avoiding the necessity of protective layers.[57] CoPt super-lattices resist oxidation more effectively than RE-TM alloys and the pulsed laser heating does not destroy the layered structure.[58, 59] Co and Fe based multi-layer structures are the most promising MO media with improved blue response, with CoPt structures being the best. [60] In agreement with experimental observations, our *ab-initio* calculated Kerr rotation angle has a peak at 4eV.

Furthermore, in CoPt superstructures the magnetic anisotropy strongly depends on the ratio between Co and Pt thicknesses and they can be produced such that the ground-state magnetization is perpendicular.

Perpendicular recording in the context of the super-paramagnetic limit is believed to allow the highest areal densities because of thicker media permitting smaller diameter grains, a higher coercitivity, and a higher signal to noise ratio (SNR). The estimated increase in the areal density is a factor 2 to 8 compared to longitudinal recording. High SNR, high coercitivity and a high ratio of H_c/M_s (coercitivity field / saturation magnetization) have to be achieved.

In the literature, two different perpendicular media are discussed: granular (CoCr-type) media and continuous multi-layer media (CoPd, CoPt multilayer). The advantage of the former is a good SNR, the advantage of the latter is the tunability in the parameters H_c and M_s. [61] Continuous multi-layer media have wavy domain walls leading to a high noise. Thus a sort of domain wall pinning technique is mandatory, e.g., in the CGC (Coupled Granular Continuous) media, i.e. a soft underlayer with a first deposited granular CoCr based medium and a CoPd or CoPt multi-layer structure on top. The walls of the continuous layer are pinned with the granular layer at magnetization transitions yielding narrower domain walls. [62]

The present investigation is focused on the analysis of continuous CoPt multi-layer structures, see Chapter 12. The first topic is to analyze the photon energy dependence, the second more fundamental question is the asymptotic behavior of the Kerr angles with the repetition number n of $(\mathrm{Pt}_x\mathrm{Co}_y)_n$ blocks.

9 Substrates

9.1 Convergence considerations for the bulk permittivity

In the numerical procedure to obtain the bulk permittivities it is necessary to carry out a convergence study. Calculating the bulk permittivity is done by sandwiching a number of layers (in our case an integer multiple of three) between two semi-infinite systems.

A numerical criterion for the convergence of the bulk permittivity with respect to the number N of bulk layers is defined as follows. In a bulk cubic system characterized by three-dimensional periodicity the in-plane and the out-of-plane component of the permittivity, $\varepsilon_{xx}(N)$ and $\varepsilon_{zz}(N)$, have to be the same. Therefore the difference between these components, $\Delta_\varepsilon(N)$,

$$\Delta_\varepsilon(N) = |\varepsilon_{xx}(N) - \varepsilon_{zz}(N)| \quad ,$$

should vanish in the limit of an infinite layer number, where

$$\lim_{N\to\infty} \Delta_\varepsilon(N) = 0 \quad .$$

9.2 Au(100)

In Fig. 9.1 the difference $\Delta_\varepsilon(N)$ as defined in Section 9.1 is shown with respect to N together with the relative differences $2\Delta_\varepsilon(N)/|\varepsilon_{xx}(N) + \varepsilon_{zz}(N)|$, $\Delta_\varepsilon(N)/|\varepsilon_{xx}(N)|$, and $\Delta_\varepsilon(N)/|\varepsilon_{zz}(N)|$, see Section 7.

For bulk gold the present theoretical results compare reasonably well with the experimental data obtained by Hagemann *et al.* [70] and of Weaver *et al.* [71]. The principal shape of the curves looks alike; for small photon energies $\varepsilon(\omega)$ assumes quite large values, see Fig. 9.2, owing to the finite life-time broadening δ (see equation (4.1)).

Using now the results of the bulk calculation as initial values in Equations (4.13) and (4.14), $\varepsilon(\omega)$ was investigated for an Au(100) surface. It turns out that the order of magnitude of the theoretical permittivity differs considerably from the experimental data of Bader *et al.* [72] and those of Truong *et al.* [73], which in turn differ considerably from each other.

In order to take into account these differences in Figs. 9.3- 9.6, showing the real an imaginary part of ε_{xx} and ε_{zz}, the experimental data are shifted and therefore different ordinates apply.

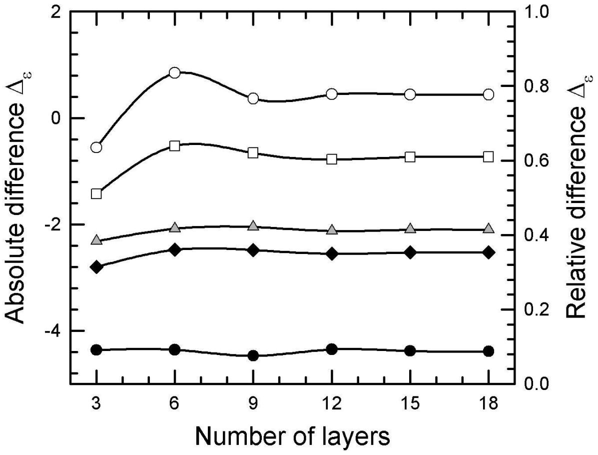

Figure 9.1: Convergence of the Au calculation to bulk with respect to the number of Au layers sandwiched between two semi-infinite systems of Au where the layer quantities are bulk like if the difference between the out-of-plane (ε_{zz}) and the in-plane components (ε_{xx} and ε_{yy}) of the permittivity vanishes: solid circles refer to $\mathrm{Re}(\Delta_\varepsilon)$, open circles to $\mathrm{Im}(\Delta\varepsilon)$ (ordinate is the left y-axis); solid diamonds to $|2\Delta_\varepsilon|/|\varepsilon_{xx}+\varepsilon_{zz}|$, triangles to $|\Delta_\varepsilon|/|\varepsilon_{xx}|$, and squares to $|\Delta_\varepsilon|/|\varepsilon_{zz}|$. For the relative differences the ordinate to the right applies.

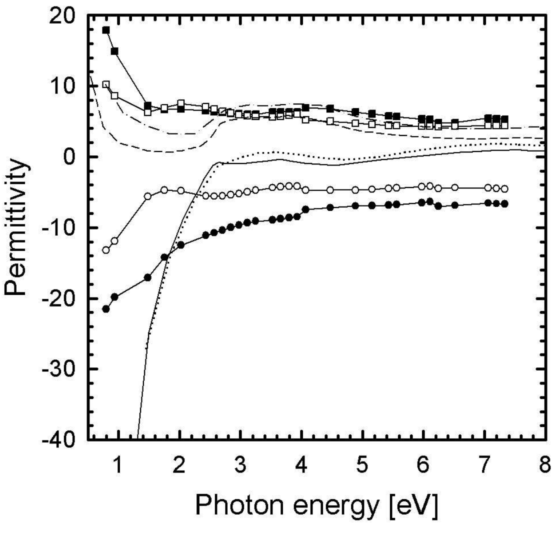

Figure 9.2: Permittivity for bulk Au. The experimental values of $\mathrm{Re}(\varepsilon_{xx})$ and $\mathrm{Im}(\varepsilon_{xx})$ of Weaver *et al.* [71] are denoted by solid and dashed lines, respectively, those of Hagemann *et al.* [70] by dotted and dash-dotted lines. The solid circles and the solid squares refer to the theoretical values of $\mathrm{Re}(\varepsilon_{xx})$ and $\mathrm{Im}(\varepsilon_{xx})$, the corresponding open symbols to $\mathrm{Re}(\varepsilon_{zz})$ and $\mathrm{Im}(\varepsilon_{zz})$.

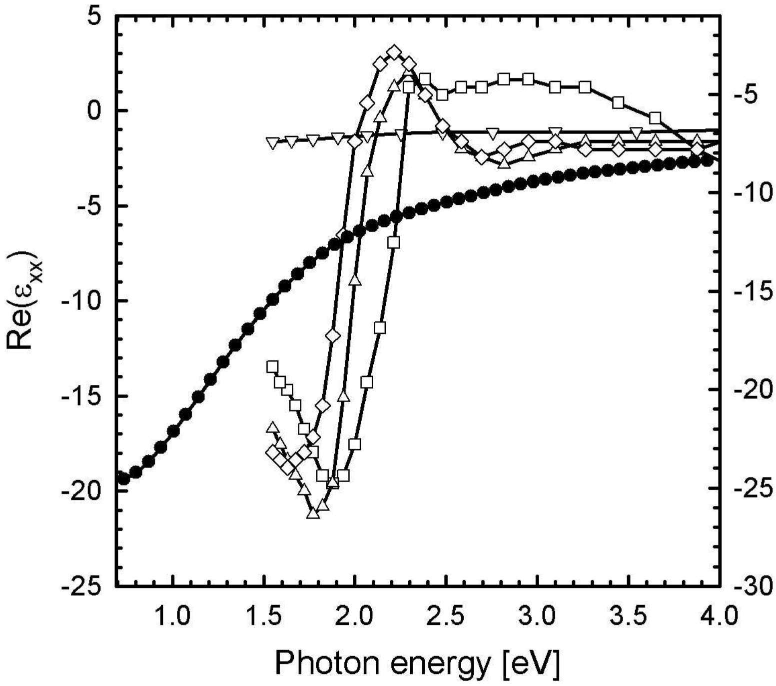

Figure 9.3: Re(ε_{xx}) for Au(100). Full circles refer to the calculated values; open squares, up triangles, and diamonds correspond in turn to the experimental data for the 3nm, 7.5nm and 10nm Au films, respectively, measured by Truong *et al.* [73]; open down triangles refer to the experimental data obtained by Bader *et al.* [72]. The left ordinate applies to the experimental data, and the right to the calculated values.

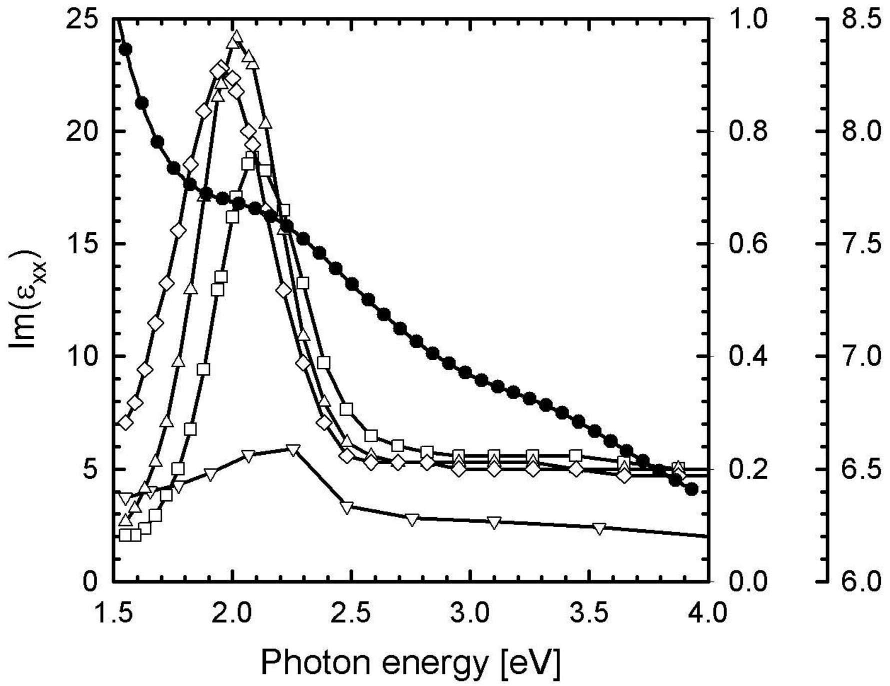

Figure 9.4: Im(ε_{xx}) for Au(100). The outer right ordinate applies to the calculated values, the inner right ordinate to the experimental data of Bader *et al.* [72] and the left to all other values. See also Fig. 9.3.

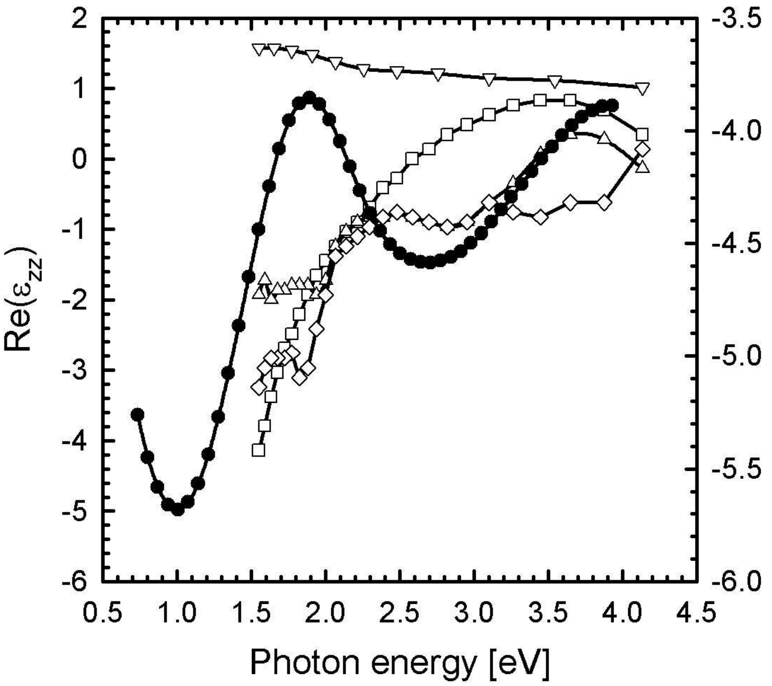

Figure 9.5: Re(ε_{zz}) for Au(100). See also Fig. 9.3.

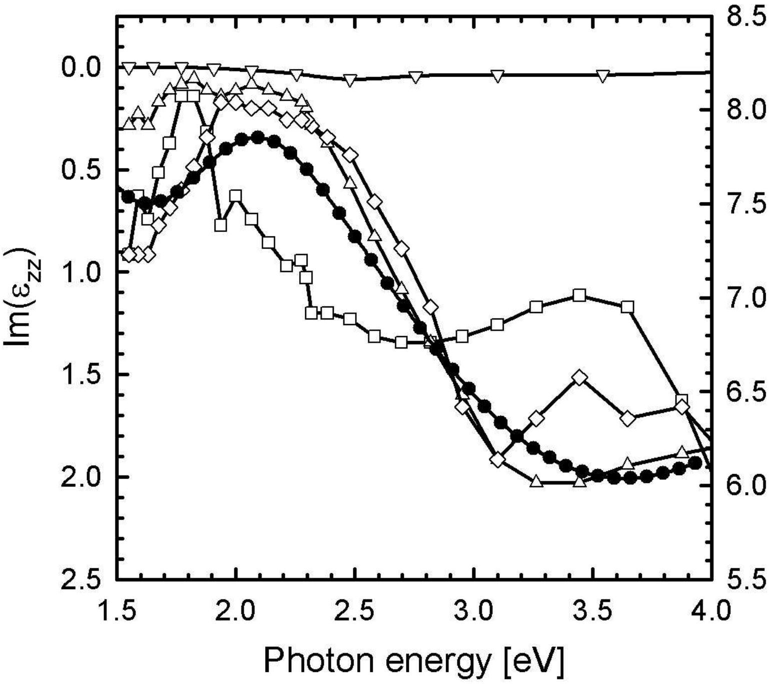

Figure 9.6: Im(ε_{zz}) for Au(100). See also Fig. 9.3.

It should be mentioned that Au surfaces usually suffer somewhat from surface reconstruction. In the experiments of Bader *et al.* [72] the surface was produced by depositing gold nano-particles in a solvent onto a glass plate and evaporating the solvent afterwards. In the experiments of Truong *et al.* [73], gold was evaporated onto glass substrates and annealed for two hours. Thus, depending on the method of preparation, fundamental differences in the surface structure of Au can to exist. The present calculations refer to perfect single crystal surfaces. Besides the fact that the experimental ambiguities affect the absolute size of the permittivity, all surface investigations (both experimental works [72, 73] and the present theoretical study) detect one common feature, namely an anomalous adsorption at the surface, an effect which is not present for bulk Au. It is indeed reassuring that in all three studies the photon energies at which the peak in the permittivity occurs have rather similar values.

Independent of the film thickness, always only two-dimensional rotational symmetry applies. Therefore all investigations of the permittivity show different results for the ε_{xx} and ε_{zz} components. The calculated values of Re(ε_{xx}) for Au(100), see Fig. 9.3, have a maximum at about 1.9eV and a kind of undulation at approximately 2.4eV, which can also be seen in the experimental values at 2.4eV for the thinnest film and at 2.2eV for the thickest fim. The calculated values of Re(ε_{zz}) for Au(100), see Fig. 9.5, appear to be in reasonable good qualitative agreement with the measured data [73], although $\varepsilon_{zz}(\omega)$

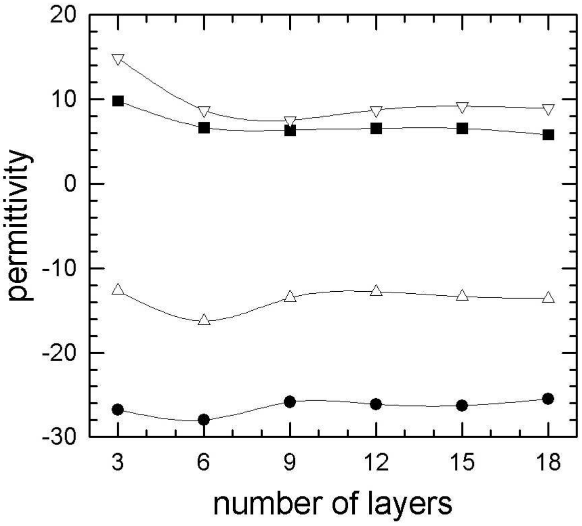

Figure 9.7: Convergence of the permittivity of Cu bulk with respect to the number of sandwiched Cu layers. Circles, squares, up and down triangles denote in turn Re(ε_{xx}), Im(ε_{xx}), Re(ε_{zz}) and Im(ε_{zz}).

seems to depend strongly on the film thickness. For instance, the experimental curves for 3nm and 7.5nm film thickness change sign at photon energies above 2.6eV and 3.4eV, respectively, while the calculated curve and the measured curve for 10nm do not change sign below 3.5eV.

9.3 Cu(100)

As described in Chapter 7 and in Section 9.1 the permittivity of Cu bulk was calculated by joining up two semi-infinite Cu bulk regions sandwiching $3n$, $(n = 1, ..., 6)$, monolayers of Cu. Fig. 9.7 shows the variation of the diagonal elements $\varepsilon_{xx} = \varepsilon_{yy}$ and ε_{zz} of the permittivity tensor with the number of sandwiched Cu layers. Only in a three–dimensional periodic (bulk) system, see Section 9.1, ε_{xx} and ε_{zz} are identical, a relation that by exploiting only two-dimensional translational symmetry cannot be reproduced completely [43, 45, 67]. Here we stop when the values of ε_{xx} and ε_{zz} reach a constant value with respect to n.

Fig. 9.8 shows the differences Re($\varepsilon_{xx} - \varepsilon_{zz}$) and Im($\varepsilon_{xx} - \varepsilon_{zz}$) and a comparison of the three relative differences $|\varepsilon_{xx} - \varepsilon_{zz}|/|\varepsilon_{xx} + \varepsilon_{zz}|$, $|\varepsilon_{xx} - \varepsilon_{zz}|/(2|\varepsilon_{xx}|)$ and $|\varepsilon_{xx} - \varepsilon_{zz}|/(2|\varepsilon_{zz}|)$. As can be seen, for more than 12 sandwiched layers these differences become nearly constant, i.e., the bulk value of the permittivity can be evaluated with sufficient accuracy.

Furthermore, a comparison between the frequency-dependent dielectric tensor elements of Cu(100) bulk with the experiment was performed, see Fig. 9.9. In Fig. 9.10 the refrac-

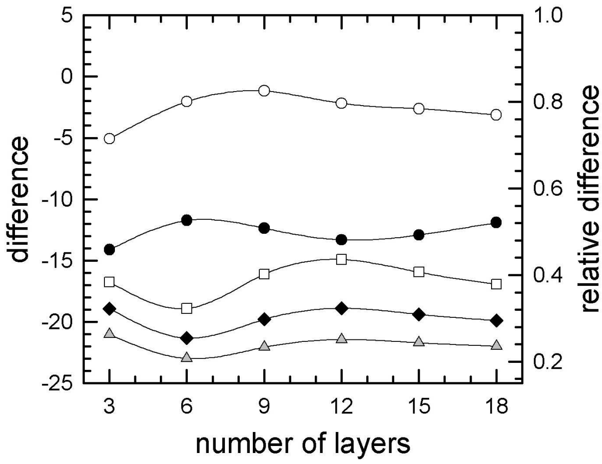

Figure 9.8: The difference between the diagonal components of the permittivity of Cu bulk as a function of the number of sandwiched Cu layers. The left ordinate applies to the difference $\Delta\varepsilon \equiv \varepsilon_{xx} - \varepsilon_{zz}$ (full circles: real part, open circles: imaginary part). The right ordinate applies to the relative differences defined as $|\Delta\varepsilon|/|\varepsilon_{xx} + \varepsilon_{zz}|$ (diamonds), $|\Delta\varepsilon|/(2|\varepsilon_{xx}|)$ (triangles), and $|\Delta\varepsilon|/(2|\varepsilon_{zz}|)$ (squares).

tive index calculated from the permittivity was compared to the same experiment. The coarse comparison shows that the theoretical values have the correct order of magnitude and that the range of the experimental results is quite broad.

It turns out that for energies between 2.5 and 4eV the correspondence is better than in the lower or higher energy regime. Quite noticeable is the minimum in the imaginary part of ε_{xx} and ε_{zz} and the maximum at 5eV which is not reflected in the theoretical calculations. The reason of this misfit may be that in the theory many-body interactions are not taken into account.

But indeed, also the experimental data has to be interpreted with care. It is of importance if the measurements are performed at oblique incidence because the permittivities are determined indirectly from reflection. From the approximative two-media formulas (3.80) and (3.89) we see that the Kerr angles for normal and oblique incidence are related by a (photon) energy-dependent factor. If this was not taken into account, this would cause a further misfit between the experimental and the theoretical results.

Furthermore the surface orientation has a large influence on the structure of the spectrum.

Additionally to the geometrical problems, neither the permittivity nor the refractive index are directly measured but they are calculated from the reflectivity $R(\omega)$. Via a Kramers-Kronig transformation the complex refractive index is obtained then. This step is very unstable with respect to the integration boundaries. In principle the whole spectrum

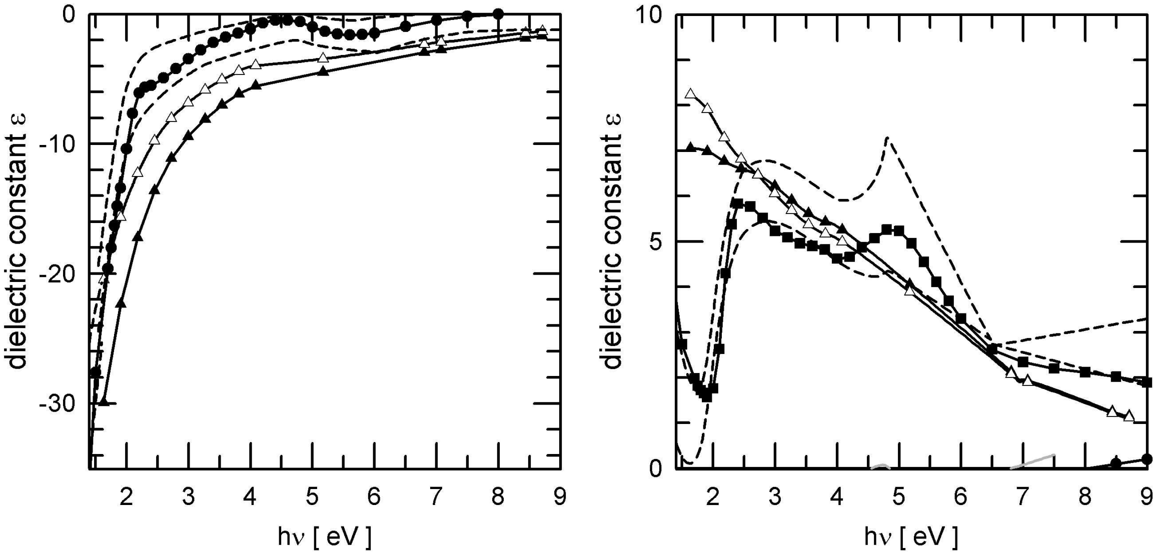

Figure 9.9: The dielectric diagonal tensor elements of Cu. *Left plot:* the real part of the dielectric constant, full triangles denote the theoretical Re(ε_{xx}), open triangles the theoretical Re(ε_{zz}), full circles the measured Re(ε_{xx}) [70] *Right plot:* the imaginary part of the dielectric constant, full triangles denote the theoretical Im(ε_{xx}), open triangles the theoretical Im(ε_{zz}), full circles the measured Im(ε_{xx}) [70]. The dashed lines in both plots mark the range of available experimental results.

$(-\infty, +\infty)$ has to be known which is, of course, impossible. Then the permittivity is determined from the refractive index which may involve further errors.

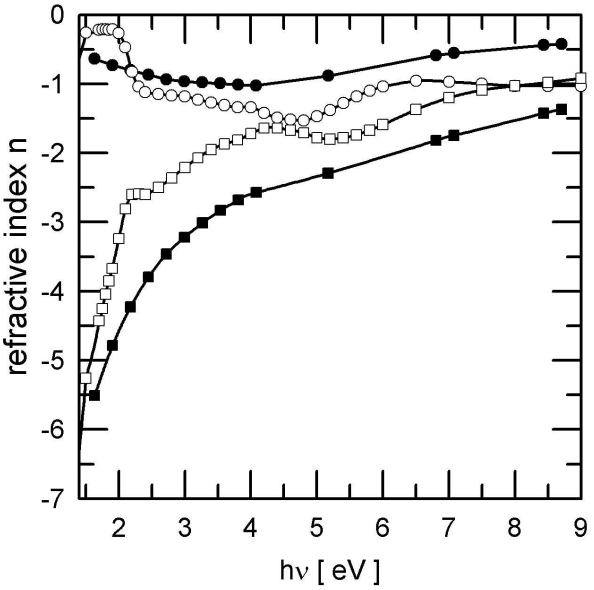

Figure 9.10: The refractive index of Cu. Full symbols denote the theoretical refractive indices, open the experimental ones [70]. Circles are used for the real part, squares for the imaginary part.

10 The reorientation transition in $\mathrm{Fe_n}$/Au(100)

10.1 Experimental and Theoretical evidence

10.1.1 Kerr intensity measurements

Back in 1989 Liu and Bader [25] reported on an in-situ surface magneto-optic Kerr effect (SMOKE) measurement for Fe on Au(100). They found sub-monolayer ferromagnetism, which, however, was unstable because of diffusion of Fe into the Au substrate and also because of Au segregation on top of the surface. Furthermore, they observed that the Fe/Au(100) system had no thermally stable out-of-plane easy axis in any thickness range. Grown at room temperature, Fe on Au(100) exhibited an in-plane easy axis in the monolayer regime, grown at 100K the easy axis turned out to be out-of-plane for films thinner than 2.8 mono-layers (ML) and in-plane for thicker films. As a comparison will be made to these measurements, it seems appropriate to recall important experimental details of this study, namely (1) crossed magnetic fields (oriented in-plane and normal to the film plane) were used to sequentially monitor the corresponding magnetization components, whereby the in-plane and the normal-to-plane configurations were referred to as longitudinal and polar geometries, respectively, (2) a p-polarized He-Ne laser source was used; and (3) as analyzer served a crystal prism polarizer nearly crossed with the incident polarization. The experimental evidence for the reorientation transition can be summarized as follows: if the easy axis was in-plane then the longitudinal SMOKE signal yielded a square hysteresis loop while the polar SMOKE signal produced no hysteresis. If, however, the easy axis was normal to the film then the polar SMOKE signal yielded a square hysteresis loop and the longitudinal SMOKE signal showed no hysteresis. In a regime of canted magnetization hysteresis related to both configurations occurred. At a given film thickness the Kerr intensity was identified with the height of the hysteresis loop in the remanent state.

10.1.2 Theoretical magnetic anisotropy energy ΔE_a

Theoretically, the reorientation transition in Fe_n/Au(100) was shown by calculating the magnetic anisotropy energy ΔE_a, defined as the sum of the band energy ΔE_b and the magnetic dipole-dipole interaction energy ΔE_{dd}, by means of the spin-polarized relativistic version of the SKKR method [63]. A perpendicular orientation of the magnetization for $n \leq 3$ and an in-plane magnetization for $n \geq 4$ was found.

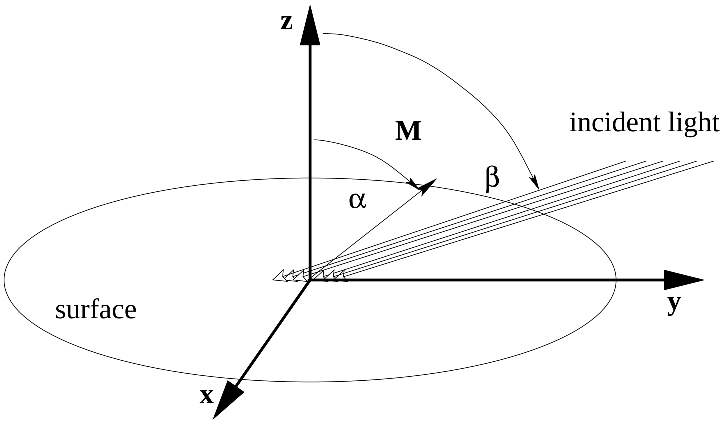

Figure 10.1: Kerr set-up used in the calculations in the case of a *p*-polarized incident light. Here α and β specify the orientation of the magnetization $\mathbf{M}$ and the direction of the incident light, respectively. Both are specified with respect to the surface normal and lie in the plane of incidence.

10.2 Computational considerations

The calculations for Fe$_n$/Au(100), $n = 1, ..., 6$, were performed as explained in Section 7.

10.2.1 The geometry

The present calculations involve a change of the angle of the magnetization (α) and the angle of incidence of light (β) which are defined in Fig. 10.1. The angle α is varied only for normal incidence of light ($\beta = 0^0$) between 0^0 and 90^0 and a scan over the angle β between 0^0 and 90^0 is performed only for the ground-state orientation of the magnetization ($\alpha = 0^0$ or 90^0).

10.2.2 The energy

The research in the literature for experimental spectra of the Kerr rotation angle θ_K and ellipticity angle ε_K for Fe/Au multi-layer structures provided only results for $(\mathrm{Fe}_n\mathrm{Au}_n)_N$ super-lattice structures on a Au substrate [74] but nothing for simply Fe$_n$/Au(100). The calculations should be performed at an energy in the visible regime where simultaneously large (experimentally detected) θ_K and ε_K occur. The photon energy satisfying this condition found for the $(\mathrm{Fe}_3\mathrm{Au}_3)_{16}$ super-lattice structures is 3.8eV.

For this particular photon energy the magneto-optical conductivity tensor was determined and the Kerr angles were calculated accounting for multiple reflections and interferences.

	number of layers					
Fe	1	2	3	4	5	6
Au	6	5	4	6	5	7

Table 10.1: $\mathrm{Fe}_n\mathrm{Au}_m$. The number of Au buffer layers which were used for a specific number of Fe layers.

10.2.3 Convergence of the results

Before the reorientation transition in Fe_n/Au(100) can be discussed it is necessary to find out (1) which accuracy is necessary and (2) how many Au buffer layers are needed to calculate the conductivity using Luttinger's formula.

As was experienced in calculating potentials, anisotropy energies or magnetic moments by means of the SKKR method, at maximum 4 Au buffer layers are noticeable influenced by the Fe layers. Fig. 10.2 shows the the layer-resolved spin magnetic moments in Fe_3/Au(100) which reflect the depth of the material's polarization.

10.2.3.1 The accuracy

Fig. 10.3 shows the result of a convergence calculation with respect to the tolerance which was performed for $n = 3$. The accuracy of the conductivity tensor, $\sigma^{pq}_{\mu\nu}$, is described by ϵ_z and $\epsilon_{\mathbf{k}}$ which are the tolerances in the complex energy (ϵ_z) and the **k**-space ($\epsilon_{\mathbf{k}}$) integration, [66]. It turns out that a tolerance in E- and **k**-integration $\leq 10^{-4}$ has to be demanded.

Fig. 10.4 shows that the MO Kerr angels for a tolerance of 10^{-2} are significantly different to those for a tolerance of 10^{-5}, thus, it is crucial to chose the tolerance with caution.

10.2.3.2 The number of Au buffer layers

If only the relative Kerr angles of Fe_n/Au(100) are of interest, it is a possibility to calculate all systems with the same number of gold layers based on the assumption that the calculations for all systems ($n = 1 - 6$) are afflicted by the same error. The difference between the systems with varying number of buffer layers (according to Tab. 10.1) and those with fixed is seen in Fig. 10.5. Compared to the error that is made for too large tolerances, the deviation between the two described cases is of minor importance.

In order to obtain a clearer picture about the dependence on the number of buffer layers, Fig. 10.6 compares the MO Kerr effect for the system Fe_3/Au(100) for different Au buffer thicknesses. The error that is made by calculating for less Au buffer layers is noticeable but compared to the error associated with a bad accuracy it is negligible.

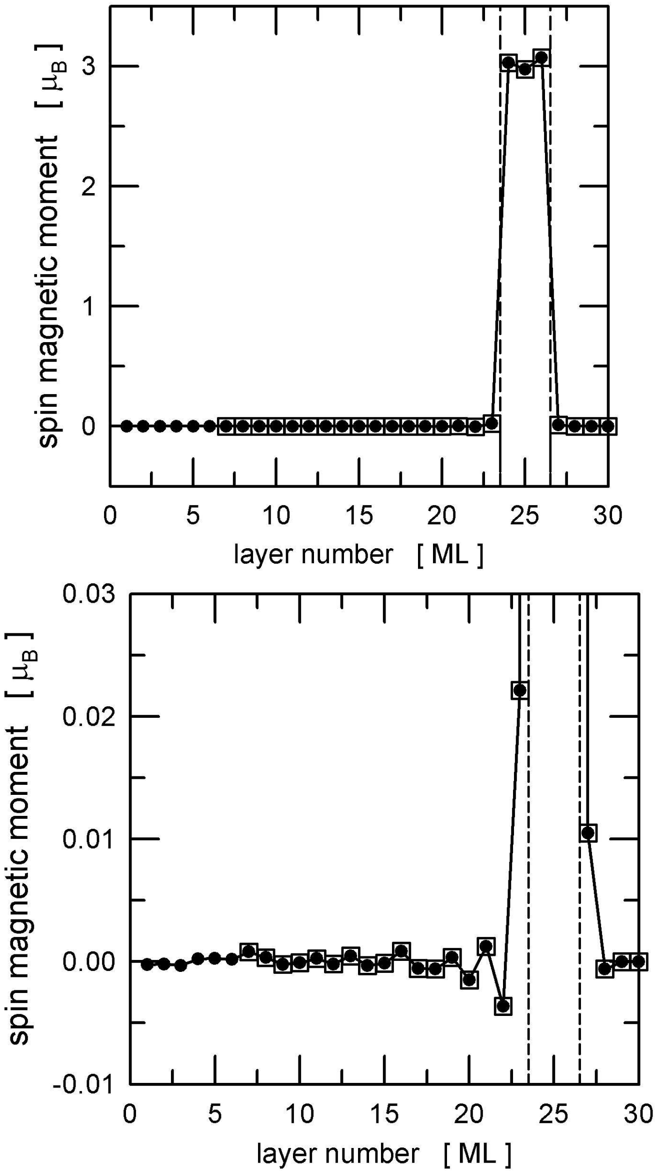

Figure 10.2: The SKKR calculated layer-resolved spin magnetic moments in Fe_3Au_{17}/Au(100) (white squares) and Fe_3Au_{23}/Au(100) (black circles) are approximately the same. The oscillation of the magnetic moments in Au goes deep inside the material, but, normally, its size can be neglected after 4 gold buffer layers.

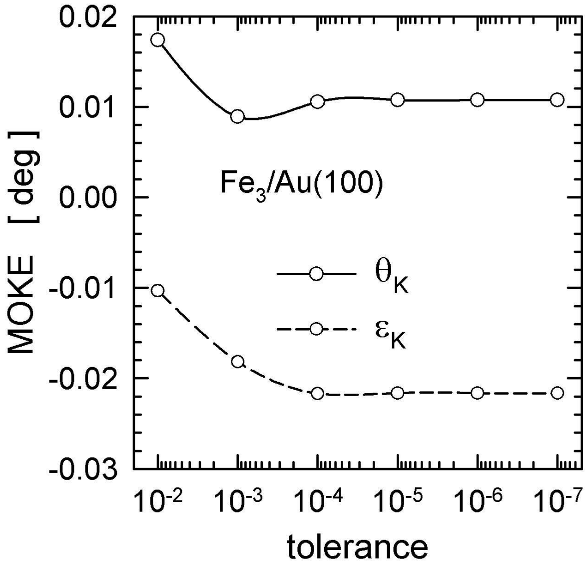

Figure 10.3: The convergence of the Kerr rotation angle, θ_K, and the Kerr ellipticity angle, ε_K, with respect to the tolerance in the conductivity tensor, $\sigma^{pq}_{\mu\nu}$. The largest changes occur between 10^{-2} and 10^{-4}, therefore, at least a value of the tolerance in $\sigma^{pq}_{\mu\nu}$ of 10^{-4} is required.

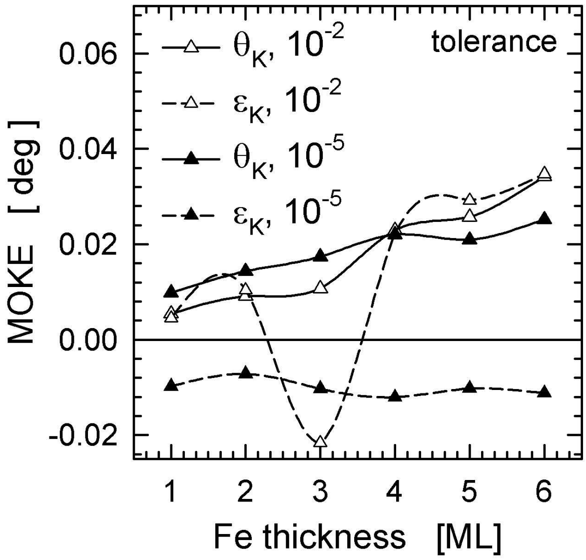

Figure 10.4: Results for values of the tolerance in the in E- and $\mathbf{k}$-integration of $\sigma^{pq}_{\mu\nu}$ of 10^{-2} and 10^{-5} are compared.

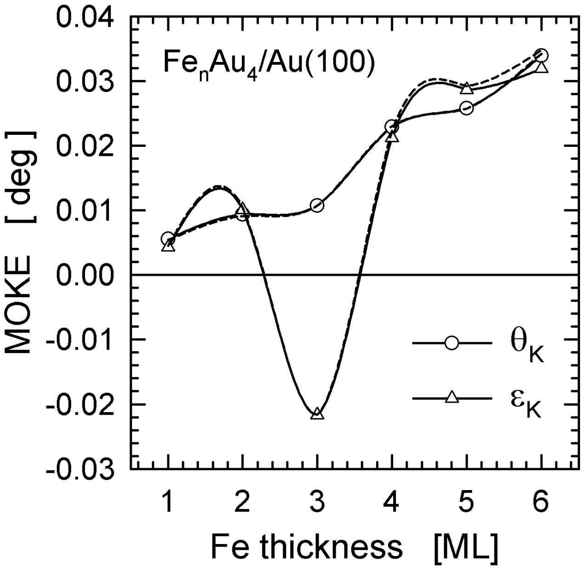

Figure 10.5: 4 buffer layers for all Fe thicknesses are included. The values are compared to the case of (according to Tab. 10.1) varying buffer thicknesses, indicated by the dashed lines.

Thus, if the computational resources are limited it is better to calculate with a moderate number of buffer layers than with a too high tolerance.

In the following the calculations are performed for the systems as given in Tab. 10.1 at a tolerance of 10^{-5}.

10.3 Comparison of the Fe permittivity to experiment

Kawagoe *et al.* [75] measured the ratio of the amplitudes of the complex reflectivities for p- and s-polarized light, $\rho(\lambda) = R_p/R_s$ (λ being the wave-length), in Fe/Au(100) and Fe/Ag(100). They varied the number of Fe layers from 2 to 20, used an optical wavelength regime of 270 – 760 nm (1.6 – 4.6 eV) and fixed the angle between the surface normal and the incident light to 57^0. By taking into account multiple reflections and using the optical constants of bulk Au they then deduced an effective dielectric constant ε of the upper Fe layer in Fe$_8$/Au(100) (But they do not speak about the off-diagonal element, maybe because it is by one to two orders of magnitude smaller than the diagonal ones are.) : at a photon energy of 3.8 eV they obtained -3.68 and 9.82 for the real (ε') and imaginary (ε'') part of ε, respectively. For the top Fe layer in Fe$_6$/Au(100), the largest system investigated in here, the *ab initio* calculated values of -5.26 and -2.06 for ε'_{xx} and ε'_{zz} as well as 5.09 and 4.45 for ε''_{xx} and ε''_{zz}. Not the best correspondence is to be expected because Fe$_6$/Au(100) and Fe$_8$/Au(100) can have different properties and it is also unknown how the transformation from the experimental $\rho(\lambda)$ was performed

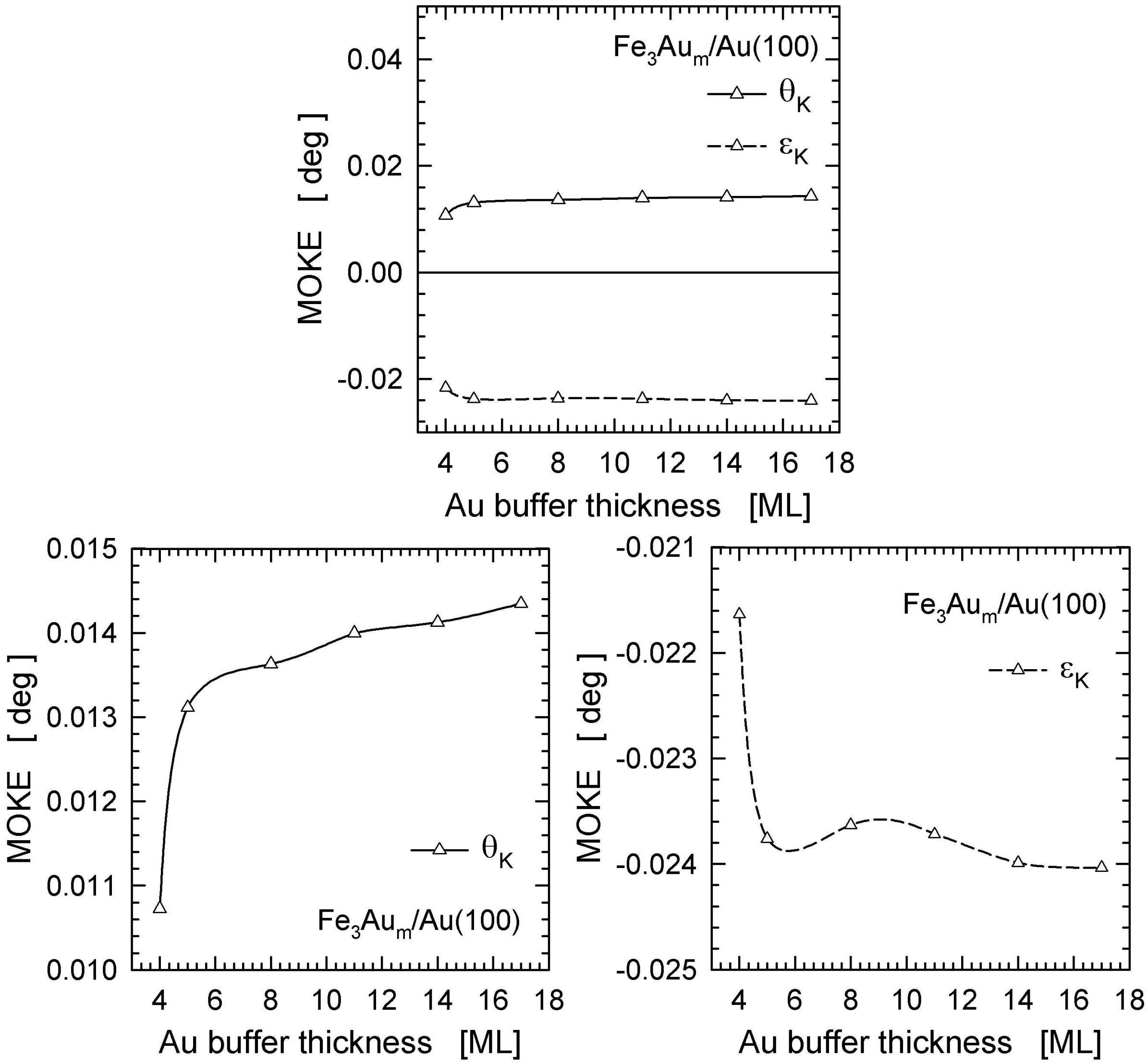

Figure 10.6: The convergence with respect to the Au buffer thickness for the example Fe$_3$/Au(100). Top: both Kerr angles together. Bottom: Detailed view of the Kerr angles plotted separately.

exactly. But, as is seen, the order of magnitude of the values is perfectly reproduced by the calculations.

10.4 MOKE for the ground-state orientations

Since – as already stated – in the SMOKE experiments by Liu and Bader [25] the polar and longitudinal Kerr intensities are given by the height of the hysteresis loops in the remanent state, the reorientation transition from a perpendicular to an in-plane orientation of the magnetization is manifested in a strong decrease of the Kerr intensity for normal incidence ($\beta = 0^0$) and a rather moderate increase of the Kerr intensity for grazing incidence ($\beta = 90^0$), see the upper part of Fig. 10.7. By considering the ground-state orientations of the magnetization resulting from magnetic anisotropy energy calculations the lower part of this figure shows the calculated Kerr rotation angles for two different angles of incidence, namely, for $\beta = 0^0$ and 70^0. Although Kerr angles and Kerr intensities cannot be directly related to each other, due to their linear dependence on the magnetization projected onto the direction of the incident light, it is not surprising at all that their respective dependence on the number of Fe layers is in good qualitative agreement. As can be immediately seen from Fig. 10.7, the calculated Kerr rotation angle for the system Fe$_n$/Au(100) in the magnetic ground state, remarkably well describes the magnetic reorientation transition in comparison with the experiments [25]: the perpendicular orientation of the magnetization is preferred below 3 ML, whereas above this Fe thickness the ground state is characterized by an in-plane orientation of the magnetization giving rise to exactly zero Kerr rotation angles for normal incidence. Since the present theoretical model does not include non-collinear magnetic arrangements, the reorientation transition [76, 77] (and consequently the calculated Kerr rotation angles) is not as smooth as in the experiment. In the case of oblique incidence (say for $\beta = 70^0$) non-vanishing Kerr rotation angles are obtained for both normal-to-plane ($n \leq 3$) and in-plane ($n > 4$) ground-state magnetization and the reorientation transition appears as a drop in θ_K.

10.5 Oblique incidence and arbitrary magnetization

10.5.1 MOKE for oblique incidence

Fig. 10.8 shows the theoretical Kerr rotation angles θ_K and ellipticity angles ε_K for the magnetic ground state of Fe$_n$/Au(100). The light is at oblique incidence and p-polarized. With the exception of grazing incidence, $\beta = 90^0$, all curves have the same structure as the theoretical results in Fig. 10.7, i.e. growing Kerr angles until $n = 3$ and – as a consequence of the reorientation transition – considerably decrease for $n = 4$.

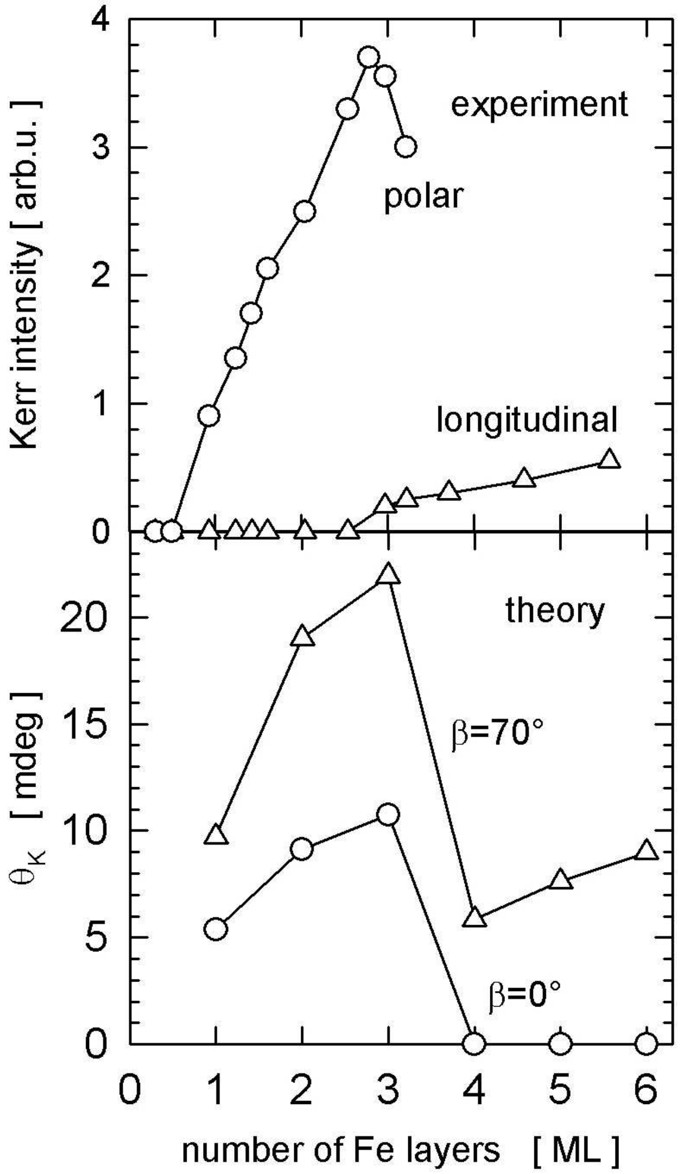

Figure 10.7: Top: SMOKE experiments by Liu and Bader [25]. Circles denote the measured data for the polar, whereas triangles for the longitudinal Kerr set-up. Bottom: calculated values of the Kerr rotation angle θ_K in the case of p-polarized incident light and for the magnetic ground state of Fe_n/Au(100). Circles mark the theoretical results for a normal incidence ($\beta = 0^0$) and triangles for an incidence of $\beta = 70^0$, see also Fig. 10.1.

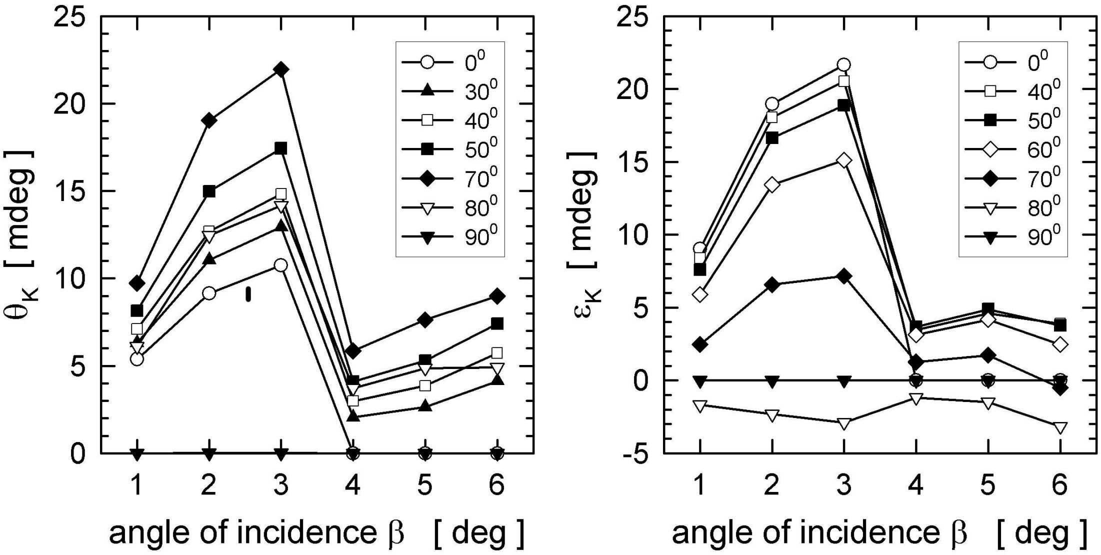

Figure 10.8: Calculated Kerr rotation (left) and ellipticity (right) angles for different angles of incidence, see Fig. 10.1, for the corresponding magnetic ground state of Fe$_n$/Au(100).

It is rewarding to analyze the Kerr angles with respect to the angle of incidence β for all film thicknesses which is done in Fig. 10.9. As it can be seen, two regimes of $\theta_K(\beta)$ and $\varepsilon_K(\beta)$ values can be distinguished: one for polar geometry ($n \leq 3$, $\alpha = 0^0$) where for $\beta = 0$ θ_K and ε_K are finite and one for longitudinal geometry ($n > 4$, $\alpha = 90^0$) with vanishing θ_K and ε_K for $\beta = 0$.

Independent of the Fe thickness the Kerr rotation angle for oblique incidence increases until $\beta = 70^0$, where a maximum of θ_K is reached; increasing the incidence angle β beyond 70^0 causes a continuous decrease of the Kerr rotation angle. Also ε_K shows a quite complicated dependence on β.

Maybe for the P-MOKE ($n \leq 3$) one has expected the largest effect for normal incidence, but, as is known from experiment [39] and from the approximative two-media formula [37, 36], the maximum is at an angle of incidence between 0^0 and 90^0. In here, the crucial point is that this dependence was mapped by means of an ab-initio method and the 2×2-matrix technique.

10.5.1.1 2×2-matrix technique versus the two-media approach

The two-media approach is used as a tool to get a better understanding of what happens in the exact but not easy to understand 2×2-matrix technique. The dependence on the angle of incidence β is analyzed for Fe$_3$/Au(100) (out-of-plane magnetization, polar geometry) and Fe$_6$/Au(100) (in-plane magnetization, longitudinal geometry) magnetization which is plotted in Figs. 10.10 and 10.11. The exact ab-initio data is compared to the simple

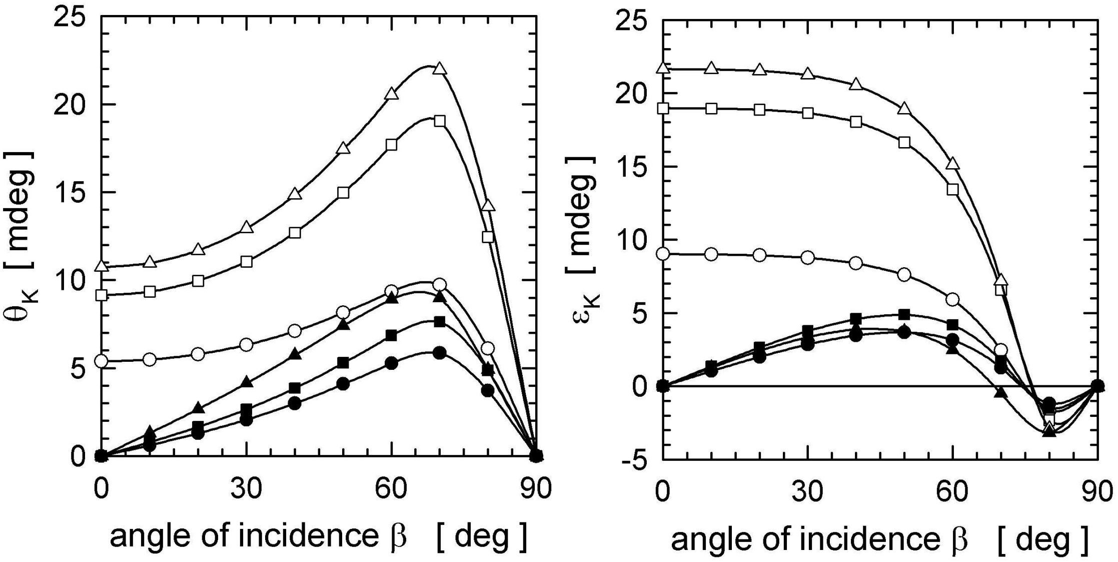

Figure 10.9: Calculated Kerr rotation (left) and ellipticity (right) angles as a function of the angle of incidence β and for different thicknesses of Fe films on Au(100). Open circles, squares and triangles refer to 1, 2 and 3, full circles, squares and triangles to 4, 5 and 6 ML of Fe on the top of Au(100).

two-media model. The Kerr rotation and Kerr ellipticity angles of Fe/Au(100), θ_K and ε_K, have been fitted separately with the P-MOKE two-media formula (3.80) and with the L-MOKE two-media formula (3.89). Additionally, a three-media formula proposed in Ref. [37] is used in order to fit the L-MOKE data.

The *ab-initio* values Fe$_3$/Au(100), see Fig. 10.10, are fitted with the two-media formula with the parameters ε_{xy} = 0.0015 + 0.002i and n = 1.1 + 5i for the Kerr rotation and ε_{xy} = 0.004 + 0.0015i and n = 1.5 + 5.8i for the Kerr ellipticity.

The *ab-initio* Kerr rotation of Fe$_6$/Au(100), see Fig. 10.11, is fitted in the two-media approach with ε_{xy} = 0.0004 + 0,005i and n = 1.1 + 5i and in the three-media approach with ε_{xy} = 0.0004 + 0,005i, n_1 = 1.4 + 4.9, and $n_2 = 1.9 + 4i$. The two-media values for the Kerr ellipticity are ε_{xy} = 0.0002 + 0.009i and n = 1.3 + 5.1i and the three-media values are ε_{xy} = 0.0004 + 0.005i, n_1 = 1.4 + 4.9i, and 1.2 + 6Ii.

10.5.2 Variation of the magnetization angle

For the particular case of Fe$_4$/Au(100) the Kerr angles are displayed in Fig. 10.12 for normal incidence ($\beta = 0^0$) and different orientations of the magnetization, $0 \leq \alpha \leq 90^0$. As can be seen from this figure both $\theta_K(\alpha)$ and $\varepsilon_K(\alpha)$ show an almost perfect $\cos(\alpha)$ dependence. This finding supports the experimentally known fact that for normal incidence the Kerr rotation angle is direct proportional to the normal component of the magnetization.

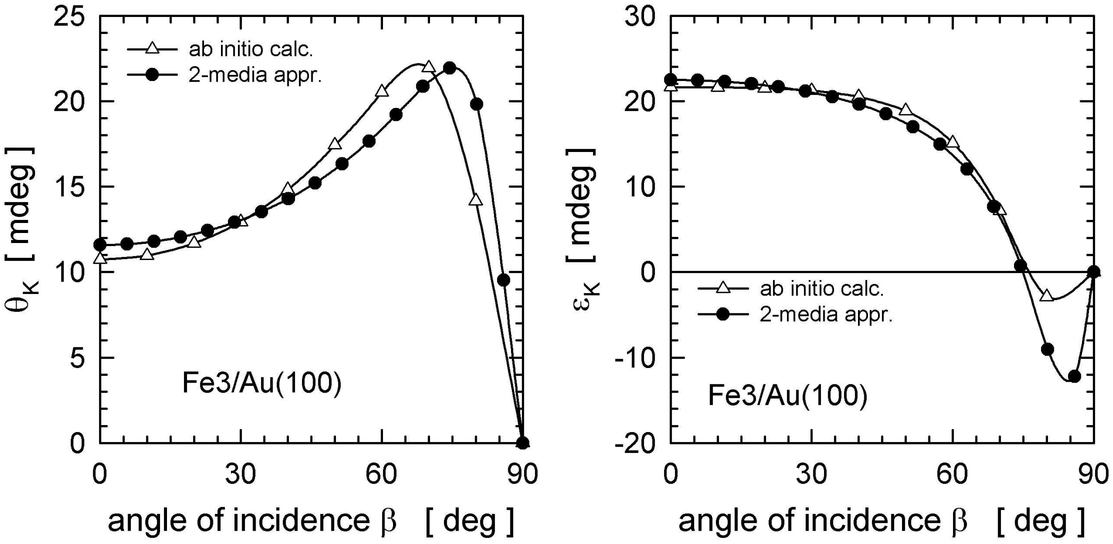

Figure 10.10: P-MOKE in Fe_3/Au(100).

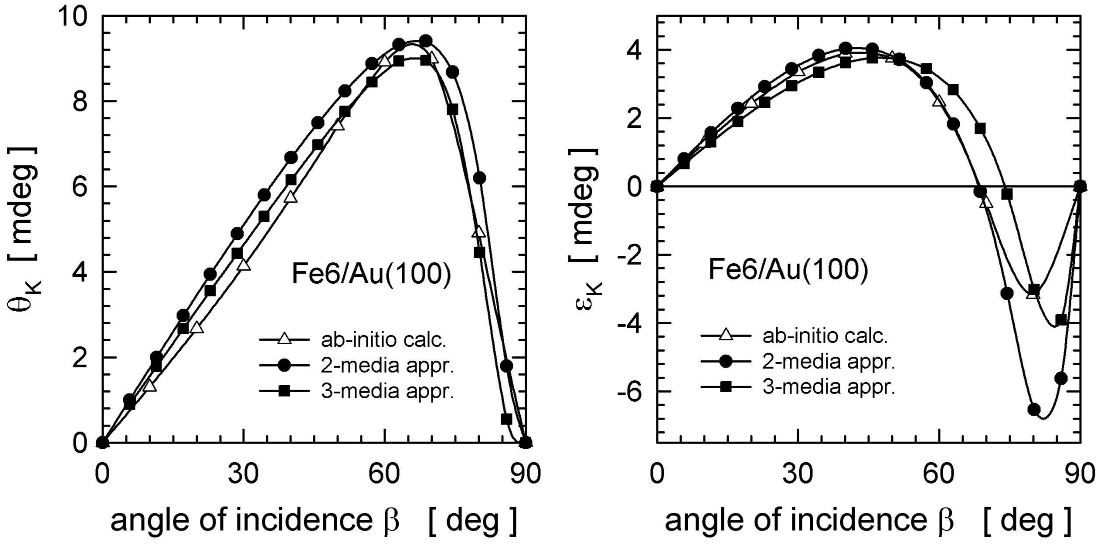

Figure 10.11: L-MOKE in Fe_6/Au(100).

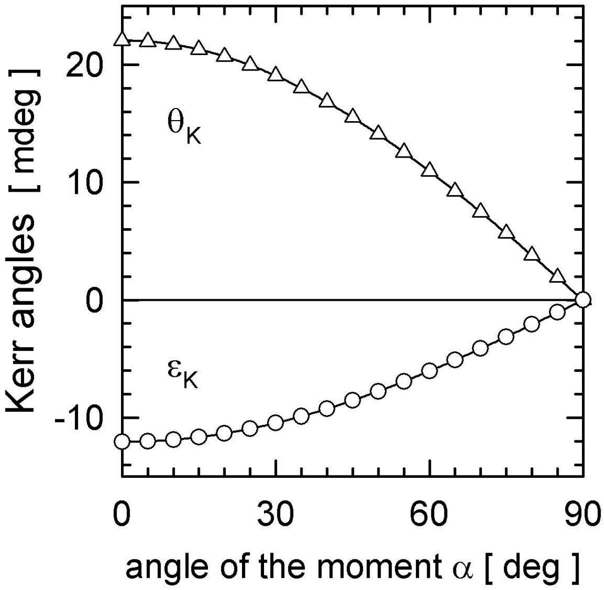

Figure 10.12: Calculated Kerr angles in the case of normal incidence for Fe$_4$/Au(100) as a function of the angle α , see Fig. 10.1.

10.6 Kerr angles versus quantities accessible by the experiment

10.6.1 Magnetic anisotropy energy

For the case of normal incidence Fig. 10.13 offers an interesting view of the Kerr angles, $\theta_K(\alpha)$ and $\varepsilon_K(\alpha)$, since in this figure each entry refers to a particular value of α, the abscissa being the anisotropy energy $E_a(\alpha)$. Obviously points along the ordinate ($E_a = 0$) correspond to $\alpha = 90^0$, while those along the abscissa belong to $\alpha = 0^0$. For $n \leq 3$ all curves fall into the regime of positive anisotropy energies (perpendicular orientation of the magnetization), while those for $n \geq 4$ refer to that of negative anisotropy energies (in-plane orientation). The reorientation transition is thus particularly clearly visualized.

10.6.1.1 External magnetic field

The paths shown in Fig. 10.13 can, in principle, be accessed experimentally if continuous reorientation transitions are induced by applying external magnetic fields in appropriate directions.

10.6.1.2 Perpendicular magnetic ground-state

Fig. 10.14 describes the effect of an in-plane applied external magnetic field $\mathbf{H}$ on a system exhibiting a perpendicular magnetic ground-state. As the field is switched on, the magneto-static force (see Appendix E) acts on the magnetic moment $\mathbf{M}$ which tries to

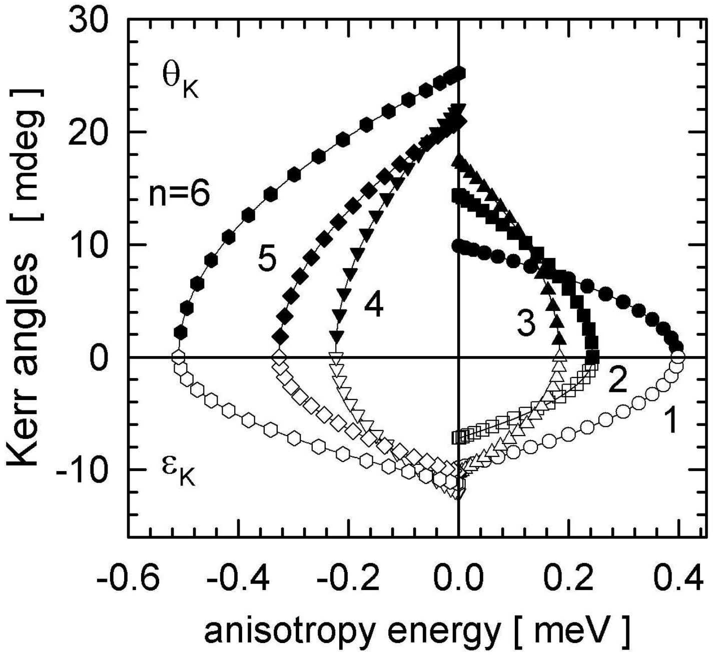

Figure 10.13: Calculated Kerr angles displayed as a function of the magnetic anisotropy energy for different thicknesses of the Fe film on Au(100). The data for this figure were obtained by varying the angle of magnetization α while the angle of incidence is fixed to $\beta = 0^0$, see Fig. 10.1.

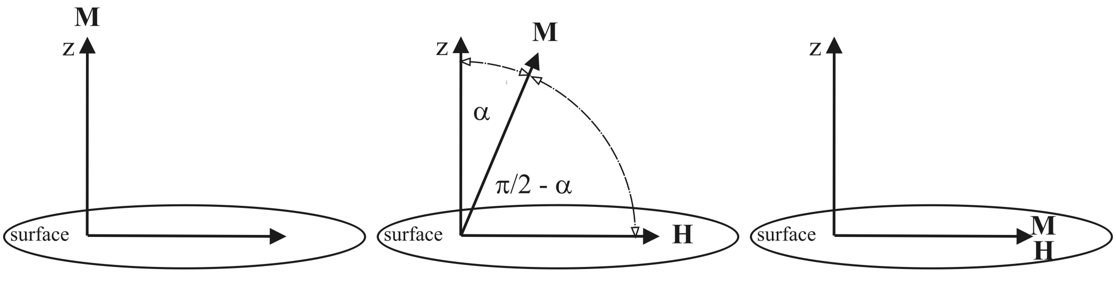

Figure 10.14: Perpendicular magnetic ground-state. In the left plot, $\mathbf{H} = 0$, in the middle $0 < \mathbf{H} < \mathbf{H}_s$, and in the right $\mathbf{H} \geq \mathbf{H}_s$, where $\mathbf{H}_s$ is the field where the needed for saturation.

align it in-plane, $\mathbf{f} \propto -\nabla\,(\mathbf{M}\cdot\mathbf{H})$. Contrary to the magneto-static force is the anisotropy. In equilibrium, the sum of both contributions to the energy of the system is minimized.

Assuming a second order anisotropy, the energy due to it is given by $E_a = -K\cos^2(\alpha)$, where K is the uniaxial anisotropy constant which is the energy difference between in-plane and perpendicular magnetization, $K = E_{\|} - E_{\perp}$, which, in the case of a perpendicular magnetic ground-state, is positive. The magneto-static energy density (see equation (E.4)) involves the inner product $\mathbf{M}\cdot\mathbf{H}$ yielding (see Fig. 10.14) $MH\cos(\frac{\pi}{2}-\alpha)$,[a.]

$$\begin{aligned}\Delta E(\alpha) &= -K\cos^2(\alpha) - MH\cos(\frac{\pi}{2}-\alpha)\\ &= -K + K\sin^2(\alpha) - MH\sin(\alpha),\\ \Delta E(y) &= -K + Ky^2 - MHy\end{aligned}$$

where $y = \sin(\alpha)$. The minimum in the energy with respect to y is found by differentiation

$$\mathrm{d}\Delta E(y)/\mathrm{d}y = 2Ky - MH = 0,$$

yielding

$$y = \sin(\alpha) = \frac{MH}{2K} = \frac{H}{H_0}, \tag{10.1}$$

where $H_0 = 2K/M$ and M is the (total) magnetic moment of the ferromagnetic system. This implies that for the case of $K > 0$ (perpendicular anisotropy) and a longitudinal magnetic field the equilibrium orientations are given by,

$$\alpha = \begin{cases} 90^0 & \text{for} \quad H > H_0 \\ \arcsin(H/H_0) & \text{for} \quad -H_0 < H \le H_0 \\ -90^0 & \text{for} \quad H \le -H_0 \end{cases} . \tag{10.2}$$

As was found out in the present study, for normal incidence the Kerr effect's dependence on the magnetization orientation is described by $\theta_K(\alpha) \approx \theta_{K0}\cos(\alpha)$ where θ_{K0} is the Kerr rotation for perpendicular magnetization, $\theta_K(\alpha = 0)$. Analogously the Kerr ellipticity is described by $\varepsilon_K(\alpha) = \varepsilon_{K0}\cos(\alpha)$ where $\varepsilon_{K0} = \varepsilon_K(\alpha = 0)$. The angle α is the equilibrium angle of the magnetization for a given external field, $\cos^2(\alpha) = 1-\sin^2(\alpha) = 1-(H/H_0)^2$, thus

$$\theta_K(\alpha) \approx \theta_{K0}\sqrt{1-\left(\frac{H}{H_0}\right)^2} \quad , \quad \varepsilon_K(\alpha) \approx \varepsilon_{K0}\sqrt{1-\left(\frac{H}{H_0}\right)^2} \quad . \tag{10.3}$$

10.6.2 In-plane magnetic ground-state

Analogously to Sec. 10.6.1.2, in the case of an in-plane magnetic ground-state, see Fig. 10.15, the Kerr effect's dependence on the external field is derived. The energy to be minimized

---

[a.] The factor 1/2 in the magneto-static energy is dropped because it is only a constant.

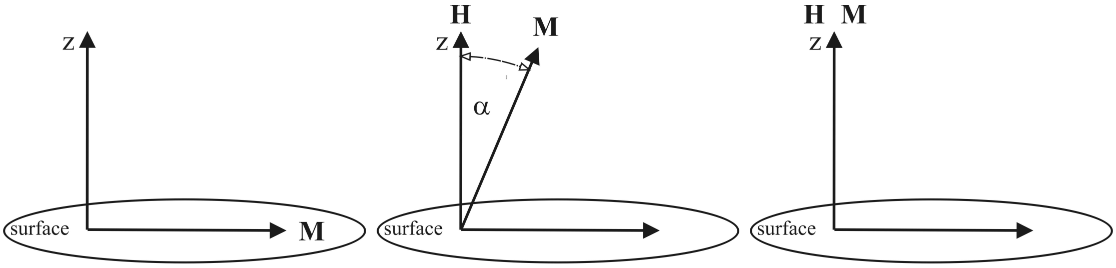

Figure 10.15: In-plane magnetic ground-state. See Fig. 10.14.

is given by

$$\Delta E(\alpha) = -K\cos^2(\alpha) - M \cdot H\cos(\alpha) \tag{10.4}$$

$$\Delta E(x) = -Kx^2 - MHx \tag{10.5}$$

where $x = \cos(\alpha)$. The differentiation with respect to x

$$\mathrm{d}\Delta E(x)/\mathrm{d}x = -2Kx - MH = 0$$

yields the minimum with respect to x,

$$x = \cos(\alpha) = -\frac{MH}{2K} = \frac{H}{H_0} \tag{10.6}$$

where $H_0 = -2K/M$. In the case of an in-plane anisotropy ($K < 0$) a polar magnetic field has to applied in order to induce a continuous reorientation transition,

$$\alpha = \begin{cases} 0^0 & \text{for} \quad H > H_0 \\ \arccos(H/H_0) & \text{for} \quad -H_0 < H \leq H_0 \\ 180^0 & \text{for} \quad H \leq -H_0 \end{cases} . \tag{10.7}$$

The Kerr angles as a function of the applied field are then given by,

$$\theta_K(\alpha) \approx \theta_{K0}\frac{H}{H_0} \quad , \quad \varepsilon_K(\alpha) \approx \varepsilon_{K0}\frac{H}{H_0} \quad . \tag{10.8}$$

The data for the Kerr angles in Fig. 10.13 and Fig. 10.16 is the same, but in the latter it is depicted as a function of an external magnetic field, the size of which is obtained from the orientation of the magnetization by using either equation (10.2) ($n \leq 3$) or equation (10.7) ($n > 3$). It is sufficient to depict only the corresponding curves for $H > 0$.

It should be noted that the obtained values of $H_0^{\|}$ are typically by one order of magnitude larger than the experimentally measured coercive fields [25] which within the model used in here are equivalent to H_0.

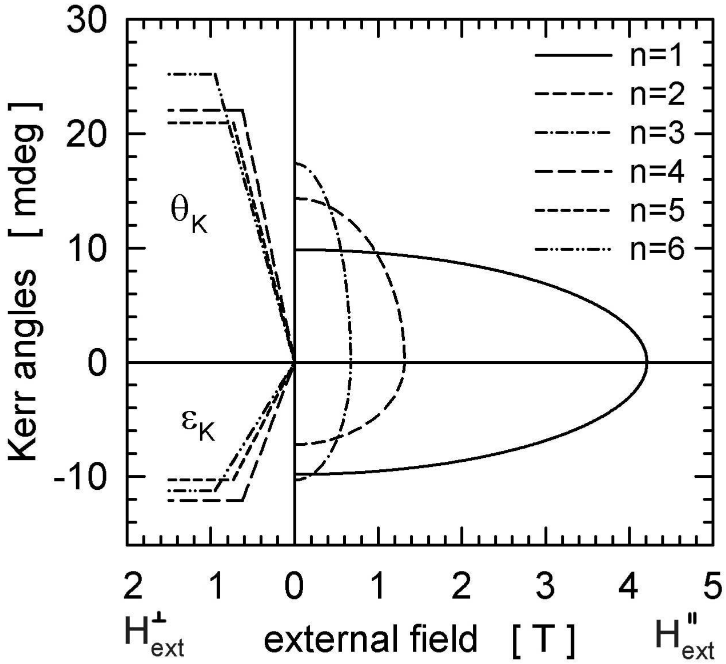

Figure 10.16: Calculated Kerr angles displayed as a function of a longitudinal ($H_{ext}^{\|}$, right part) and a polar ($H_{ext}^{\perp}$, left part) external magnetic field applied to Fe$_n$/Au(100) for $n \leq 3$ and $n > 4$, respectively. As in Fig. 10.13 the data for this figure was obtained by varying α and keeping the angle of incidence fixed to $\beta = 0^0$, see also Fig. 10.1.

10.6.2.1 The band energy difference

The Figs. 10.17 and 10.18 show the dependence of the band energy difference on the orientation of the magnetization and that the simple trigonometric behavior is a good approximation for Fe_n/Au(100). The behavior is equivalently described by

$$\begin{aligned}\Delta E_b(\alpha) &= E(\alpha) - E_{\|}\\ \Delta E_b(\alpha = 0^0) &= E(\perp) - E_{\|} = -K\\ \Delta E_b(\alpha = 90^0) &= E(\|) - E_{\|} = 0\end{aligned}$$

yielding

$$\Delta E_b(\alpha) \approx -K\cos^2\alpha \tag{10.9}$$

or by

$$\begin{aligned}\Delta E_b(\alpha) &= E(\alpha) - E_{\perp}\\ \Delta E_b(\alpha = 0^0) &= E(\perp) - E_{\perp} = 0\\ \Delta E_b(\alpha = 90^0) &= E(\|) - E_{\perp} = +K\end{aligned}$$

implying

$$\Delta E_b(\alpha) \approx +K\sin^2\alpha. \tag{10.10}$$

One description is obtained from the other by adding a constant (which does not affect the energy minimum),

$$K - K\cos^2\alpha = K(1-\cos^2\alpha) = K\sin^2\alpha. \tag{10.11}$$

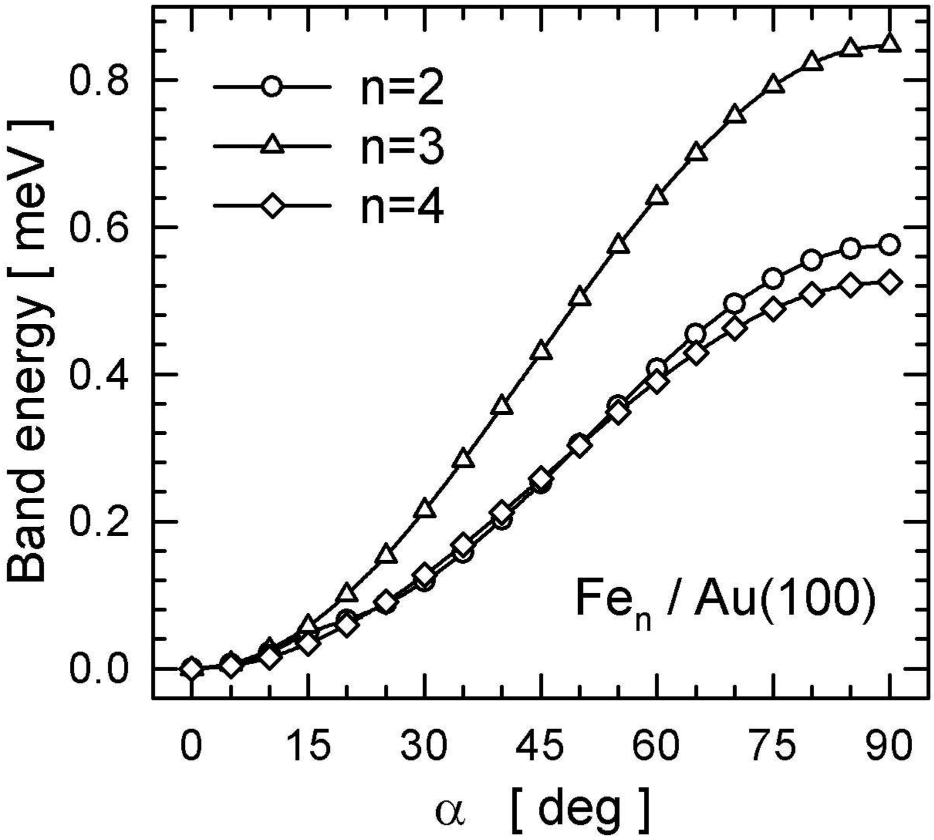

Figure 10.17: Dependence of the band energy difference defined by $\Delta E_b(\alpha) = E(\alpha) - E_\perp$ on the magnetization orientation.

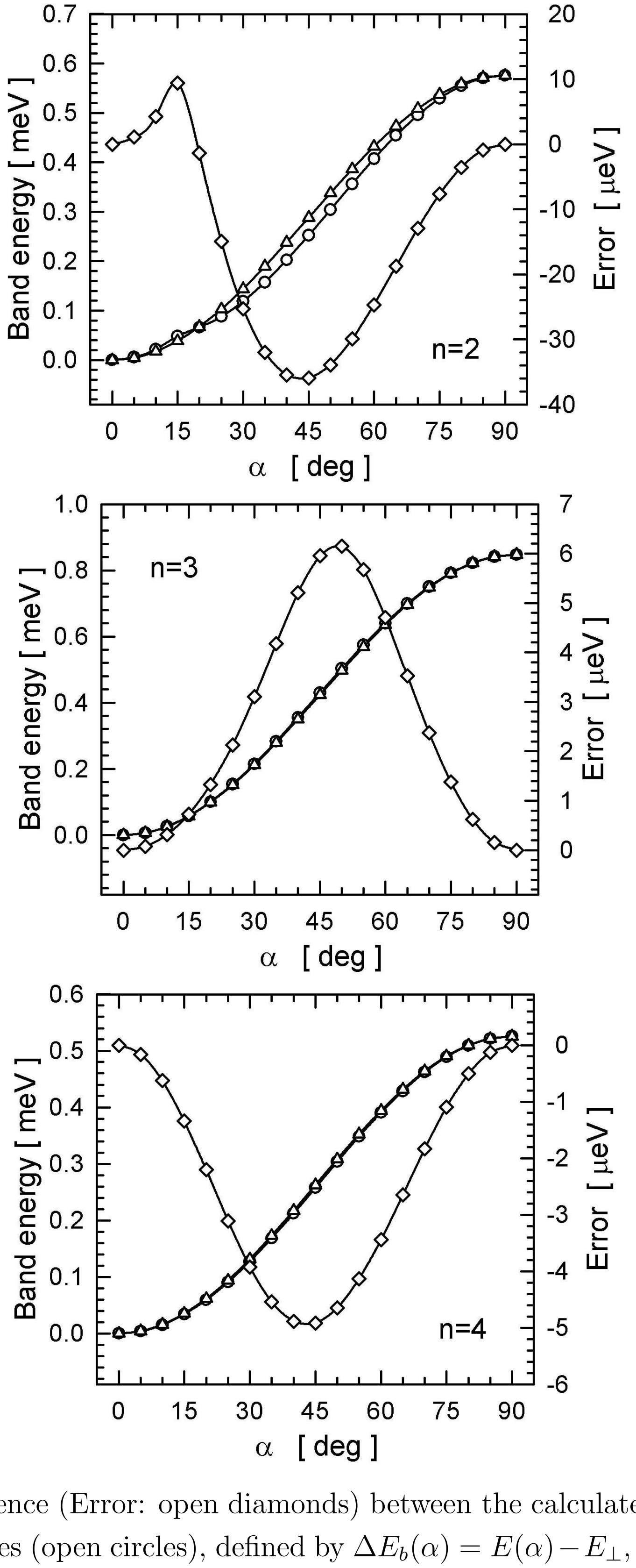

Figure 10.18: Difference (Error: open diamonds) between the calculated band energy differences (open circles), defined by $\Delta E_b(\alpha) = E(\alpha) - E_\perp$, and the estimation $\Delta E_b(\alpha) \approx +K \sin^2 \alpha$.

11 Inter-layer exchange coupling in Cu/Ni tri-layer systems

All calculations for $\mathrm{Fe}_n/\mathrm{Au}(100)$, $n = 1, ..., 6$, were performed as explained in Section 7, namely by considering three buffer layers of Cu to guarantee reliable matching to the semi-infinite Cu(100) substrate and at least three vacuum layers to join up to the semi-infinite vacuum. All systems investigated refer exactly to those studied theoretically and experimentally by Hammerling *et al.* [55]. We use linearly polarized light normal incidence at normal incidence with a photon wave length corresponding to a He-Ne laser, namely 633nm (1.96eV).

The spacer thickness of the $\mathrm{Cu}_4\mathrm{Ni}_8\mathrm{Cu}_n\mathrm{Ni}_9/\mathrm{Cu}(100)$ system is varied between two and ten mono-layers of Cu. For a free surface not only a sufficient number of vacuum layers has to be used but also so-called "buffer" layers to the semi-infinite substrate, and the total number of layers has to be an integral multiple of three [48, 63, 41]. Table 11.1 schematically shows the sequence of layers and the orientation of the magnetic moments for all investigated cases. In this table $\uparrow$, $\downarrow$ label the directions of the magnetization induced in the Cu layers, $\Uparrow$, $\Downarrow$ in the Ni layers and $\times$ indicates vacuum layers in the actually investigated systems $\mathrm{Vac}_m\mathrm{Cu}_4\mathrm{Ni}_8\mathrm{Cu}_n\mathrm{Ni}_9\mathrm{Cu}_3/\mathrm{Cu}(100)$, $m \geq 3$ and $2 \leq n \leq 10$. For $n = 10$ both configurations, the ferromagnetic and the anti-ferromagnetic one, are listed since this particular case will serve later on for a comparison of their magneto-optical properties. It should be mentioned that the magnetic configuration (orientation of the moments) resulted from the IEC calculations in Ref. [55]. As was shown there, the out-of-plane orientation of the moments in the Ni layers is a consequence of the lattice relaxation. Assuming that there is no distortion of the inter-layer distance in the Ni slabs as compared to fcc Cu, an in-plane orientation would be preferred. At present, however, this kind of layer relaxation cannot be taken into account in the conductivity calculations, the lattice spacing considered refers to a perfect fcc Cu bulk. In all conductivity calculations the orientation of the magnetization is assumed to be out-of-plane (z direction).

	number of spacer layers									
	2	3	4	5	6	7	8	9	10	
39									×	
38									×	
37									×	Vac
36						×	×	×	×	
35						×	×	×	×	
34						×	×	×	↓↑	
33			×	×	×	×	×	↑	↓↑	Cu_4
32			×	×	×	×	↓	↑	↓↑	
31			×	×	×	↑	↓	↑	↓↑	
30	×	×	×	×	↑	↑	↓	↑	⇓⇑	
29	×	×	×	↓	↑	↑	↓	⇑	⇓⇑	
28	×	×	↑	↓	↑	↑	⇓	⇑	⇓⇑	
27	×	↓	↑	↓	↑	⇑	⇓	⇑	⇓⇑	Ni_8
26	↑	↓	↑	↓	⇑	⇑	⇓	⇑	⇓⇑	
25	↑	↓	↑	⇓	⇑	⇑	⇓	⇑	⇓⇑	
24	↑	↓	⇑	⇓	⇑	⇑	⇓	⇑	⇓⇑	
23	↑	⇓	⇑	⇓	⇑	⇑	⇓	⇑	⇓⇑	
22	⇑	⇓	⇑	⇓	⇑	⇑	⇓	⇑	↓↑	
21	⇑	⇓	⇑	⇓	⇑	⇑	⇓	↑	↓↑	
20	⇑	⇓	⇑	⇓	⇑	⇑	↓	↑	↓↑	
19	⇑	⇓	⇑	⇓	⇑	↑	↓	↑	↓↑	
18	⇑	⇓	⇑	⇓	↑	↑	↓	↑	↓↑	
17	⇑	⇓	⇑	↓	↑	↑	↓	↑	↑	Cu_n
16	⇑	⇓	↑	↓	↑	↑	↑	↑	↑	
15	⇑	↓	↑	↓	↑	↑	↑	↑	↑	
14	↑	↑	↑	↑	↑	↑	↑	↑	↑	
13	↑	↑	↑	↑	↑	↑	↑	↑	↑	
12	⇑	⇑	⇑	⇑	⇑	⇑	⇑	⇑	⇑	
⋮	⇑	⇑	⇑	⇑	⇑	⇑	⇑	⇑	⇑	Ni_9
4	⇑	⇑	⇑	⇑	⇑	⇑	⇑	⇑	⇑	
3	↑	↑	↑	↑	↑	↑	↑	↑	↑	
2	↑	↑	↑	↑	↑	↑	↑	↑	↑	Cu_3
1	↑	↑	↑	↑	↑	↑	↑	↑	↑	
⋮	Cu bulk									

Table 11.1: Magnetic configurations.

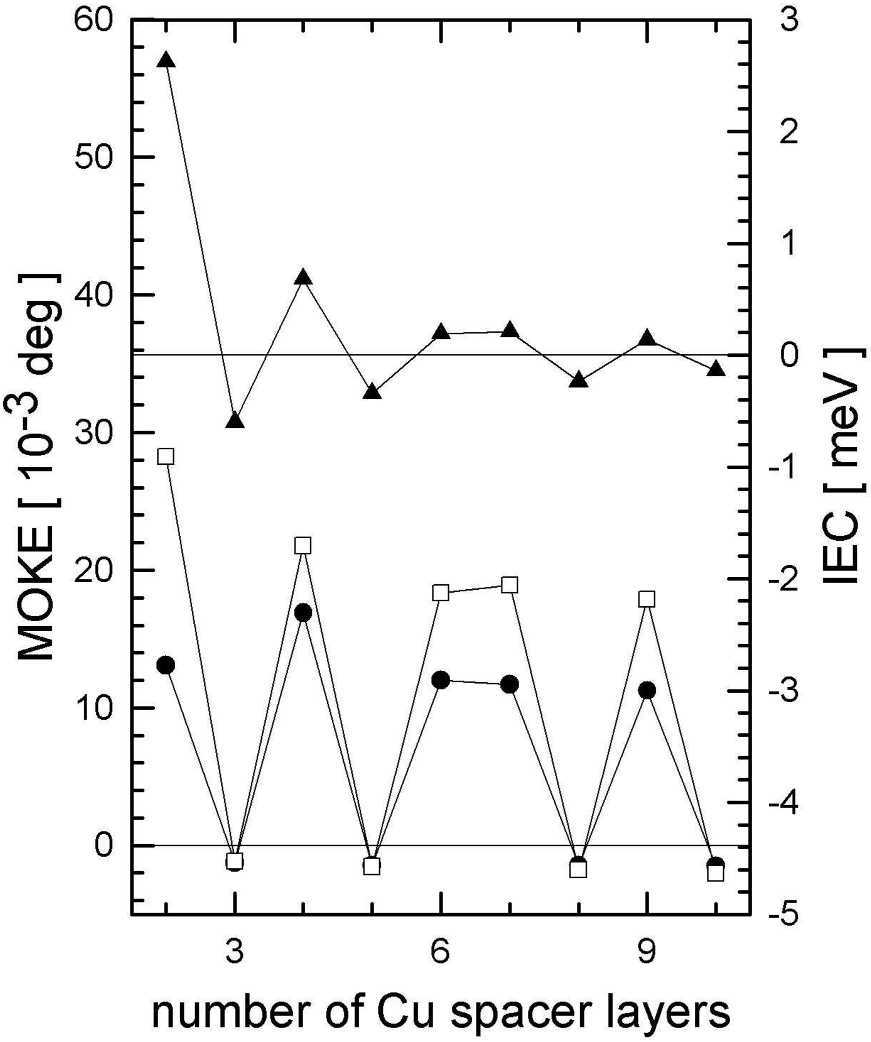

Figure 11.1: Comparison between IEC and MOKE for $Cu_4Ni_8Cu_nNi_9/Cu(100)$ with respect to the number of Cu spacer layers. Triangles denote the theoretical IEC results of Ref. [55], circles and squares the calculated Kerr angles θ_K and ε_K, respectively.

11.1 Discussion

11.1.1 Kerr angles and inter-layer exchange coupling

In Fig. 11.1 a comparison between the calculated IEC of Ref. [55] and the calculated Kerr angles is displayed versus the number of spacer layers (ML). It should be pointed out that the physical origin of the IEC and that of the MOKE is different and cannot be related directly. The stronger damped oscillation of the IEC values are thus not in contradiction with the moderate damping of the MOKE data. As can be seen the agreement of the oscillation pattern between the MOKE results and the IEC calculations is perfect. At a first glance this seems to confirm the rule of thumb that the Kerr effect is proportional to the total magnetic moment, see Ref. [13], since in a FM configuration the total magnetic moment has to be larger than in an AFM configuration.

11.1.2 Kerr angles and the total magnetic moment

The total moment is defined as the sum over all layer-resolved magnetic moments including not only the Ni moments but also the very weak moments in the spacer and buffer layers,

$$m = \sum_{p=1}^{N} m_p \,, \tag{11.1}$$

where N is the total number of layers considered. m does not change sign (z being the quantization axis) as suggested by the variation of the MOKE data with respect to the number of spacer layers, see Fig. 11.1, because 8 Ni layers were considered to change sign while the magnetization of the 9 Ni layers is kept constant. This fact cannot be used to explain the negative MO Kerr angles.

simply because always contribute less than and the Cu layers contribute very little. This in turn implies to consider first the magneto-optical properties of $\mathrm{Cu_4Ni_8Cu}_n\mathrm{Ni_9/Cu(100)}$ before returning to the question of a possible relation to magnetic moments.

11.1.2.1 Layer-resolved permittivity for anti-parallel and parallel coupling

In order to sort out the difference between a FM and an AFM configuration one particular case, namely for ten spacer layers was considered. As can be seen from Fig. 11.2 the layer-resolved diagonal elements $\varepsilon^p_{xx} = \varepsilon^p_{yy}$ and ε^p_{zz}, do not show any peculiar differences between the two types of magnetic configurations, whereas obviously the layer-resolved off-diagonal elements ε^p_{xy} in Fig. 11.3 are of opposite signs in the oppositely polarized Ni-slabs. It is interesting to note that essentially the paramagnetic Cu spacer layers become polarized. Polarization means that the complex off-diagonal permittivity tensor elements, $\varepsilon^p_{yx} = -\varepsilon^p_{xy}$, shown in Fig. 11.3, do not vanish in the Cu spacer layers.

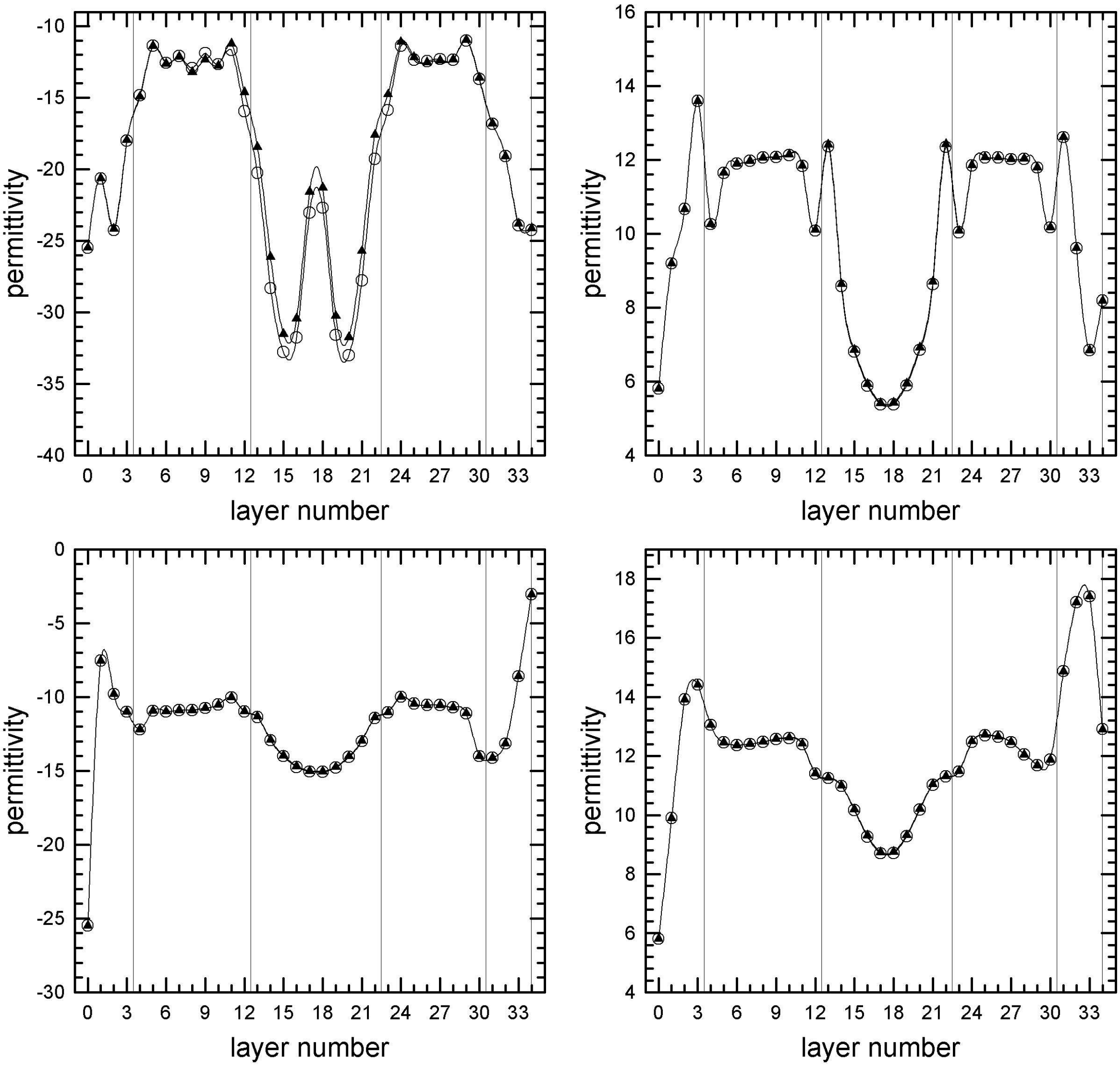

Figure 11.2: Comparison of the AFM (triangles) and FM (circles) layer-resolved complex permittivity Re(ε_{xx}) (upper left), Im(ε_{xx}) (upper right), Re(ε_{zz}) (lower left), and Im(ε_{zz}) (lower right) for $Cu_4Ni_8Cu_{10}Ni_9$/Cu(100).

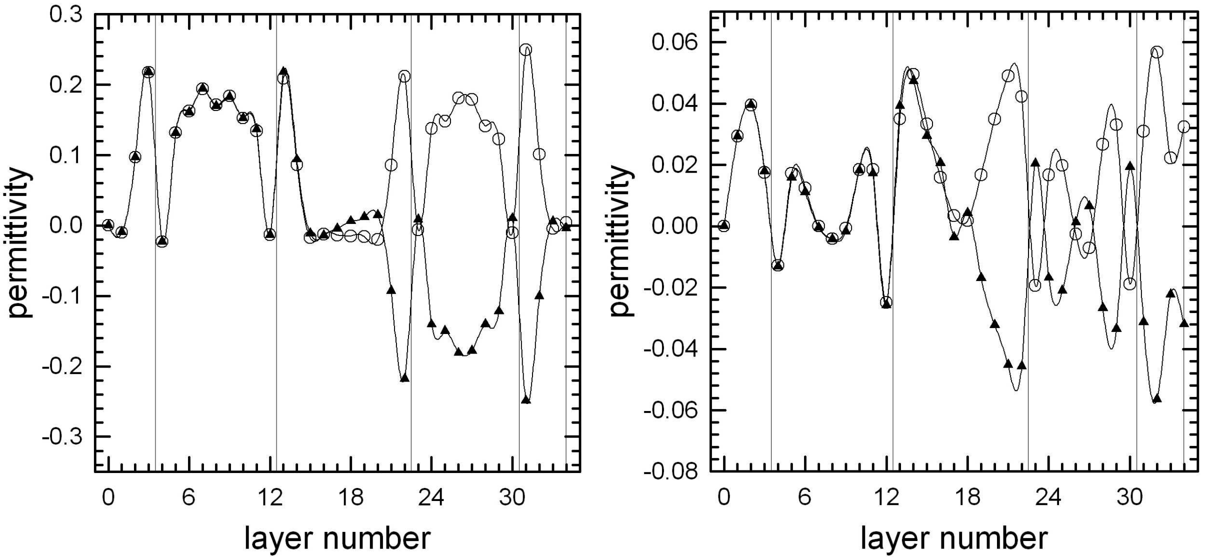

Figure 11.3: Comparison of the AFM (triangles) and FM (circles) layer-resolved complex permittivity $\mathrm{Re}(\varepsilon_{xy})$ (left) and $\mathrm{Im}(\varepsilon_{xy})$ (right) for $\mathrm{Cu_4Ni_8Cu_{10}Ni_9/Cu(100)}$.

The layer-resolved permittivities ε^{p}_{ij}, $i, j \in \{x, y, z\}$, are the only input needed in order to calculate the Kerr angles and ellipticities in terms of the 2×2 matrix technique.[43, 45, 53] This implies that ε^{p}_{xy} is the only quantity in the description of MOKE that appears with an opposite sign in an AFM as compared to a FM configuration.

11.1.2.2 Penetration depth

Neglecting multiple reflections and interferences, it is simple to analyze an incident wave reflected at a particular layer p. Assuming no further reflections, the light travels back to the surface with a reduced amplitude A'. The space-like part of a plane wave travelling in z direction is given by $A \exp[ikz]$. The wave number k is complex, thus the real part is responsible for the oscillation and the imaginary part for the absorption of the wave. Using layer-resolved complex wave numbers the damped amplitude A'_p can be obtained as

$$A'_p = A_0 \prod_{q=0}^{N-p+1} \prod_{q=N-p+1}^{0} \exp\left[i\,\mathrm{Im}(k_{N-q}) \cdot d_{N-q}\right] = A_0 \prod_{q=0}^{N-p+1} \exp\left[2i\,\mathrm{Im}(k_{N-q}) \cdot d_{N-q}\right] \quad . \tag{11.2}$$

If the penetration depth is defined as the thickness at which the amplitude of the incident wave is reduced to A_0/e, where e is Euler's constant, the number of layers s needed for this purpose has to be determined from the below relation

$$\sum_{q=0\in\{1,\ldots,s\}} \mathrm{Im}(k_{N-q}) \cdot d_{N-q} = -1 \quad . \tag{11.3}$$

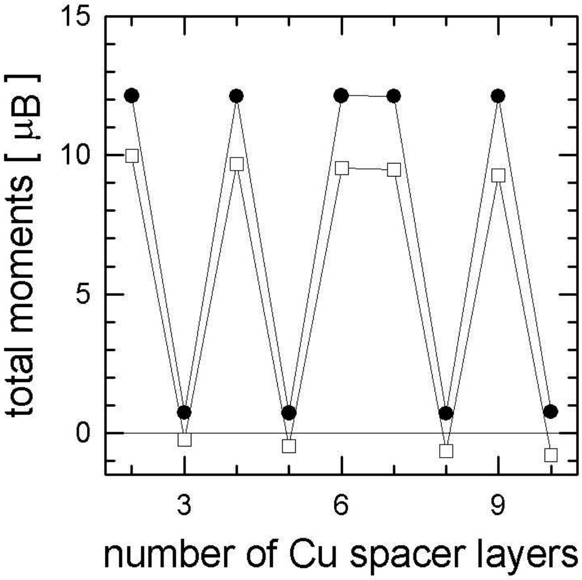

Figure 11.4: Total (undamped, circles) and effective (damped, squares) total magnetic moments in $\mathrm{Cu_4Ni_8Cu_{10}Ni_9/Cu(100)}$ versus the number of Cu spacer layers.

It should be noted that for the penetration depth only light travelling in direction of the substrate is considered, therefore in Equation (11.3) the factor 2 is dropped. The bulk-value of the refractive index of pure Cu, e.g., leads to a penetration depth of $s = 68.5$ layers.

11.1.2.3 Effective magnetic moments

It is assumed that the magneto-optic Kerr effect is related to a weighted sum of the layer-resolved magnetic moments (referred to as total effective magnetic moment) with weighting factors being the damping factors of a wave reflected at a layer p. Then the total effective (i.e. damped) magnetic moment is given by

$$m' = \sum_{p=1}^{N} m'_p \ , \quad m'_p = \frac{A'_p}{A_0} \cdot m_p \quad . \tag{11.4}$$

The total damped magnetic moment m', see Fig. 11.4, turns out to be negative for an AFM configuration which, as summarized in Table 11.2, is then consistent with the theoretical MOKE results obtained using the 2×2 matrix technique [43, 45, 53]. In Fig. 11.5 m_p and m'_p in $\mathrm{Cu_4Ni_8Cu_{10}Ni_9/Cu(100)}$ are shown as a function of the layer index p. In this figure, in which the Cu substrate is to the left, vacuum to the right, and the damping factor is displayed in terms of circles, one can see that especially in the Ni slab closer to the substrate the damped magnetic moments are considerably smaller than the undamped ones.

	FM	AFM
θ_K, ϵ_K	> 0	< 0
m'	> 0	< 0
m	> 0	> 0

Table 11.2: Comparison of theoretical MOKE results as given by θ_K and ϵ_K with damped (m') and undamped (m) total magnetic moments.

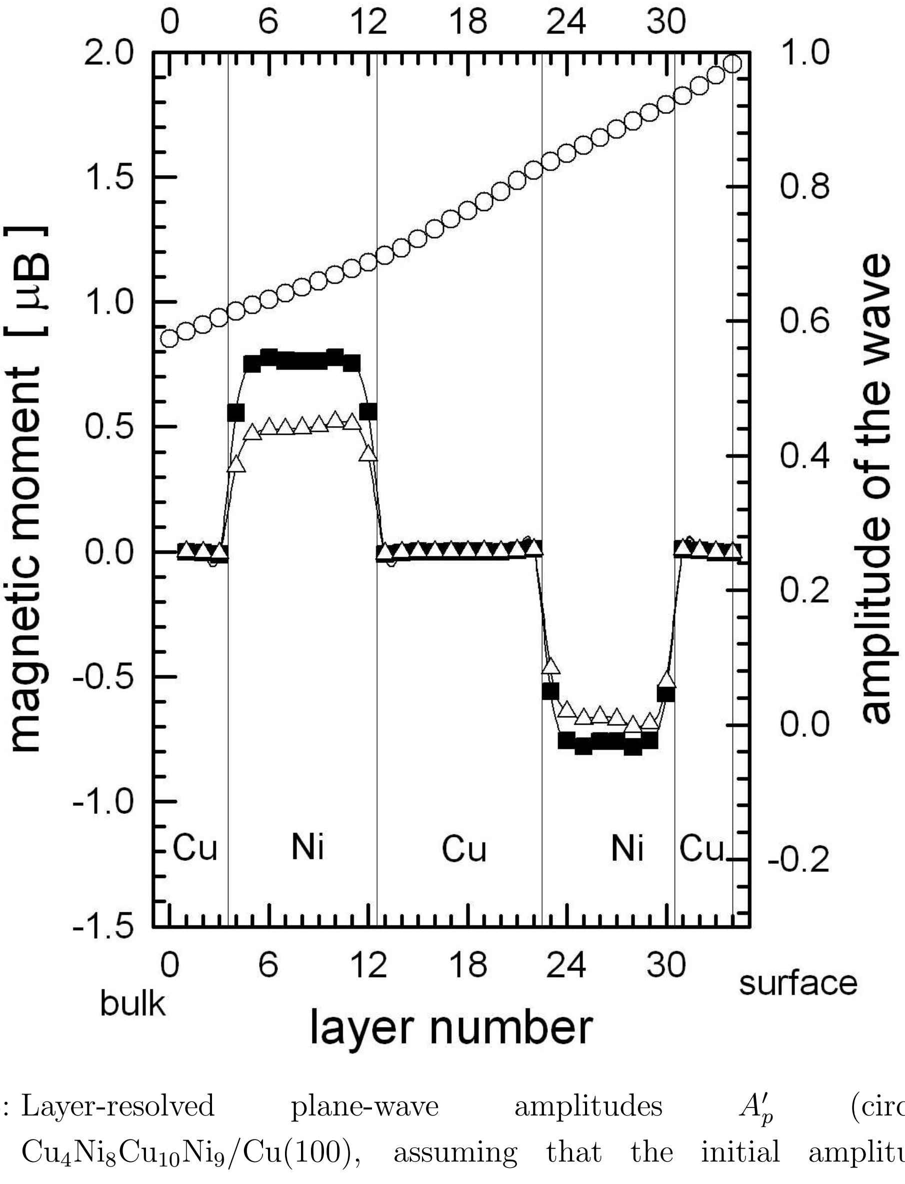

Figure 11.5: Layer-resolved plane-wave amplitudes A'_p (circles) in $Cu_4Ni_8Cu_{10}Ni_9/Cu(100)$, assuming that the initial amplitude A_0 is unity. Squares and triangles refer in turn to layer-resolved undamped and damped magnetic moments.

It should be noted that empirical information depth profiles were already introduced [78, 79] in the early nineties by defining so-called sensitivity functions. Thus it appears at a first glance that in Equation (11.4) only a well-known recipe is applied. This, however, is not the case, since the layer-resolved magnetic moments m_p in this equation are calculated by means of an ab-initio approach and the amplitudes A'_p simply mimic a (possible) exponential decay. The weights $A'_p/\ A_0$ are only introduced in order to show that in Kerr measurements not the true total magnetic moment is mapped but a quantity that reflects a rather complicated thickness dependence.

12 Future material for perpendicular magneto-optic recording: Co/Pt super-lattices

12.1 Summary of existing experimental studies

Magneto-optical and magnetic properties are not independently but involve a compromise, as the former correlate with the t_{Co}/t_{Pt} ratio and the latter depend inversely on this ratio.[57] Investigations on CoPt superstructures yield that the superstructure with a Co thickness of $t_{Co} = 4$Å and a Pt thickness of $t_{Pt} = 12.7$Å shows the highest Kerr rotation with the constraint of 100% remanence and positive nucleation field H_n at a wave length $\lambda = 820$ nm. Assuming a (111) surface orientation and a perpendicular lattice spacing of 2.265Å, the thicknesses of this superstructure in mono-layers (ML) are given by $t_{Co} = 1.8$ML and $t_{Pt} = 5.6$ML, in here is abbreviated by $\mathrm{Co}_{1.8}\mathrm{Pt}_{5.6}$. Based on Ref. [58] a Co thickness t_{Co} less than 4Å (1.8ML) and a Pt thickness t_{Pt} greater than 12Å (5.3ML) are needed for perpendicular magnetism and 100% remanence.

The comparison of photon energy dependent Kerr spectra of CoPt multi-layers and CoPt alloys [57] shows similar peak structures.This insensitivity is believed to result from the fact that the wavelength of the beam is about 100 to 1000 times larger than the multi-layer periodicity. The main influence on the Kerr effect is given by the concentration of Co. The present investigation includes multi-layer structures, only, as there are many experiments available.

Typical wavelengths of commercial magneto-optic (MO) are about 800nm (780nm, 820nm). Recently, the optical phase change (PC) media[a.] have been developed using an UV-laser with a wave-length of 405nm.

[a.] In respect of storage density and life-time the PC media compete with the MO media. When high quality and secure data storage are required, MO media have to be preferred. For economical reasons the PC media will probably replace MO devices in the next years because PC devices are cheaper as no polarization sensitive detection optics is required. First, the number of read/write/erase cycles in PC media is smaller than in MO media and secondly, the MO media are more resistant to mechanical damage than the purely optical PC media.

12.2 Ab-initio P-MOKE at normal incidence of the beam

In the present study the magneto-optical properties of a $(\mathrm{Pt}_6\mathrm{Co}_2)_n/\mathrm{Pt}(111)$ superstructure with Pt layers on top of the surface are investigated theoretically, as discussed in Section 7, in an energy range of $\hbar\omega = 1 - 8$eV. The interest is, at one hand, the energy dependence of the Kerr rotation and ellipticity angles and, at the other hand, at fixed energy the dependence of the Kerr rotation and ellipticity angles on the repetition number n in $(\mathrm{Pt}_6\mathrm{Co}_2)_n/\mathrm{Pt}(111)$ superstructures.

Furthermore it is rewarding to investigate the influence of each layer on the MO Kerr effect by analyzing the layer-resolved dielectric tensor $\varepsilon^p_{\mu\nu}$, see Fig. 12.1, where p is the layer number and μ, ν are x, y, z. The dielectric tensor of a paramagnetic medium has vanishing off-diagonal elements, and no MO effects occur. The polarization of a paramagnetic substrate can be seen in the dielectric tensor elements. In Fig. 12.1, the typical properties [54] of CoPt-superstructures are shown, namely that the off-diagonal elements of the interface Pt layer exceed that of the magnetic Co layers. This means that the influence to the MO Kerr effect is mainly due to the Pt layers.

Fig. 12.2 shows that for the Co/Pt multi-layer structure the magneto-optic response is not only favorable in the blue laser regime (405nm such as the phase change optical devices) but that the peak in the Kerr rotation angle occurs at even higher energies, at about 4eV, allowing a further increase of the storage density.

A comparison between experimental values and calculations ones shows that the peaks of the magneto-optic Kerr angles appear at about the same energies. The magnitude of the angles in experiments is larger but due to the fact that in experiments the repetition number is at least 10 (in these calculations it is only 6). Presumably, by increasing the number of repetitions of the $(\mathrm{Pt}_6\mathrm{Co}_2)$ structure should finally lead to larger values. An additional reason that may explain the different size of the Kerr angles may be that the measurements could have been performed for an angle of incidence where the maximum MOKE occurs, see Sections 3.5 and 10.5.1.

Comparing superstructures $(\mathrm{Pt}_6\mathrm{Co}_2)_n/\mathrm{Pt}(111)$ with different repetition number at the same energy, i.e., $\hbar\omega = 3$eV (which was chosen to be the same as in the PC-media laser, 405nm) in Fig. 12.3, due to the finite penetration depth of the beam [68] saturation of the Kerr rotation and ellipticity angles, θ_K and ε_K, is to be expected. Indeed, only six repetitions are necessary to see the flattening of the Kerr rotation angle θ_K.

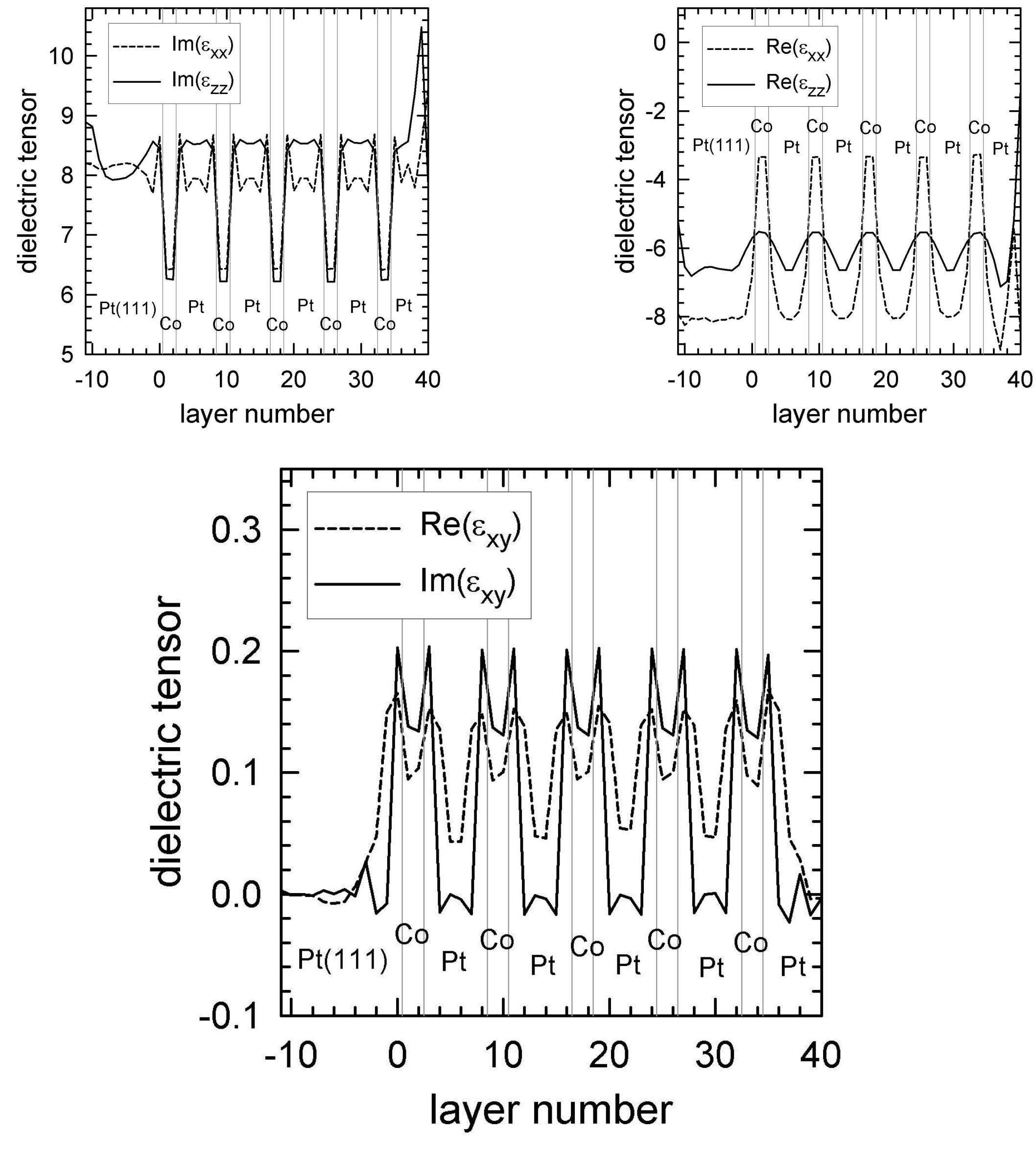

Figure 12.1: The layer-resolved complex dielectric tensor elements ε^p_{xx}, ε^p_{zz}, and ε^p_{xy} in the case of $(Pt_6Co_2)_5/Pt(111)$. The layers are labelled beginning with the the first Co in $(Pt_6Co_2)_5$, $p = 1$, and hence, negative layer indices refer to the Pt buffer layers on top of the Pt(111) substrate. The vertical lines denote the interface between Pt_6 and Co_2.

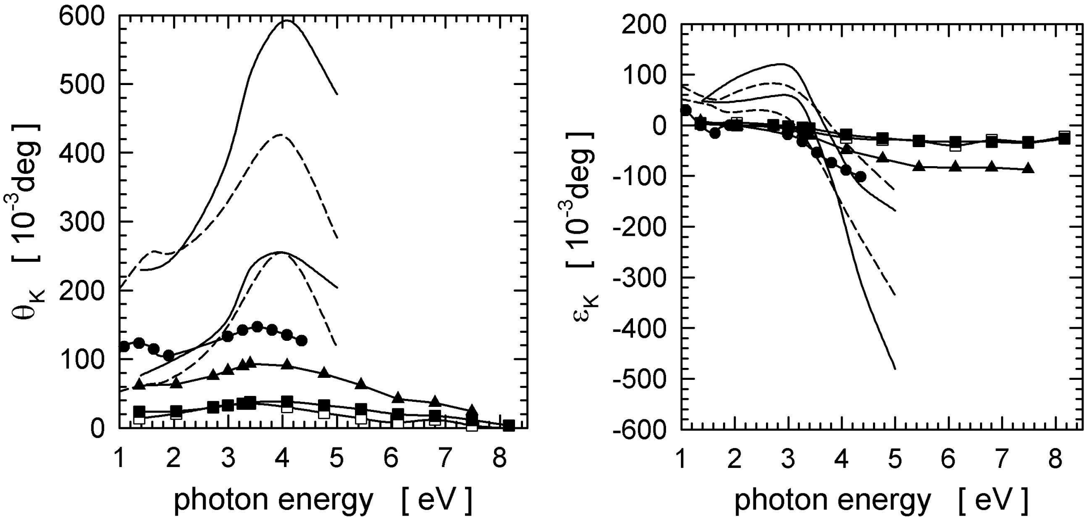

Figure 12.2: Dependence of the Kerr rotation and ellipticity angles, θ_K and ε_K, on the photon energy. Open squares denote $Co_2/Pt(111)$, full squares, full triangles, and full circles denote the superstructures $(Pt_6Co_2)_n/Pt(111)$ with $n = 1, 3, 6$, respectively. The solid and dashed lines refer to measured MO Kerr angles for different t_{Co}/t_{Pt} ratios [57, 58].

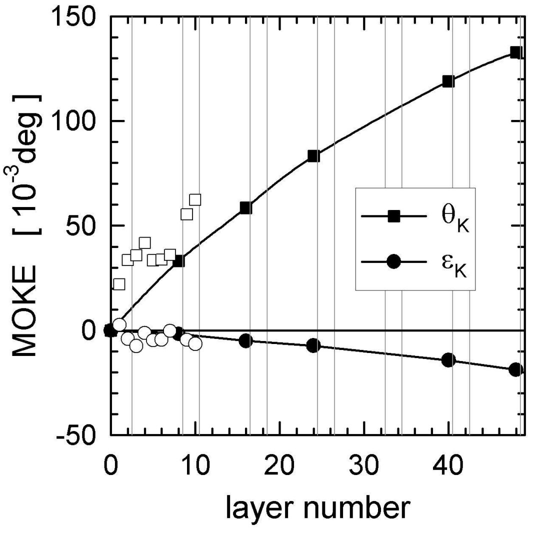

Figure 12.3: The MOKE in CoPt multi-layer structures on Pt(111) at an energy of $\hbar\omega = 3$eV. Vertical lines refer to the same boundaries as in Fig.12.1. Full symbols refer to structures with completed structure $(Pt_6Co_2)_n/Pt(111)$, open symbols refer to incomplete super-structures such as $Pt_1Co_2/Pt(111)$.

Part IV

Appendix

A Magneto-Optical Readout

A magneto-optical device possesses a sensitive readout because the Kerr quantities are in the range of tenths of degrees. Information is stored in bits being magnetized either upwards or downwards (for perpendicular recording). Thus, it is the aim to design the magneto-optical readout such that the signal difference between up and down magnetization is largest. Fig. A.1 schematically shows the optical path of the laser beam. The beam first passes a collimator, a polarizer, the beam splitter, and the objective lens before it impinges on the magneto-optical medium. After reflection, the beam splitter reflects a partition of the light to the analyzer the role of which will be discussed in detail in the current chapter. [28]

A.1 The polarizing beam splitter (PBS)

A.1.1 The effect of the PBS on a beam

The PBS resolves the components of the incident polarization along two mutually orthogonal axis ξ and η and the two transmitted beams are linearly polarized. In the following, the effect on an elliptically polarized wave, being is the linear superposition of the two circularly polarized basis waves, is analyzed.

Definition of left (LCP) and right (RCP) circularly polarized waves: A left circularly polarized (LCP) wave has positive helicity, ie. $\mathbf{E}$ turns counter-clock-wise when the observer is facing in the on-coming wave. This concept is opposite to that of the handedness. Under time inversion the LCP wave becomes RCP and vice versa. The same holds for reflection.

A.1.2 Transmission of the elliptically polarized wave

We have to find the projection of the electric field vector of the circularly polarized waves to the axes of the PBS, (ξ, η). Originally the wave is given in the basis $\{\mathbf{e}_x, \mathbf{e}_y\}$, thus the right circularly polarized (RCP) wave is given by

$$\begin{aligned} &E_- \left(\cos(\omega t + \Delta_-)\mathbf{e}_x - \sin(\omega t + \Delta_-)\mathbf{e}_y\right) = \\ &\qquad = E_- \left(\cos(\omega t + \Delta_- + \gamma)\mathbf{e}_\xi - \sin(\omega t + \Delta_- + \gamma)\mathbf{e}_\eta\right) \end{aligned}$$

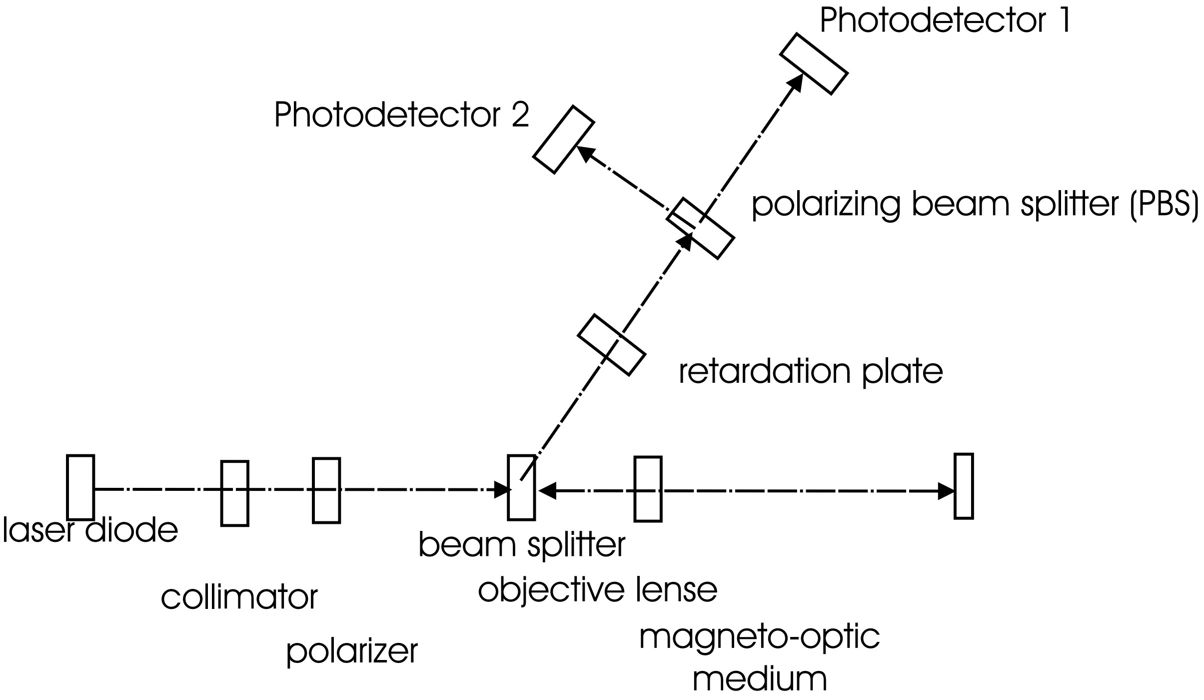

Figure A.1: The magneto-Optical readout.

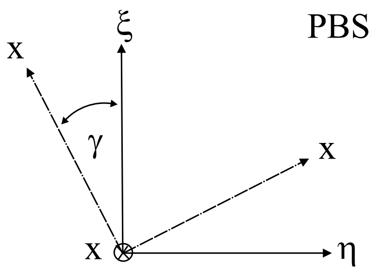

Figure A.2: ξ and η are mutually orthogonal. the two transmitted beams are linearly polarized.

and the left circularly polarized (LCP) wave by

$$E_+\left(\cos(\omega t+\Delta_+)\mathbf{e}_x+\sin(\omega t+\Delta_+)\mathbf{e}_y\right)= \\ =E_+\left(\cos(\omega t+\Delta_+-\gamma)\mathbf{e}_\xi+\sin(\omega t+\Delta_+-\gamma)\mathbf{e}_\eta\right) \quad .$$

Then the PBS splits the incident elliptically polarized wave into the two linear polarized beams in ξ and η direction

$$\mathbf{e}_\xi: \quad E_-\cos(\omega t+\Delta_-+\gamma)+E_+\cos(\omega t+\Delta_+-\gamma) \quad , \tag{A.1}$$

$$\mathbf{e}_\eta: \quad -E_-\sin(\omega t+\Delta_-+\gamma)+E_+\sin(\omega t+\Delta_+-\gamma) \quad . \tag{A.2}$$

A.1.3 Differential detection scheme

The Signals S_ξ and S_η are subtracted. The time averages in ξ and η direction are

$$S_\xi=E_-^2\langle\cos^2(\omega t+\Delta_-+\gamma)\rangle+E_+^2\cos(\omega t+\Delta_+-\gamma) \tag{A.3}$$

$$+E_-E_+\langle\cos(\omega t+\Delta_-+\gamma)\cos(\omega t+\Delta_+-\gamma)\rangle \tag{A.4}$$

$$=\frac{1}{2}(E_-^2+E_+^2)+E_-E_+\langle\cos(2\omega t+\Delta_-+\Delta_+)\rangle\cos(\Delta_--\Delta_++2\gamma) \tag{A.5}$$

$$=\frac{1}{2}(E_-^2+E_+^2)+E_-E_+\cos(2\gamma+(\Delta_--\Delta_+)) \quad , \tag{A.6}$$

$$S_\eta=\frac{1}{2}(E_-^2+E_+^2)-E_-E_+\cos(2\gamma+(\Delta_--\Delta_+)) \quad . \tag{A.7}$$

The difference for this magnetization state is given by

$$\Delta S(\uparrow)=S_\xi-S_\eta=2E_-E_+\cos(2\gamma+(\Delta_--\Delta_+)) \tag{A.8}$$

and for the reversed magnetization state by

$$\Delta S(\downarrow)=S_\xi-S_\eta=2E_-E_+\cos(2\gamma-(\Delta_--\Delta_+)) \quad . \tag{A.9}$$

As cosine is an even function, at $\gamma=\pi/4$ the two signals coincide.

In order to obtain a the situation for ΔS where the phase shift between LCP and RCP is zero, a retardation plate has to be included. The thickness of this plate has to be chosen such that the optimum value for a specific read out device and a certain MO medium is attained.

A.1.4 Introduction of the retardation plate

Before passing the *retardation plate* the wave has the form

$$\mathbf{e}_x: \quad E_-\cos(\omega t+\Delta_-)+E_+\cos(\omega t+\Delta_+) \quad , \tag{A.10}$$

$$\mathbf{e}_y: \quad -E_-\sin(\omega t+\Delta_-)+E_+\sin(\omega t+\Delta_+) \quad , \tag{A.11}$$

$$\mathbf{E}_-+\mathbf{E}_+=\tilde{E}_x\mathbf{e}_x+\tilde{E}_y\mathbf{e}_y \quad , \quad \tilde{E}_x=E_xe^{i\phi_x} \quad \text{and} \quad \tilde{E}_y=E_ye^{i\phi_y} \quad , \tag{A.12}$$

thus, the wave leaving the retardation plate, represented in (x, y) coordinates, is

$$E_x = \frac{1}{2}(E_- e^{i\phi_-} + E_+ e^{i\phi_+}) \quad , \tag{A.13}$$

$$E_y = \frac{1}{2}(E_- e^{i\phi_-} - E_+ e^{i\phi_+}) \quad . \tag{A.14}$$

The (ξ, η) coordinates belonging to the PBS—the two signs belonging to the two magnetization states—are

$$\mathbf{E}_\xi = \tilde{E}_x \cos\gamma \pm \tilde{E}_y \sin\gamma \quad , \tag{A.15}$$

$$\mathbf{E}_\eta = \tilde{E}_x \sin\gamma \mp \tilde{E}_y \cos\gamma \quad . \tag{A.16}$$

The the difference between the two signals is given by

$$\Delta S = S_\xi - S_\eta = (\tilde{E}_x \cos\gamma \pm \tilde{E}_y \sin\gamma) \cdot cc. - (\tilde{E}_x \sin\gamma \mp \tilde{E}_y \cos\gamma) \cdot cc. \tag{A.17}$$

$$= (E_x e^{i\phi_x} \cos\gamma \pm E_y e^{i\phi_y} \sin\gamma) \cdot cc. - (E_x e^{i\phi_x} \sin\gamma \mp E_y e^{i\phi_y} \cos\gamma) \cdot cc. \tag{A.18}$$

$$= (E_x^2 - E_y^2)(\cos^2\gamma - \sin^2\gamma) \pm 2E_x E_y (e^{i(\phi_x - \phi_y)} + cc.) \sin\gamma \cos\gamma \tag{A.19}$$

$$= (E_x^2 - E_y^2)\cos(2\gamma) \pm 2E_x E_y 2\cos(\phi_x - \phi_y)\frac{1}{2}\sin(2\gamma) \quad , \tag{A.20}$$

$$\Delta S = (E_x^2 - E_y^2)\cos(2\gamma) \pm 2E_x E_y \cos(\phi_x - \phi_y)\sin(2\gamma) \quad . \tag{A.21}$$

The optimum read-out signal—this is when the difference between the signal for up- and down magnetization is largest—is achieved for a crossing between the axis of the PBS with respect to the axis of the elliptically polarized wave is $\pi/4$,

$$\Delta S(\uparrow) - \Delta S(\downarrow) = 4E_x E_y \cos(\phi_x - \phi_y) \quad , \tag{A.22}$$

and if a retardation plate is included in the optical path eliminating the phase shift between the RCP and the LCP,

$$\Delta S(\uparrow) - \Delta S(\downarrow) = 4E_x E_y \quad . \tag{A.23}$$

The the Kerr angles are then obtained by

$$\tan(2\theta_K) = \frac{2|E_y/E_x|}{1 - |E_y/E_x|^2}\cos(\phi_y - \phi_x) \quad , \tag{A.24}$$

$$\sin(2\varepsilon_K) = -\frac{2|E_y/E_x|}{1 + |E_y/E_x|^2}\sin(\phi_y - \phi_x) \quad . \tag{A.25}$$

B Approximative formulas for Kerr angles

The formulas for the Kerr rotation and ellipticity angles given in equation (2.7) and (2.8) are compared with approximative formulas given in the literature. According to Ref. [32] the Kerr angles are given approximately by

$$\theta_{Ks} \approx -\mathrm{Re}(\tilde{r}_{ps}/\tilde{r}_{ss}) \tag{B.1}$$

$$\theta_{Kp} \approx \mathrm{Re}(\tilde{r}_{sp}/\tilde{r}_{pp}) \tag{B.2}$$

$$\varepsilon_{Ks} \approx \frac{\mathrm{Im}(\tilde{r}_{ps}/\tilde{r}_{ss})}{\mathrm{Re}(\tilde{r}_{ps}/\tilde{r}_{ss})} \tag{B.3}$$

$$\varepsilon_{Kp} \approx \frac{\mathrm{Im}(\tilde{r}_{sp}/\tilde{r}_{pp})}{\mathrm{Re}(\tilde{r}_{sp}/\tilde{r}_{pp})} \tag{B.4}$$

The complex Kerr angle Θ_K is often [36, 33] approximated by

$$\Theta_{Ks} \approx \tilde{r}_{ps}/\tilde{r}_{ss} = \theta_{Ks} + i\varepsilon_{Ks} \tag{B.5}$$

$$\Theta_{Kp} \approx \tilde{r}_{sp}/\tilde{r}_{pp} = \theta_{Kp} + i\varepsilon_{Kp} \tag{B.6}$$

We want to test the equivalence of the equations (2.7)-(2.8) and the equations (B.5)-(B.6).

If the complex refractive index of equation (B.6) is the starting point of the calculations, one has

$$\Theta_{Kp} \approx \theta_{Kp} + i\varepsilon_{Kp} \tag{B.7}$$

$$\approx \frac{\tilde{r}_{sp}}{\tilde{r}_{pp}} = \frac{r_{sp}}{r_{pp}} e^{i(\Delta_{sp} - \Delta_{pp})} \tag{B.8}$$

and thus

$$\rightarrow \varepsilon_{Kp} \approx \frac{r_{sp}}{r_{pp}} \sin(\Delta_{sp} - \Delta_{pp}) \tag{B.9}$$

$$\rightarrow \theta_{Kp} \approx \frac{r_{sp}}{r_{pp}} \cos(\Delta_{sp} - \Delta_{pp}) \tag{B.10}$$

For an incident p-wave the ellipticity can be calculated with the help of equation (2.8)

$$\begin{aligned}
\tan\varepsilon_{Kp} &= \frac{|\tilde{a}_+| - |\tilde{a}_-|}{|\tilde{a}_+| + |\tilde{a}_-|} && \text{(B.11)}\\
|\tilde{a}_\pm| &= |r_{pp}e^{i\Delta_{pp}} \mp ir_{sp}e^{i\Delta_{sp}}| && \text{(B.12)}\\
&= |(r_{pp}\cos\Delta_{pp} \pm r_{sp}\sin\Delta_{sp}) + i(r_{pp}\sin\Delta_{pp} \mp r_{sp}\cos\Delta_{sp})| && \text{(B.13)}\\
&= (r_{pp}^2 + r_{sp}^2 \pm r_{pp}r_{sp}\sin(\Delta_{sp} - \Delta_{pp}))^{1/2} && \text{(B.14)}\\
&\approx (r_{pp}^2 + r_{sp}^2)^{1/2}\left(1 \pm \frac{r_{pp}r_{sp}\sin(\Delta_{sp} - \Delta_{pp})}{r_{pp}^2 + r_{sp}^2}\right) && \text{(B.15)}\\
\rightarrow \tan\varepsilon_{Kp} &= \frac{r_{pp}r_{sp}}{r_{pp}^2 + r_{sp}^2}\sin(\Delta_{sp} - \Delta_{pp}) && \text{(B.16)}
\end{aligned}$$

If $r_{pp} >> r_{sp}$, then

$$\tan\varepsilon_{Kp} \approx \frac{r_{pp}r_{sp}}{r_{pp}^2}\sin(\Delta_{sp} - \Delta_{pp}) = \frac{r_{sp}}{r_{pp}}\sin(\Delta_{sp} - \Delta_{pp}) \tag{B.17}$$

which is equivalent to equation (B.9).

The Kerr rotation obeys the equations (2.7),

$$\begin{aligned}
\theta_{Kp} &= -\frac{1}{2}(\Delta_+ - \Delta_-), \quad \tan\Delta_\pm = \mathrm{Im}(\tilde{a}_\pm)/\mathrm{Re}(\tilde{a}_\pm) && \text{(B.18)}\\
\theta_{Kp} &\approx -\frac{1}{2}\left(\frac{\mathrm{Im}(\tilde{a}_+)}{\mathrm{Re}(\tilde{a}_+)} - \frac{\mathrm{Im}(\tilde{a}_-)}{\mathrm{Re}(\tilde{a}_-)}\right) && \text{(B.19)}\\
= \theta_{Kp} &\approx -\frac{1}{2}\frac{\mathrm{Im}(\tilde{a}_+)\mathrm{Re}(\tilde{a}_-) - \mathrm{Im}(\tilde{a}_-)\mathrm{Re}(\tilde{a}_+)}{\mathrm{Re}(\tilde{a}_+)\mathrm{Re}(\tilde{a}_-)} && \text{(B.20)}
\end{aligned}$$

$$\begin{aligned}
\tilde{a}_\pm &= \frac{1}{\sqrt{2}}(\tilde{r}_{pp} \mp i\tilde{r}_{sp}) && \text{(B.21)}\\
\tilde{r}_{pp} &= r_{pp}e^{i\Delta_{pp}}, \qquad \tilde{r}_{sp} = r_{sp}e^{i\Delta_{sp}} && \text{(B.22)}\\
\mathrm{Re}(\tilde{a}_\pm) &= \frac{1}{\sqrt{2}}(r_{pp}\cos\Delta_{pp} \pm r_{sp}\sin\Delta_{sp}) && \text{(B.23)}\\
\mathrm{Im}(\tilde{a}_\pm) &= \frac{1}{\sqrt{2}}(r_{pp}\sin\Delta_{pp} \mp r_{sp}\cos\Delta_{sp}) && \text{(B.24)}
\end{aligned}$$

Therefore the numerator of θ_{Kp} is given by

$$\frac{1}{2}2r_{sp}\cos\Delta_{sp}(r_{sp}\sin\Delta_{sp} - r_{pp}\cos\Delta_{pp}) \tag{B.25}$$

the nominator by

$$-(r_{sp}\sin\Delta_{sp} - r_{pp}\cos\Delta_{pp})(r_{sp}\sin\Delta_{sp} + r_{pp}\cos\Delta_{pp}) \tag{B.26}$$

Thus for $r_{sp} << r_{pp}$

$$\theta_{Kp} \approx \frac{r_{sp}\cos\Delta_{sp}}{r_{sp}\sin\Delta_{sp} + r_{pp}\cos\Delta_{pp}} \approx \frac{r_{sp}\cos\Delta_{sp}}{r_{pp}\cos\Delta_{pp}} \tag{B.27}$$

is obtained. An approximation of $\cos\Delta_{sp}/\cos\Delta_{pp} \approx e^{i(\Delta_{sp}-\Delta_{pp})} \approx \cos(\Delta_{sp} - \Delta_{pp})$ yields

$$\theta_{Kp} \approx \frac{r_{sp}}{r_{pp}}\cos(\Delta_{sp} - \Delta_{pp}) \tag{B.28}$$

which is identical to equation (B.10).

C Auxiliary calculations for P-MOKE

For an incident p-wave the Kerr rotation angle reads

$$\tan\Theta_K^p = \frac{\tilde{r}_{sp}}{\tilde{r}_{pp}} \tag{C.1}$$

$$= \frac{n\varepsilon_{xy}\cos\alpha}{n'(n\cos\alpha' + n'\cos\alpha)(n\cos\alpha + n'\cos\alpha')}\frac{n'\cos\alpha + n\cos\alpha'}{n'\cos\alpha - n\cos\alpha'} \tag{C.2}$$

$$= \frac{n\varepsilon_{xy}\cos\alpha}{n'(n\cos\alpha + n'\cos\alpha')(n'\cos\alpha - n\cos\alpha')}. \tag{C.3}$$

For an incident s-wave the following equation is obtained

$$\tan\Theta_K^s = \frac{\tilde{r}_{ps}}{\tilde{r}_{ss}} \tag{C.4}$$

$$= \frac{\varepsilon_{xy}n\cos\alpha}{n'(n\cos\alpha' + n'\cos\alpha)(n\cos\alpha + n'\cos\alpha')}\frac{n\cos\alpha + n'\cos\alpha'}{n\cos\alpha - n'\cos\alpha'} \tag{C.5}$$

$$= \frac{\varepsilon_{xy}n\cos\alpha}{n'(n\cos\alpha' + n'\cos\alpha)(n\cos\alpha - n'\cos\alpha')} \tag{C.6}$$

The nominators for Θ_K^p (incident p-wave)

$$(n\cos\alpha + n'\cos\alpha')(n'\cos\alpha - n\cos\alpha') = \\ = (n^{'2} - n^2)\cos\alpha\cos\alpha' - nn'(\cos^2\alpha - \cos^2\alpha') \tag{C.7}$$

are transformed by reformulating the second term in equation (C.7) using the addition theorem ($\cos^2 x = 1 - \sin^2 x$) and Snell's law ($n\sin\alpha = n'_\pm \sin\alpha'_\pm$)

$$nn'(\cos^2\alpha - \cos^2\alpha') = nn'(\sin^2\alpha' - \sin^2\alpha) \tag{C.8}$$

$$= nn'(\frac{n}{n'} - \frac{n'}{n})\sin\alpha\sin\alpha' \tag{C.9}$$

$$= (n^2 - n^{'2})\sin\alpha\sin\alpha' \tag{C.10}$$

and consequently the nominator (incident p-wave) becomes

$$(n\cos\alpha + n'\cos\alpha')(n'\cos\alpha - n\cos\alpha') = (n^{'2} - n^2)\cos(\alpha + \alpha') \tag{C.11}$$

The same ideas for an incident s-wave lead to

$$(n\cos\alpha' + n'\cos\alpha)(n\cos\alpha - n'\cos\alpha') = (n^2 - n^{'2})\cos(\alpha - \alpha') \tag{C.12}$$

D Auxiliary calculations to the incident s-wave (P-MOKE)

Introducing $A_\pm \equiv \frac{\varepsilon_{xy}\sin^2\alpha'_\pm}{2\varepsilon_{xx}\cos\alpha'_\pm}$, (3.68) and (3.70) become

$$\begin{aligned} -\cos\alpha E_p'' &= \left(-A_+ - i\right)\cos\alpha'_+ E'_{s+} + \left(-A_- + i\right)\cos\alpha'_- E'_{s-}, && \text{(D.1)} \\ nE_p'' &= n'_+\left(A_+ - i\right)E'_{s+} + n'_-\left(A_- + i\right)E'_{s-}. && \text{(D.2)} \end{aligned}$$

E'_{s+} is eliminated by adding equation (D.1) multiplied by $n'_+\left(A_+ - i\right)$ and (D.2) multiplied by $\left(A_+ + i\right)\cos\alpha'_+$, which gives E'_{s-}

$$E'_{s-} = \frac{n\cos\alpha'_+\left(A_+ + i\right) - n'_+\cos\alpha\left(A_+ - i\right)}{n'_+\cos\alpha'_-\left(A_+ - i\right)\left(-A_- + i\right) + n'_-\cos\alpha'_+\left(A_+ + i\right)\left(A_- + i\right)}E_p'' \tag{D.3}$$

E'_{s-} is eliminated by summing over equation (D.1) multiplied by $\left(-n'_-\right)\left(A_- + i\right)$ and (D.2) multiplied by $\left(-A_- + i\right)\cos\alpha'_-$, yielding E'_{s+}

$$E'_{s+} = \frac{n'_-\cos\alpha\left(A_- + i\right) + n\cos\alpha'_-\left(-A_- + i\right)}{n'_-\cos\alpha'_+\left(A_- + i\right)\left(A_+ + i\right) + n'_+\cos\alpha'_-\left(-A_- + i\right)\left(A_+ - i\right)}E_p'' \tag{D.4}$$

Next the nominator of E'_{s+} and E'_{s-} (in equation (D.3) and (D.4)),

$$n'_-\cos\alpha'_+\left(A_- + i\right)\left(A_+ + i\right) + n'_+\cos\alpha'_-\left(-A_- + i\right)\left(A_+ - i\right), \tag{D.5}$$

will be approximated to first order in ε_{xy},

$$\begin{aligned} \left(A_- + i\right)\left(A_+ + i\right) &= \left(\frac{\varepsilon_{xy}\sin^2\alpha'_-}{2\varepsilon_{xx}\cos\alpha'_-} + i\right)\left(\frac{\varepsilon_{xy}\sin^2\alpha'_+}{2\varepsilon_{xx}\cos\alpha'_+} + i\right) && \text{(D.6)} \\ &= \frac{\varepsilon_{xy}^2\sin^2\alpha'_-\sin^2\alpha'_+}{4\varepsilon_{xx}^2\cos\alpha'_-\cos\alpha'_+} + i\frac{\varepsilon_{xy}}{2\varepsilon_{xx}}\left(\frac{\sin^2\alpha'_-}{\cos\alpha'_-} + \frac{\sin^2\alpha'_+}{\cos\alpha'_+}\right) - 1 && \text{(D.7)} \\ &\approx i\frac{\varepsilon_{xy}}{2\varepsilon_{xx}}\left(\frac{\sin^2\alpha'_-}{\cos\alpha'_-} + \frac{\sin^2\alpha'_+}{\cos\alpha'_+}\right) - 1, && \text{(D.8)} \\ \left(-A_- + i\right)\left(A_+ - i\right) &\approx i\frac{\varepsilon_{xy}}{2\varepsilon_{xx}}\left(\frac{\sin^2\alpha'_-}{\cos\alpha'_-} + \frac{\sin^2\alpha'_+}{\cos\alpha'_+}\right) + 1, && \text{(D.9)} \end{aligned}$$

so that (D.5) becomes

$$\underbrace{n'_+\cos\alpha'_- - n'_-\cos\alpha'_+}_{(1)} + i\frac{\varepsilon_{xy}}{2\varepsilon_{xx}}\left(\frac{\sin^2\alpha'_-}{\cos\alpha'_-} + \frac{\sin^2\alpha'_+}{\cos\alpha'_+}\right)\left(n'_+\cos\alpha'_- + n'_-\cos\alpha'_+\right). \tag{D.10}$$

The term (1) will be transformed by augmenting it with $n'_+ \cos\alpha'_- + n'_- \cos\alpha'_+$, yielding

$$n'_+ \cos\alpha'_- - n'_- \cos\alpha'_+ = \frac{n'^2_+ \cos^2\alpha'_- - n'^2_- \cos^2\alpha'_+}{n'_+ \cos\alpha'_- + n'_- \cos\alpha'_+}. \tag{D.11}$$

Insertion of $n'_\pm$ in the first order approximation $n_\pm = \varepsilon_{xx} \pm i\varepsilon_{xy} \cos\alpha_\pm$ gives

$$\frac{\varepsilon_{xx}(\cos^2\alpha'_- - \cos^2\alpha'_+) + i\varepsilon_{xy}(\cos\alpha_+ \cos^2\alpha'_- + \cos\alpha_- \cos^2\alpha'_+)}{n'_+ \cos\alpha'_- + n'_- \cos\alpha'_+} \tag{D.12}$$

With $\cos^2 x = 1 - \sin^2 x$ and Snell's law $(n \sin\alpha = n'_\pm \sin\alpha'_\pm)$

$$\begin{aligned}
\cos^2\alpha'_- - \cos^2\alpha'_+ &= \sin^2\alpha'_+ - \sin^2\alpha'_- && \text{(D.13)}\\
&= n^2 \sin^2\alpha \left(\frac{1}{n'^2_+} - \frac{1}{n'^2_-}\right) && \text{(D.14)}\\
&= n^2 \sin^2\alpha \frac{n'^2_- - n'^2_+}{n'^2_- n'^2_+} && \text{(D.15)}
\end{aligned}$$

Insertion of $n'_\pm$ gives

$$-i\varepsilon_{xy} n^2 \sin^2\alpha \frac{\cos\alpha_- + \cos\alpha_+}{n'^2_- n'^2_+} \tag{D.16}$$

and thus (D.5) reads

$$\begin{aligned}
&\frac{-i\varepsilon_{xx}\varepsilon_{xy} n^2 \sin^2\alpha \frac{\cos\alpha'_- + \cos\alpha'_+}{n'^2_- n'^2_+}}{n'_+ \cos\alpha'_- + n'_- \cos\alpha'_+} + \\
&\qquad + \frac{i\varepsilon_{xy}(\cos\alpha'_+ \cos^2\alpha'_- + \cos\alpha'_- \cos^2\alpha'_+)}{n'_+ \cos\alpha'_- + n'_- \cos\alpha'_+} + i\frac{\varepsilon_{xy}}{2n'^2}\frac{2\sin^2\alpha'}{\cos\alpha'} 2n' \cos\alpha'
\end{aligned}$$

If higher orders of ε_{xy} are neglected, the approximation $\cos\alpha'_+ \approx \cos\alpha'_- \approx \cos\alpha'$ and $n'_+ \approx n'_- \approx n' \approx \sqrt{\varepsilon_{xx}}$, and Snell's law $\frac{n}{n'} \sin\alpha = \sin\alpha'$ give

$$\begin{aligned}
&= i\varepsilon_{xy} \frac{-\varepsilon_{xx} n^2 \sin^2\alpha \frac{2\cos\alpha'}{n'^4} + 2\cos^3\alpha'}{2n' \cos\alpha'} + i\varepsilon_{xy} \frac{2\sin^2\alpha'}{n'} \\
&= i\varepsilon_{xy} \frac{-\frac{\varepsilon_{xx} n^2}{n'^4} \sin^2\alpha + \cos^2\alpha' + 2\sin^2\alpha'}{n'} = i\frac{\varepsilon_{xy}}{n'}
\end{aligned}$$

From (D.3) and from (D.4) we obtain:

$$E'_{s-} = -i\frac{n'}{\varepsilon_{xy}}(n \cos\alpha'_+ (A_+ + i) - n'_+ \cos\alpha (A_+ - i)) E''_p, \tag{D.17}$$

$$E'_{s+} = -i\frac{n'}{\varepsilon_{xy}}(n'_- \cos\alpha (A_- + i) - n \cos\alpha'_- (A_- - i)) E''_p. \tag{D.18}$$

$$E'_{s-} \approx E'_{s+} \approx -i\frac{n'}{\varepsilon_{xy}}(n\cos\alpha'_+ \,(A_+ + i) - n'_+ \cos\alpha \,(A_+ - i))E''_p \tag{D.19}$$

$$\approx -i\frac{n'}{\varepsilon_{xy}}(\underbrace{(n\cos\alpha'_+ - n'_+\cos\alpha)A_+}_{neglect} + i(n\cos\alpha'_+ + n'_+\cos\alpha))E''_p \tag{D.20}$$

$$\approx \frac{n'(n\cos\alpha' + n'\cos\alpha)}{\varepsilon_{xy}}E''_p \tag{D.21}$$

$E'_{s\pm}$ are inserted into the equations (3.67) and (3.69)

$$E_s + E''_s = 2\frac{n'(n\cos\alpha' + n'\cos\alpha)}{\varepsilon_{xy}}E''_p, \tag{D.22}$$

$$n\cos\alpha(E_s - E''_s) = 2n'\cos\alpha'\frac{n'(n\cos\alpha' + n'\cos\alpha)}{\varepsilon_{xy}}E''_p. \tag{D.23}$$

$E''_p(E_s)$ and $E''_s(E_s)$ are determined by summing over or subtracting of (D.22) multiplied by $n\cos\alpha$ and (D.23), yielding

$$E''_p = \frac{\varepsilon_{xy} n\cos\alpha}{n'(n\cos\alpha' + n'\cos\alpha)(n\cos\alpha + n'\cos\alpha')}E_s, \tag{D.24}$$

$$E''_s = \frac{n\cos\alpha - n'\cos\alpha'}{n'\cos\alpha' + n\cos\alpha}E_s. \tag{D.25}$$

E The magneto-static energy

The magneto-static energy is obtained from the Maxwell-equations[a.],

$$\partial_i B_i = 0, \qquad \partial_i D_i = 4\pi\rho,$$
$$\epsilon_{ijk}\partial_j E_k = -\frac{1}{c}\partial_0 H_i, \qquad \epsilon_{ijk}\partial_j H_k = \frac{4\pi}{c} j_i + \frac{e}{c}\partial_0 D_i,$$

and the electro-magnetic force,

$$f_i = \frac{1}{c}(\rho E_i + \epsilon_{ijk} j_j B_k), \tag{E.1}$$

assuming for the magneto-static case vanishing fields **E** and **D**. As the force is the total differential of the energy, the scope of the following lines is to express **f** as a total differential of the fields **H** and **B**. The current density **j** in the equation (E.1) is expressed in terms of the magnetic field **H**,

$$\begin{aligned} j_i &= \frac{c}{4\pi}\epsilon_{ijk}\partial_j H_k \\ f_i &= \frac{1}{4\pi}\epsilon_{ijk}(\epsilon_{jlm}\partial_l H_m) B_k \\ &= \frac{1}{4\pi}(B_j \partial_j H_i - B_j \partial_i H_j). \end{aligned}$$

Both terms are total differentials, the $B_j\partial_j H_i = \partial_j(H_i B_j) - H_i \partial_j B_j$, because $\partial_j B_j = 0$ and the second term as $B_j \partial_i H_j = \mu H_j \partial_i H_j = \mu\partial_i(H_j H_j)/2 = \partial_i(B_j H_j)/2$ so that

$$\begin{aligned} f_i &= \frac{1}{4\pi}(\partial_j(H_i B_j) - \frac{1}{2}\partial_i(B_j H_j)) \\ &= \frac{1}{4\pi}\partial_j\left((H_i B_j) - \frac{1}{2}\delta_{ij}(B_k H_k)\right). \end{aligned}$$

The second term is known as the magneto-static energy density w_{ij},

$$w_{ij} = -\frac{1}{8\pi}\delta_{ij}(B_k H_k), \tag{E.2}$$

and the energy is obtained by integration over the volume V,

$$W = \int_V w_{ij}(r_k)\,\mathrm{d}^3 r. \tag{E.3}$$

[a.] In here ρ is the charge density and **j** the current density.

B_i is eliminated by the material equations, $B_i = H_i + 4\pi M_i$, yielding

$$W = -\int_V \frac{1}{8\pi}\delta_{ij}((H_k + 4\pi M_k)H_k)\,\mathrm{d}^3r = -\int_V \delta_{ij}(\frac{1}{8\pi}H_kH_k + \frac{1}{2}M_kH_k)\,\mathrm{d}^3r.$$

In the following we are only interested in the part of the energy density depending on the angle between the applied field **H** and the (equilibrium) magnetization **M**,

$$\Delta w = -\frac{1}{2}\,\mathbf{M}\cdot\mathbf{H}. \tag{E.4}$$

Bibliography

[1] M. Faraday, Trans. R. soc. London (London) 5, 592 (1846).

[2] J. Kerr, Philos. Mag. 3, 339 (1877), ibid. 5, 161 (1878).

[3] H. J. Williams, R.C. Sherwood, F.G. Foster, andE.M. Kelley, J. Appl. Phys. **28**, 1181 (1957).

[4] R.L. Conger and J.L. Tomlinson, J. Appl. Phys. **33**, S-1059 (1962).

[5] E. J. Supernowicz, J. Appl. Phys. **34**, 1110 (1963).

[6] K. H. J. Buschow, In: *Ferromagnetic Materials*, E.P. Wohlfahrt and K.H.J. Buschow, editors, North-Holland, Amsterdam, **4**, 588 (1988).

[7] J. Schoenes, In: *Materials Science and Technology*, R.W. Cahn, P. Hassen, and E.J. kramer, Verlag-Chemie, Weinheim, **3**, 147 (1992).

[8] H. A. Lorentz, Arch. Meerl. **19**, 123 (1884).

[9] H.R. Hulme, Proc. Roy. Soc. A, **135**, 237 (1932).

[10] H. Feil and C.Haas, Phys. Rev. Lett. **58**, 65 (1987).

[11] J.H. Wijngaard, C. Haas, and T.A. de Groot, Phys. Rev. B **40**, 9318 (1989).

[12] R.A. de Groot, F.M. Mueller, P.G. van Engen, and K.H.J. Buschow, J. Appl. Phys. **55**, 2151 (1984).

[13] P. N. Argyres, Phys. Rev. **97**, 334, (1955).

[14] B. R. Cooper and H. Ehrenreich, Solid State Commun. **2**, (1964).

[15] W. Kohn and L. Sham, Phys. Rev. B **140**, A1133 (1965).

[16] P. Hohenberg and W. Kohn, Phys. Rev. B **136**, B864 (1964).

[17] R. Kubo, J. Phys. Soc. Jpn. **12**, 570 (1957).

[18] Wang and Callaway, Phys. Rev. B **9**, 4897 (1974).

[19] P.M. Oppeneer, J. Sticht, and F. Herman J. Magn. Soc. Jpn. **15** (S1), 73 (1991).

[20] P.M. Oppeneer, T. Maurer, J. Sticht, and J. Kübler, Phys. Rev. B **45**, 10924 (1992).

[21] P.M. Oppeneer, J. Sticht, T. Maurer, and J. Kübler, Z. Phys. B. - Condens. Matter **88**, 309 (1992).

[22] S.V. Halilov and R. Feder 1993, Solid Stat Commun. **88**, 749 (1993).

[23] G.Y. Guo and H. Ebert, Phys. Rev. B **50**, 10377 (1994).

[24] Weller, D., In H. Ebert and G. Schütz, editors, *Spin-Orbit-influenced Spectroscopies of Magnetic Solids*, Springer, Berlin (1995).

[25] C. Liu and S.D. Bader, J. Vac. Sci. Technol. **A8**(3), 2727 (1990).

[26] H. Ebert, Rep. Prog. Phys. **59**, 1665 (1996).

[27] M. Mansuripur, *The Physical Principles of Magneto-Optic Recording*, Cambridge University Press, Cambridge (1995).

[28] M. Mansuripur, *Classical Optics and its Applications*, Cambridge University Press, Cambridge (2002).

[29] Tadao Yoshida, Proceedings of the IEEE, **82** (10), 1492 (1994).

[30] *HS Technology* http://www.minidisc.org/disk_technology.html

[31] Hermann Strass, *Massenspeicher optimal einsetzen: Festplatten, Streamer, CD-ROM, WORM, Halbleiterspeicher*, Franzis-Verlag GmbH, Poing (1994).

[32] Z.J.Yang and M.R. Scheinfein, J. Appl. Phys. **74**, 11, 6810 (1993).

[33] M.-A. Schroeder, *Magnetooptische Kerr-Effekte im VUV an Eisen und Eisensystemen*, PhD Thesis, Hamburg (2000).

[34] J. Zak, E.R. Moog, C. Liu, S.D. Bader, J. Appl. Phys. **68**, 8, 4203 (1990).

[35] R.P. Hunt, J. Appl. Phys. **38**, 4, 1652 (1967).

[36] C.Y. You, S.C. Shin, Appl. Phys. Lett. **69** (9), 1315 (1996).

[37] C.Y. You, S.C. Shin, J. Appl. Phys. **84**, 1, 541 (1998).

[38] C.Y. You, S.C. Shin, J. Magn. Magn. Mat. **198-199**, 573 (1999).

[39] M.N. Deeter, D. Sarid, IEEE Transactions on Magnetics, **24**, 6, 2470 (1988).

[40] J.W. Lee, J. Kim, S.K. Kim, J.R. Jeong, S.C. Shin, Phys. Rev. B **65**, 144437 (2002).

[41] J. Zabloudil, R. Hammerling, L. Szunyogh, and P. Weinberger, *Electron Scattering in Solid Matter: A theoretical and computational treatise*, Springer Verlag, Heidelberg, (2004).

[42] K. Palotás, B. Lazarovits, L. Szunyogh and P. Weinberger, *Electric properties of nanostructures*, In: Handbook of Theoretical and Computational Nanotechnology, M. Rieth and W. Schommers editors, in press (2005).

[43] A. Vernes, L. Szunyogh, P. Weinberger, Phys. Rev. B **65**, 144448 (2002).

[44] A. Vernes, L. Szunyogh, and P. Weinberger, Phase Transitions **75**, 167 (2002).

[45] Vernes, A., Szunyogh, L., and Weinberger, P., ibid., A. Vernes, L. Szunyogh, and P. Weinberger, Phys. Rev. B **66**, 214404 (2002).

[46] L. Szunyogh, *Introduction to Multiple Scattering Theory*, lecture notes.

[47] T. Huhne, C. Zecha, and H. Ebert and P. H. Dederichs and R. Zeller, Phys. Rev. B, **58**, 16, (1998).

[48] Szunyogh, L., Ujfalussy, B., Weinberger, P., and Kollar, E., Phys. Rev. B **49**, 2721 (1994).

[49] M. Weinert, R. E. Watson, and J. W. Davenport, Phys. Rev. B **32**, 2115 (1985).

[50] G. H. O. Daalderop, P. J. Kelly, and M. F. H. Schuurmans, Phys. Rev. B **41**, 11919 (1990).

[51] P. Weinberger, L. Szunyogh, Computational Material Science 17, 414 (2000).

[52] L. Szunyogh, *Theory of electric transport*, lecture notes.

[53] I. Reichl, A. Vernes, L. Szunyogh, C. Sommers, P. Mohn, and P. Weinberger, Phil. Mag. **84**, 2543 (2004).

[54] A. Vernes, L. Szunyogh, and P. Weinberger, J. Appl. Phys. **91**, 7291 (2002).

[55] R. Hammerling, J. Zabloudil, P. Weinberger, J. Lindner, E. Kosubek, R. Nünthel, K. Baberschke, Phys. Rev. B **68**, 092406 (2003).

[56] R. Carey, D.M. Newman, B.W. Thomas, J. Phys. D: Appl. Phys. **28**, 2207 (1995).

[57] W.B. Zeper, F.J.A.M. Greidanus, P.F. Garcia, and C.R. Fincher, J. Appl. Phys. **65**, 12, 4971 (1989).

[58] E.R. Moog, J. Zak, and S.D. Bader, J. Appl. Phys. **69**, 2, 880 (1991).

[59] E.R. Moog, J. Zak, and S.D. Bader, J. Appl. Phys. **69**, 8, 4559 (1991).

[60] X. Gao, D.W. Thompson, and J.A. Woollam, Appl. Phys. Lett. **70**, 24, 3203 (1997).

[61] R. Wood, Y. Sonobe, Z. Jin, B. Wilson, J. Magn. Magn. Mat. **235**, 1 (2001).

[62] H. Muraoka, Y. Nakamura, J. Magn. Magn. Mat. **235**, 10 (2001).

[63] L. Szunyogh, B. Újfalussy, and P. Weinberger, Phys. Rev. B **51**, 9552 (1995).PRB 51, 9552 (1995).

[64] S.H. Vosko, L. Wilk, and M. Nusair, Can. J. Phys. **58**, 1200 (1980).

[65] L. Szunyogh and P. Weinberger, J. Phys. Cond. Matt. **11**, 10451 (1999);

[66] A. Vernes, L. Szunyogh, and P. Weinberger, J. Phys. Condens. Matter **13**, 1529 (2001);

[67] A. Vernes, I. Reichl, P. Weinberger, L. Szunyogh, and C. Sommers, Phys. Rev. B **70**, 195407 (2004);

[68] I. Reichl, R. Hammerling, A. Vernes, P. Weinberger, C. Sommers, and L. Szunyogh, Phys. Rev. B **70**, 214417 (2004).

[69] A. Vernes and P. Weinberger, Phys. Rev. B **70**, 134411 (2004).

[70] H.J. Hagemann, W.Gudat, and C. Kunz, J. Opt. Soc. Am. **65**, 742 (1975).

[71] J.H. Weaver, C. Krafka, D.W. Lynch, E.E. Koch, Fach—Informationszentrum Karlsruhe, (1981).

[72] Georges Bader, Alain Haché, Vo-Van Truong, Thin Solid Films **375**, 73 (2000).

[73] Vo-Van Truong, Roch Belley, Georges Bader, Alain Haché, Applied Surface Science **212-213**, 140 (2003).

[74] K. Takanashi, S. Mitani, H. Fujimori, K. Sato, and Y. Suzuki, J. Magn. Magn. Mater. **177-181**, 1199 (1998).

[75] T. Kawagoe, K. Nakamura, T. Terashima, H. Kaihoko, and T. Mizoguchi, J. Magn. Magn. Mater. **148**, 185 (1995).

[76] L. Udvardi, R. Király, L. Szunyogh, F. Denat, M.B. Taylor, B.L. Györffy, B. Újfalussy, and C. Uiberacker, J. Magn. Magn. Mater. **183**, 283 (1998);

[77] L. Udvardi, L. Szunyogh, A. Vernes, and P. Weinberger, Phil. Mag. B **81**, 613 (2001).

[78] G. Traeger, L. Wenzel, and A. Hubert, Phys. Status Solidi A **131**, 201 (1992).

[79] A. Hubert and G. Traeger, J. Magn. Magn. Mater. **124**, 185 (1993).